Analysis of different mutations in the transcription factor *LMX1B* leading to nail-patella syndrome

DISSERTATION

ZUR ERLANGUNG DES DOKTORGRADES DER NATURWISSENSCHAFTEN (DR. RER. NAT.) DER FAKULTÄT BIOLOGIE UND VORKLINISCHE MEDIZIN DER UNIVERSITÄT REGENSBURG

vorgelegt von

Lisa Lucke

aus München

im Jahr 2020

Das Promotionsgesuch wurde eingereicht am:

Die Arbeit wurde angeleitet von:

Prof. Dr. Ralph Witzgall

_____

Lisa Lucke

Table of Content

List of Figures

List of Tables

1. Introduction

1.1 Anatomy of the kidneys

The kidneys are located retroperitoneal on either side of the spine in the abdomen. Major functions of the kidneys are the control of electrolyte concentrations, osmolality, acid-base balance, and regulation of blood pressure. Most importantly, the kidneys are responsible for blood filtration. The functional unit of the kidney is the nephron, consisting of the renal corpuscle and a tubular system, subdivided into the proximal and distal tubule (Figure 1.1). The average nephron number per human kidney is around 1 million, but numbers of individuals may differ. Within the renal corpuscle blood is filtrated resulting in about 180 liter of primary urine per day. Subsequently, the primary urine is concentrated by the adjacent tubular system to between 2 and 3 liter per day. Histologically, the kidney can be divided into two major components: the cortex and the medulla.

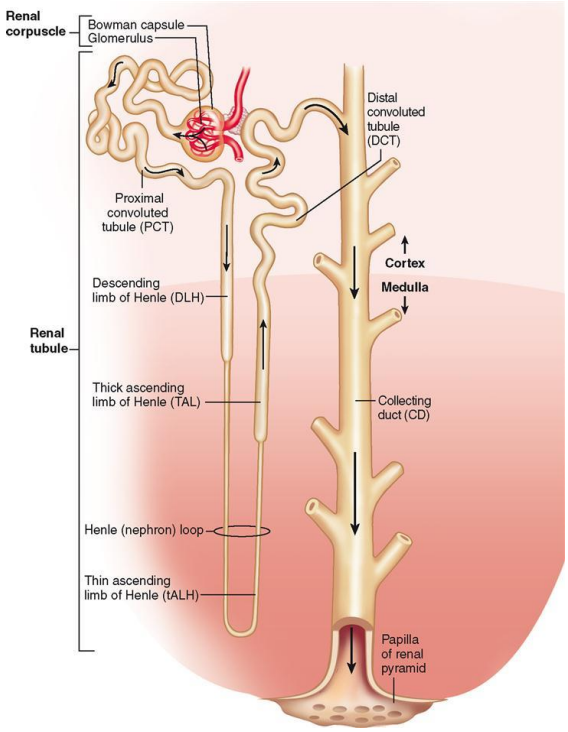

Figure 1.1: Anatomy of the kidney with its functional unit, the nephron. Nephrons spanning the cortex and medulla of the mammalian kidney. (https://basicmedicalkey.com/urinary-system-2/)

1.2 The renal corpuscle

Blood filtration occurs within the renal corpuscles, also called the Malpighian corpuscles. In the present work, the term glomerulus is often used synonymously, although it describes more precisely the capillary tuft in the center of a renal corpuscle, built by capillaries and the mesangium (Figure 1.2, [A]). The mesangium represents the backbone of the glomerular tuft comprising the mesangial matrix and mesangial cells. The endothelium of the capillary wall harbors fenestrations allowing water, peptides, peptide hormones, organic compounds, such as glucose or amino acids, and ions to flow through. The capillaries are exteriorly covered (Figure 1.2, [B]) by the sensitive network of a specific cell type: the podocytes. This assembles the inner, visceral layer of the Bowman´s capsule projecting into the Bowman´s space. The outer layer of the Bowman´s capsule is defined as the parietal layer and is composed of parietal cells enclosing the whole structure. In between the podocytes and the fenestrated endothelium, the glomerular basement membrane (GBM) is located, an extracellular matrix compartment, secreted from both cell types. The ensemble of the fenestrated endothelium, the GBM, and the podocytes is called the glomerular filtration barrier (GFB). The blood flow is directed through afferent and efferent arterioles at the vascular pole driven by hydrostatic pressure, while the primary urine leaves the renal corpuscle at the opposing urinary pole.

[A]

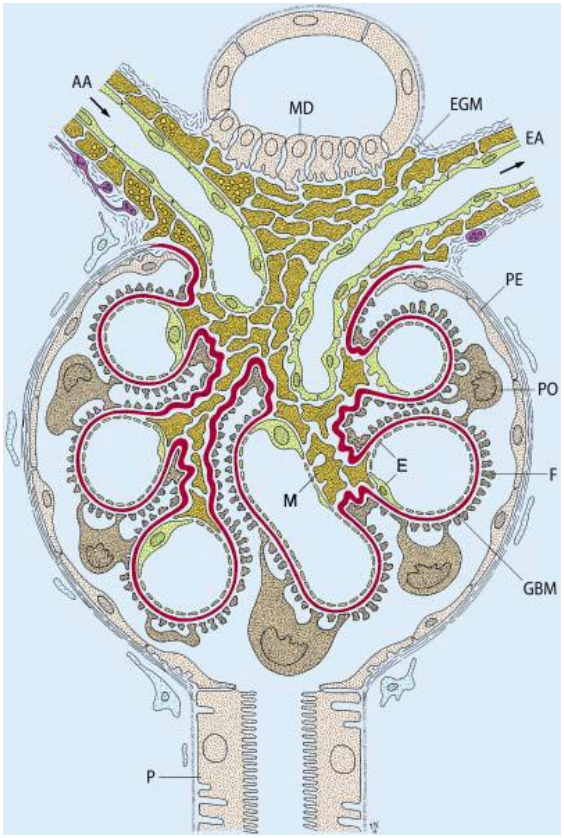

[B]

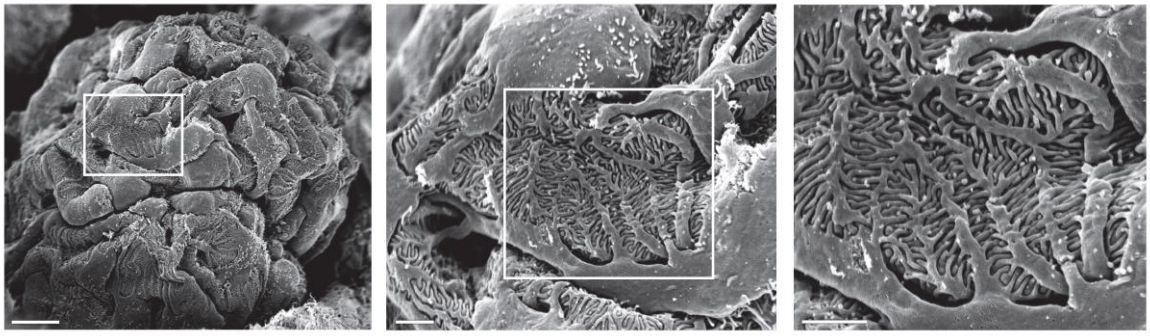

Figure 1.2: Structure of the glomerulus.
[A] Schematic representation of a longitudinally dissected renal corpuscle. Blood capillaries enter the renal corpuscle through the afferent arteriole (AA) and leave the glomerulus through the efferent arteriole (EA). Between the arterioles, the extraglomerular mesangium (EGM) is located and attached to the distal tubulus forming the macula densa (MD). Blood filtration occurs at the glomerular filtration barrier which comprises the fenestrated endothelium (E), the glomerular basement membrane (GBM, red), and the interdigitating foot processes (F) originating from the podocyte cell bodies (PO). The mesangium (M) composes the axial skeleton of the glomerular tuft consisting of contractile mesangial cells which secrete the mesangial matrix. At the vascular pole, the podocyte epithelium changes into the parietal epithelium (PE) of the Bowman´s capsule. At the tubular pole, the proximal convoluted tubule (P) arises (Kriz 2006). **[B]** Scanning electron micrograph of a glomerulus of a C57BL/6 mouse at the age of 3 months. Illustration of interdigitating foot processes of neighboring podocytes. Scale bar left panel 10 µm, middle and right panel 2 µm (Burghardt *et al.* 2015).

1.3 The glomerular filtration barrier (GFB)

The filtration barrier of the kidney is a complex structure acting as a molecular filter system: on the one hand water and dissolved substances are able to freely pass the barrier, on the other hand plasma proteins and necessary substances should be restrained. In order to achieve the transition from blood to primary urine, a highly effective system built up by three layers accomplishes this particular filtration process. The barrier is composed of an inner fenestrated endothelium, the glomerular basement membrane, and the foot processes of the podocytes (Figure 1.3, [A]). The molecular mechanism of blood filtration is still unknown, but all three layers are thought to be involved during filtration (Moeller & Tenten 2013). Dissolved substances leave the capillary lumen through the fenestrations and enter the Bowman´s space after passing the glomerular basement membrane and the slit diaphragm of the podocytes. Damage to any of these three layers can lead to protein and blood cell loss via the urine that are usually restricted in the blood and not able to pass the size and charge selective filtration barrier (Jarad & Miner 2009).

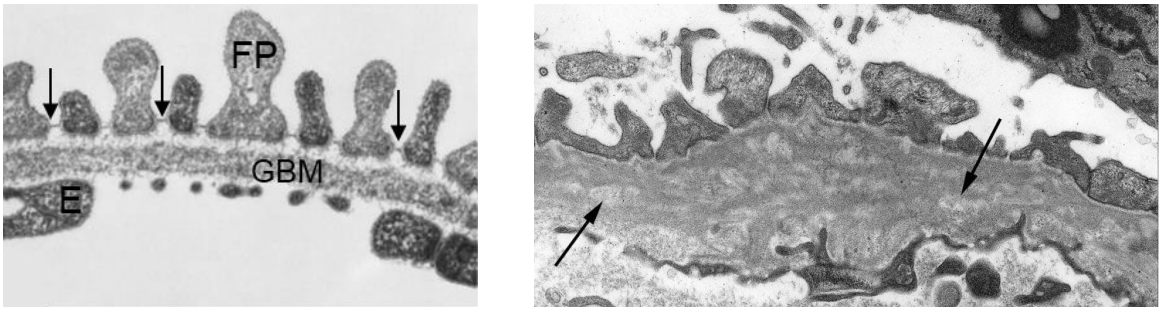

[A] Healthy GFB [B] Impaired GFB

Figure 1.3: Picture of the GFB on an ultrastructural level.
[A] Detailed demonstration of the ultrastructural composition of the glomerular filtration barrier of a healthy person. The barrier comprises the fenestrated endothelium (E), the glomerular basement membrane (GBM) including *Lamina rara interna*, *Lamina rara densa*, and *Lamina rara externa* and the interdigitating foot processes of the podocytes (FP), which build up the slit diaphragms (arrows). Adapted from (Kriz 2006). **[B]** Image of the ultrastructural changes in the glomerular filtration barrier of nail-patella syndrome patients. The glomerular basement membrane is markedly thickened and shows a moth-eaten appearance (arrows). In addition patients show a loss of podocyte foot processes (Heidet *et al.* 2003).

1.3.1 The fenestrated endothelium

The endothelium of glomerular capillaries differs from a “common” endothelium in the following points: glomerular endothelial cells appear flatter than normal endothelial cells and they form large pores, so-called fenestrae, without diaphragms between single endothelial cells (Ballermann 2005). These fenestrations have a diameter of 60 – 80 nm and occupy roughly 40% of the capillary wall (Avasthi *et al.* 1980; Lea *et al.* 1989). It was long time thought that the fenestrated endothelium is irrelevant for the filtration barrier due to its leaky pores (Satchell 2013). Indeed, studies approved the important role of the endothelium during blood filtration while showing proteinuria regardless of alterations in the glomerular basement membrane or the podocyte structure (Eremina *et al.* 2008; Fridén *et al.* 2011; Satchell & Braet 2009; Sugimoto *et al.* 2003). The signal molecule VEGF-A, which is synthesized by podocytes, plays an essential role in formation and maintenance of endothelial cell fenestrations (Ballermann 2005). Furthermore, the glomerular endothelium is covered by a negatively charged glycocalyx comprising proteoglycans, glycoproteins, and sialic acids, which are anchored at the cell surface (Reitsma *et al.* 2007; Weinbaum *et al.* 2007). Soluble proteins such as hyaluronic acids are excreted and build up a gel-like dynamic structure, the so-called endothelial surface layer (Pries *et al.* 2000). Due to the negative charge and its gel-like structure, the fenestrated endothelium is thought to act as a size-selective filter and in addition as an electrostatic barrier (Jeansson & Haraldsson 2003). Consequently, the glycocalyx refers to be of major importance for proper blood filtration.

1.3.2 The glomerular basement membrane

The glomerular basement membrane is the basal lamina of the glomerulus and is located between the fenestrated endothelium and the podocytes (Figure 1.3, [A]). It is composed of basal laminae, which are excreted during nephrogenesis from both the endothelial cells and the visceral epithelial cells, later podocytes (Abrahamson 1985; St John & Abrahamson 2001; Jarad *et al.* 2006) receiving a triple-layered structure: *Lamina rara interna, Lamina densa* and *Lamina rara externa* (Farquhar 2006). Important proteins of the basement membrane are nidogen, heparin sulfate proteoglycans, laminin-521, type IV collagen (collagen α3α4α5 and to a lesser extent collagen α1α1α2) and agrin (Timpl 1989; Lennon *et al.* 2014a). A previous study revealed by use of ultra-resolution microscopy that the proteoglycan agrin and the C-terminal end of laminin-521 are located near to the podocytes, whereas collagen α1α1α2 (IV) is located in the vicinity of the endothelial cells. In addition, collagen α3α4α5 (IV) and nidogen form the *Lamina densa* of the basement membrane (Suleiman *et al.* 2013). The proteins of the glomerular basement membrane have a high negative charge preventing blood proteins, that feature per se an anionic nature, to pass the barrier. The cell-matrix contacts of podocytes are ensured by α3β1-integrin binding to the C-terminal domain of laminin-521.

The importance of a proper glomerular basement membrane structure for blood filtration could be emphasized by two hereditary glomerular diseases caused by mutations of glomerular basement membrane proteins. One of them is the Pierson syndrome, which is based on mutations in the *LAMB2* gene encoding for β2 chain of laminin (Zenker *et al.* 2004). The symptoms of these patients vary widely depending on the type of mutation, but invariably lead to death in childhood. Truncating mutations are known to generate a more severe phenotype than missense mutations (Matejas *et al.* 2010). Patients with Pierson syndrome develop congenital nephrosis with mesangial sclerosis and distinct eye abnormalities (Zenker *et al.* 2004; Choi *et al.* 2008). *Lamb2* knock-out mice exhibit defects in the glomerular filtration barrier, in the development and organization of the neuromuscular junction, and in the retina. In addition those mice develop a massive proteinuria and die very small at three weeks of age (Miner *et al.* 2006; Noakes *et al.* 1995). Remarkably, proteinuria was detectable shortly after birth, but the loss of slit diaphragms and changes in podocyte foot process structure initially appeared in

week two. These findings indicate that Laminin β2 (LAMB2) is required for proper functioning of the glomerular filtration barrier (Jarad *et al.* 2006).

The second hereditary glomerular basement membrane disease, the Alport syndrome, is caused by mutations in the *COL4A3*, *COL4A4* or *COL4A5* genes encoding collagen type IV α3, α4 or α5 chains, respectively. Alport syndrome is associated with a progressive glomerular disease, hearing loss, and lens defects (Chew & Lennon 2018). During renal development, initial collagen α1α1α2(IV) is replaced by collagen α3α4α5(IV) that fails to appear in Alport syndrome patients (Kalluri *et al.* 1995). Alterations in glomerular basement membrane composition leads to a membrane thickening and splitting. Since the glomerular disease develops for years, one can imagine that collagen α3α4α5(IV) is not preliminary necessary for blood filtration, but is essential for signaling to podocytes (Tryggvason & Wartiovaara 2001; Gross *et al.* 2004). In 2012, a longitudinal study confirmed that ACE inhibitors delayed the progression of end-stage renal disease in Alport syndrome patients suggesting a first therapeutic option for patients (Gross *et al.* 2012).

1.3.3 The podocytes

The outermost layer of the glomerular filtration barrier is represented by specialized and terminally differentiated epithelial cells: the podocytes. The location, the architecture, and the relevance of this cell type is unique. Essential for the glomerular structure, podocytes cover the exterior of the glomerular capillaries and are responsible for the slit diaphragm formation of interdigitating foot processes. This molecular filter prevents proteins depending on their size, such as albumin or even larger proteins, from the release into the Bowman´s capsule. Until today, intense research on podocytes could reveal a multitude of hereditary renal diseases, such as nail-patella syndrome, congenital nephrotic syndrome or focal segmental glomerulosclerosis (FSGS), that are caused due to the damage and functional loss of the podocytes (Pavenstädt *et al.* 2003).

Cytoarchitecture of podocytes

Podocytes are highly differentiated cells that have a voluminous cell body protruding into the Bowman´s space while being anchored to the glomerular basement membrane by its arborizing cellular extensions (Pavenstädt *et al.* 2003). Primary foot processes project from the floating podocyte cell body and branch into secondary and tertiary so-called foot processes (Burghardt *et al.* 2015). Since podocytes are located on the outside of the glomerular capillary, they are exposed to tremendous physical forces, which are required for efficient glomerular filtration. Foot processes are not only involved in the formation of the filtration barrier, but are also essential for increasing the surface and thereby mediating a proper attachment to the glomerular basement membrane (Kobayashi 2002; Lennon *et al.* 2014b; Schell & Huber 2017). Those foot processes always interdigitate with foot processes of a neighbored podocyte forming specialized cell-cell junctions so-called slit-diaphragms (Burghardt *et al.* 2015; Conti *et al.* 2017; Grahammer 2017). Early studies from the 1980s showed that primary and secondary foot processes harbor unique cytoskeletal components and characteristics employing immune-gold-labeled electron microscopy (Andrews & Bates 1984; Drenckhahn & Franke 1988). The podocyte´s backbone is served by an abundantly rich actin cytoskeleton, which enables podocytes to continually and dynamically alter shape in addition to guarantee the static function (Mundel *et al.* 1997). The cytoskeleton is built up by three distinct ultrastructural elements: 1) microfilaments (7-9 nm diameter), intermediate filaments (10 nm), and microtubules (24 nm). Microfilaments are predominantly located in the foot processes and contain a dense network of F-actin and myosin. For maintaining the podocyte shape, actin-binding proteins such as synaptopodin and α-actinin-4 play a crucial role. Whereas primary foot processes are predominantly stabilized by intermediate filaments and microtubules, such as desmin and vimentin, secondary processes are mainly based on a tightly regulated actin cytoskeleton including myosin-2, α-actinin-4, talin, vinculin, paxillin, and synaptopodin (Asanuma *et al.* 2005; Shankland 2006). As podocytes are not able to replicate by mitosis, a replacement of dead or detached cells is not possible (Kriz 2019). A podocyte loss can be partly substituted by parietal and progenitor cells (Shankland *et al.* 2014), but also by means of hypertrophy of neighboring podocytes

(Wiggins 2007). For maintenance of a proper blood filtration, the podocyte architecture is of particular importance since alterations evoke proteinuria.

Podocyte injury and foot process effacement

Progressive podocyte loss is the most frequent cause of glomerular diseases leading to end-stage renal failure. The response of podocytes to injury and stress occurs in a unique way. Injured podocytes can be divided into three groups: Besides those podocytes that develop excessive hypertrophy or those that indicate an increased turnover of cell material, the most general alteration in injured podocyte cell structure is the loss of the interdigitating foot process pattern. The retraction of the foot processes results in a broad, uniform layer and is accompanied by loss of slit diaphragms, termed foot process effacement (Kriz *et al.* 2013). The pathological rearrangement process can clearly be distinguished into two stages: Within the first stage, the shape of foot processes changes due to the loss of the regular interdigitating pattern resulting in irregularly shaped cell projections (George *et al.* 2012). The slit diaphragms are lost or displaced from their original position and replaced by occludens-type junctions between deformed foot processes. In the second phase, the foot processes retract into the primary podocyte cell processes forming a broad flattened, disc-like cell without any processes, which directly adhere to the glomerular basement membrane (Kriz *et al.* 2013). On the molecular level, podocyte foot process effacement is accompanied by alterations in the expression levels of actin cytoskeleton-related proteins (Shirato *et al.* 1996; Smoyer *et al.* 1997) in addition to changes in the action cytoskeleton structure (Shirato 2002). In particular, genetic defects in actin-binding proteins such as α-actinin-4 lead to the autosomal dominant FSGS with patients suffering from a progressive renal failure including proteinuria (Kaplan *et al.* 2000).

Another protein, that is known to interact with actin inside the podocyte, is synaptopodin. After application of protamine sulfate, synaptopodin-null mice showed an abnormal recovery from the induced foot process effacement (Asanuma *et al.* 2005). Moreover, it has to be mentioned that synaptopodin directly interacts with α-actinin-4 by elongating α-actinin-4-induced filaments (Asanuma *et al.* 2005). Synaptopodin seems to play a crucial role in maintaining normal podocyte shape. This is presumably achieved by altering the α-actinin-4 function (Shankland 2006).

Taken together, these results emphasize the importance of the actin cytoskeleton for podocyte cell structure and function.

Structure of cell-cell contacts: the slit diaphragms

During filtration, the plasma passes through the fenestrated endothelium and the glomerular basement membrane before it reaches a special part of the filtration barrier: the slit diaphragm (Figure 1.4). This is a specialized type of intercellular junctions connecting podocyte foot processes of neighboring podocytes (Grahammer *et al.* 2013). Slit diaphragms feature a 40 nm wide structure including a network of convoluted strands that form the scaffold of the slit diaphragm (Tryggvason *et al.* 2006). Initially, it was thought to be organized in a zipper-like model of a sieve with pores that were 5 nm wide and 15 nm long, smaller than the size of albumin (Rodewald & Karnovsky 1974; Wartiovaara *et al.* 2004). Recent studies could validate by electron tomography the presence of more than just one layer of cell-cell contacts (Burghardt *et al.* 2015; Grahammer *et al.* 2016). However, both studies clearly demonstrate two types of cell-cell contacts at different basolateral positions. There is still the contradiction whether one of the distinct contacts consists of a continuous layer or just single spots of filamentous structures. Due to the fact, that many mutations in genes encoding for slit diaphragm proteins lead to podocyte foot process effacement and proteinuria, the slit diaphragm seems to control the structure and function of the glomerular filtration. In 1998, mutations in *NPHS1* encoding for the immunoglobulin superfamily molecule, nephrin, were identified to cause congenital nephrotic syndrome of the Finnish type (Kestilä *et al.* 1998; Grahammer *et al.* 2013). As main components of the slit diaphragm, nephrin and the shorter structurally related Neph1 (Donoviel *et al.* 2001) straddle the gap between neighboring podocyte foot processes. A knock-out of these genes in mice leads to foot process effacement, proteinuria, and early death. Moreover, several other slit diaphragm proteins, such as podocin (Boute *et al.* 2000), protocaderin Fat 1 (Ciani *et al.* 2003), and the ion channel TrpC6 (Reiser *et al.* 2005; Winn *et al.* 2005) have been identified to be important for the slit diaphragm formation. In addition, mutations in genes for molecules linking the slit diaphragm to the actin cytoskeleton, such as CD2-associated protein (CD2AP) were approved as being associated with proteinuria in mice (Shih *et al.* 1999). The protein podocin is encoded by *NPHS2*

and is almost exclusively expressed in podocytes binding to nephrin (Huber *et al.* 2001), Neph1 (Sellin *et al.* 2003), and CD2AP (Schwarz *et al.* 2001). Since *Nphs2* knock-out mice develop severe proteinuria and die early after birth due to renal failure, podocin plays a central role in signaling and slit diaphragm protein recruitment (Roselli *et al.* 2004). Zonula occludens-1 (ZO-1) was described as the first protein localizing to the cytoplasmic basis of the slit diaphragms (Schnabel *et al.* 1990). In a previous study ZO-1 was shown to potentially organize nephrin proteins and recruit signal transduction components to the slit diaphragm of podocytes (Huber *et al.* 2003). In summary, the slit diaphragm is an intriguing and unique cell-cell contact that seems to control the structure and function of the glomerular filtration barrier. An array of highly specialized functions are executed by the slit diaphragm numbering among: forming the filter, anchoring the sieve to the glomerular basement membrane, connecting the slit diaphragm via adaptor proteins to the actin cytoskeleton, and initiating signals that regulate the plasticity of podocyte foot processes (Grahammer *et al.* 2013).

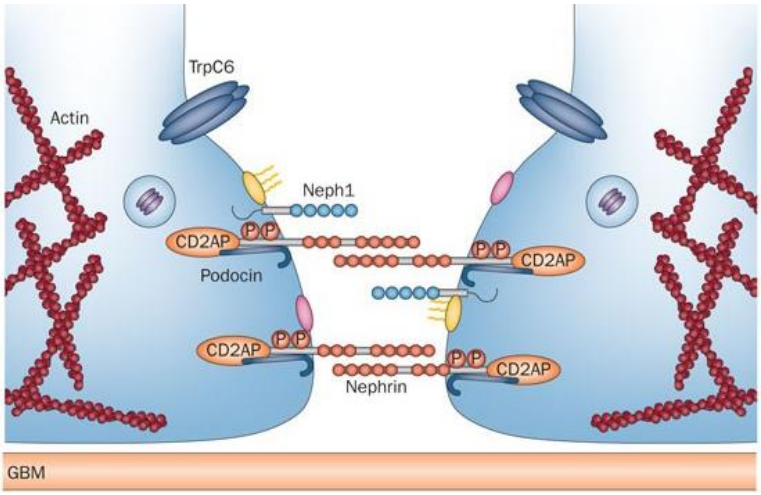

Figure 1.4: Molecular composition of the podocyte slit diaphragm.
During development, podocytes are initially bridged via tight-junction and gap-junction components, which are stepwise replaced by the neuronal-junction components nephrin, podocin, and Neph1. *Abbreviations:* (CD2AP), CD2-associated protein; (GBM), glomerular basement membrane; (P), phosphorylated residues; (NEPH1), nephrin-like protein 1; (TrpC6), transient receptor potential channel 6 (Grahammer *et al.* 2013).

Composition of cell-matrix contacts

While the cell bodies of podocytes protrude into the Bowman´s space, the podocyte foot processes are anchored to the glomerular basement membrane by several transmembrane proteins that are located at their foot processes (Figure 1.5). Podocytes are constantly exposed to mechanical stress, therefore a tight adhesion to the glomerular basement membrane is required for proper blood filtration (Sachs & Sonnenberg 2013). Intact foot processes are attached to the glomerular basement membrane by various integrin dimers and by α- and β-dystroglycans. It was previously shown, that a decreased number or strength of cell-matrix contacts may lead to podocyte detachment and loss (Kriz *et al.* 2013). In addition, mutations in components mediating podocyte-matrix adhesion lead to impairment of the glomerular basement membrane, podocyte foot process effacement, and proteinuria (Sachs & Sonnenberg 2013). Various adapter and signaling proteins connect the adhesion receptors to the actin cytoskeleton. A major protein family that is responsible for cell-matrix adhesion is the integrin family. Integrins belong to type I transmembrane proteins and form αβ-heterodimers. The most important integrin heterodimer in podocytes are α3β1-integrins. These integrins build focal adhesion complexes that specifically bind laminins of the glomerular basement membrane and are additionally anchored to the actin cytoskeleton of the foot processes via talin, vinculin and paxillin (Faul *et al.* 2007). Focal adhesions are clusters of proteins that connect the extracellular matrix to the actin cytoskeleton (Zaidel-Bar *et al.* 2004) and are essential for podocyte function and renal filtration. Several other focal adhesion proteins, such as vinculin (Lausecker *et al.* 2018), integrin-linked kinase (El-Aouni *et al.* 2006), and tetraspanin CD151 (Sachs *et al.* 2006) have been described to form crucial parts of the podocyte adhesion plaque.

A second extracellular link to the actin cytoskeleton in podocytes is accomplished by the adhesion receptor dystroglycan (Ervasti & Campbell 1993; Durbeej *et al.* 1998). However, fixation of the podocyte to the extracellular matrix is necessary, dystroglycan seems not to be of critical importance, since a deletion in murine podocytes does not evoke any renal impairment both under normal conditions and stress (Jarad *et al.* 2011).

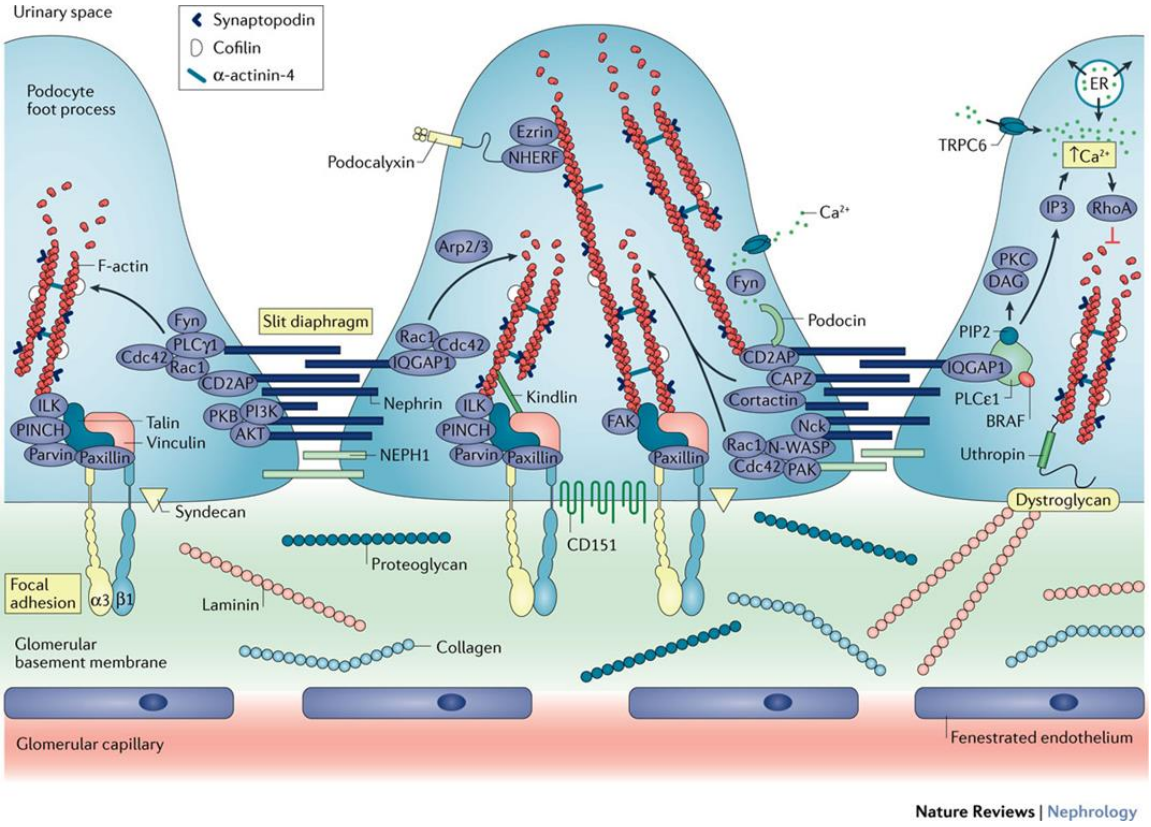

Figure 1.5: Podocyte cell-matrix proteins.

At the interface with the glomerular basement membrane, podocyte foot processes express integrins, dystroglycans, and syndecans, which generate a tight adhesion to the extracellular matrix. *Abbreviations:* (ILK), integrin-linked kinase; (FAK), focal adhesion kinase; (NEPH1), nephrin-like protein 1; (TRPC6), transient receptor potential channel 6; (CD2AP), CD2-associated protein; (RhoA) small GTPase transforming protein RhoA; (Rac1), related C3 botulinum toxin substrate 1; (Cdc42), cell division control protein 42 homologue; (α3β1), integrin α3β1; (Arp2/3), actin-related protein 2/3; (BRAF), serine/threonine-protein kinase B-raf; (Ca^{2+}), calcium; (CAPZ), F-actin capping protein; (DAG), diaglycerol; (ER), endoplasmic reticulum; (F-actin), filamentous actin; (Fyn), tyrosine-protein kinase Fyn; (IP3), inositol 1,4,5-triphosphate; (IQGAP1), Ig-motif containing GTPase-activating protein 1, (NHERF), Na^{+}/H^{+} exchange regulatory cofactor; (N-WASP), neural Wiskott-Aldrich syndrome protein; (PAK), p21-activated kinases; (PINCH), particularly interesting new Cys-His protein 1; (PIP2), phosphatidylinositol biphosphate; (PI3K), phosphoinositide 3-kinase; (PKC), protein kinase C; (PLCε1), phospholipase Cε1; (PLCγ1), phospholipase Cγ1 (Perico *et al.* 2016).

1.4 Nail-patella syndrome

Nail-patella syndrome (OMIM #161200) is an autosomal-dominant inherited disorder with an incidence of approximately 1:50 000 (Bongers *et al.* 2002). However, an epidemiologically based incidence estimate is still not available. The symptoms of patients with nail-patella syndrome appear both interfamilial and intrafamilial quite diverse. Between 95 – 100% suffer from dysplastic finger- and toenails (Figure 1.6, A) and between 74 – 93% from absent or hypoplastic patellae (Figure 1.6, B). In addition, iliac horns (68 – 81%; Figure 1.6, C), ocular symptoms like glaucoma (10 – 12%), ocular hypertension (4 – 7%) and iris hyperpigmentation (46 – 54%; Figure 1.6, D) occur. Most important for the prognosis are renal abnormalities (10 - 40%; Figure 1.3, B) (Witzgall 2017). Renal symptoms often develop over years and range from mild proteinuria and hematuria to end-stage renal-disease (Sweeney *et al.* 2003). Nail-patella syndrome is caused by mutations of the gene encoding the LIM homeobox transcription factor 1 beta (LMX1B) (Dreyer *et al.* 1998; McIntosh *et al.* 1998; Vollrath *et al.* 1998).

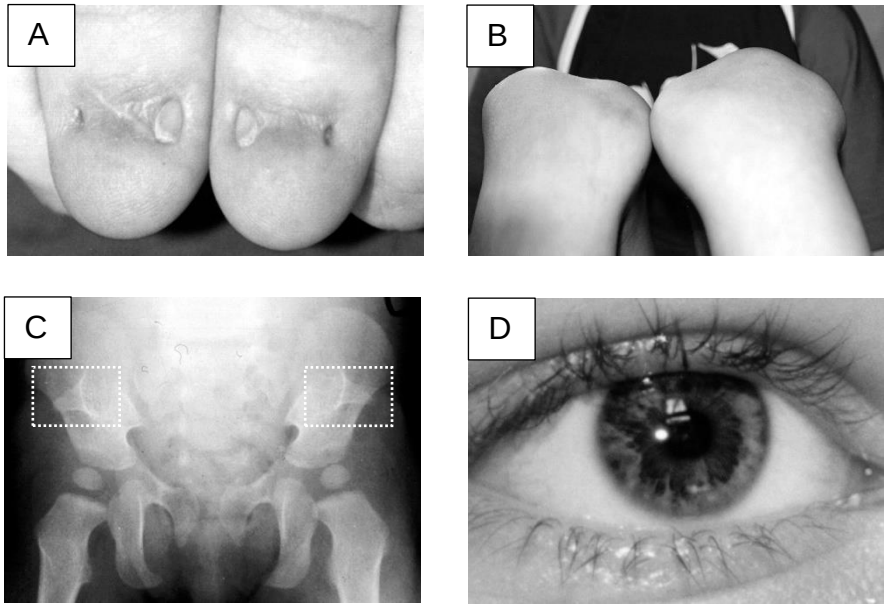

Figure 1.6: Symptoms of nail-patella syndrome patients.
[A] Thumbnails with severe dysplasia on the ulnar border of the thumbnail. **[B]** Subluxation of patellae on knee flexion. **[C]** Iliac horns of pelvis. **[D]** Lester´s sign of the iris. (Sweeney *et al.* 2003).

1.5 The transcription factor LMX1B

1.5.1 Structure and mutations

The *LMX1B* gene is located on the human chromosome 9q34 and is composed of eight exons (Vollrath *et al.* 1998), which give rise to a ~7-kb mRNA (Dreyer *et al.* 1998). LMX1B comprises two NH_2-terminal LIM domains, which are described to be important for protein-protein interactions. In addition LMX1B contains a central homeodomain, known to bind DNA (Figure 1.7) (Witzgall 2017). The first LIM domain is encoded by exon 2, the second LIM domain by exon 3 and are separated by a spacer of eight amino acids. Moreover, LMX1B contains a central homeodomain essential for DNA binding, which is encoded by exons 4 to 6 (Vollrath *et al.* 1998). The C-terminal glutamine- and serine-rich region is of unknown function (Bongers *et al.* 2002). In 1998, for the first time, two different isoforms of LMX1B were reported in human, one of 372 amino acids in length (Dreyer *et al.* 1998) and one of 379 amino acids in length (Vollrath *et al.* 1998). This phenomenon was described by alternative splicing of the last 21 nucleotides of exon 7 (Seri *et al.* 1999). Later, additional 23 amino acids at the NH_2-terminus of unknown function were discovered in the human LMX1B protein because a start codon further upstream of the original one was identified. As a result, we are literally dealing with isoforms of 395 and 402 amino acid in length, respectively (Dunston *et al.* 2004). In this thesis, the reference sequence of *LMX1B*/*Lmx1b* referred to the first NCBI RefSeq. number: NM_002316.2, NP_002307.1 transcript variant 1 in human and to NCBI RefSeq.: NM_010725.3, NP_034855.3 in mice were used due to later nomenclature of *Lmx1b* knock-in mouse design.

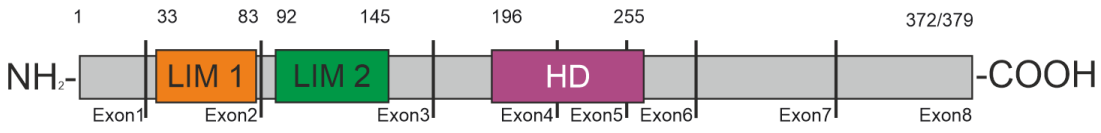

Figure 1.7: Modular structure of the transcription factor LMX1B.
The transcript of LMX1B with either 372 or 379 amino acids in length, contains two NH_2-terminal LIM domains (LIM 1 and LIM 2) and a central homeodomain (HD). Numbers above indicate amino acid positions.

The majority of mutations evoking nail-patella syndrome are described to be located in exons 2 to 6 (Human Gene Mutation Database at the Institute of Medical Genetics in Cardiff, http://www.hgmd.org/) by affecting the proper function of the LIM domains and of the homeodomain. Most of these mutations cluster in missense mutations leading to the substitution of amino acids, which are essential for the binding of zinc in the LIM domains. In case of a missense mutation within the homeodomain, LMX1B binding to the DNA is affected. Alternatively, the spectrum of mutations comprises in addition nonsense and frame-shifting mutations, which lead to the loss of LMX1B protein sequence beyond the mutation. Almost no mutations in the region of the *LMX1B* gene downstream of the homeobox have been identified. So far indicating no major importance for the LMX1B function (Witzgall 2017). In developing mice, Lmx1b is expressed in the kidney, brain, spinal cord, and the eye (Dunston *et al.* 2005). Within the kidney, Lmx1b is exclusively expressed in podocytes not only at embryonic stages but also in adult individuals (Morello & Lee 2002).

1.5.2 Linkage to nail-patella syndrome

Different parts of the skeletal system and a variety of organs are affected in patients with nail-patella syndrome. It was not immediately clear whether only one gene was mutated in those patients. The genetical linkage of nail-patella syndrome to the ABO locus was found in 1955 (RENWICK & LAWLER 1955). More than 40 years later mutations in *LMX1B* were determined to be the cause of the syndrome (Dreyer *et al.* 1998; McIntosh *et al.* 1998; Vollrath *et al.* 1998). The expression pattern of LMX1B can be reflected by the nail-patella syndrome symptoms (also see chapter 1.1). In addition to the importance of LMX1B for establishing the dorsoventral pattern in limb development, LMX1B is also expressed in the anterior segment of the eye (Pressman *et al.* 2000), in the brain (Adams *et al.* 2000) and in the podocytes of the kidney (Dreyer *et al.* 1998; Morello *et al.* 2001).

1.5.3 Functions of the LIM domains and interaction partners

So far, two interaction partners are identified binding to the LIM domains of LMX1B (Witzgall 2017). The E47 protein is encoded by the *E2A* gene, which is transcribed into an alternatively spliced mRNA, the E12 protein is the product of the other splice variant. The E47 protein is known to strongly increase the transcriptional activity of LMX1B by binding the LIM B domain of LMX1B (Dreyer *et al.* 2000; Johnson *et al.* 1997). Another interaction partner was the LDB1 protein, which shows the opposite effect to E47 (Dreyer *et al.* 2000; Marini *et al.* 2010). On closer consideration, the interaction of E47 and LDB1 with the closely related protein LMX1A seems to be more complex. Coincidentally, LDB1 downregulated the transcriptional activity of LMX1A but only in the presence of the E47 protein. When E47 was absent, no effect of LDB1 was detected (Jurata & Gill 1997). LDB1 is known to interact with the ubiquitin ligase RLIM and with SSDP1 (single-stranded DNA-binding protein1). In turn, RLIM leads to the proteasome-dependent degradation of LDB1 (Hiratani *et al.* 2003; Ostendorff *et al.* 2002), and SSDP1 promotes the transcriptional activation by LIM-homeodomain transcription factors (Nishioka *et al.* 2005). Moreover, previous studies presented an interaction of LMX1B and PAX2 (Marini *et al.* 2005) and with the paraspeckle protein 1 (PSPC1) (Hoekstra *et al.* 2013), but the relevance of these interactions in podocytes is not clarified at present.

1.5.4 Pathogenic mechanism of nail-patella syndrome

Nonsense and frameshift mutations lead to the synthesis of a truncated protein, moreover the pathogenetic effects of missense mutations in nail-patella syndrome are still not known. The few missense mutations that have been published, show a complete or partial loss LMX1B functionality (Bongers *et al.* 2008). The general assumption of the pathogenic mechanism is thought to be haploinsufficiency (Jiang *et al.* 2014), since described mutations showed a loss-of-function (Sato *et al.* 2005). This hypothesis is supported by the fact that whole deletions of *LMX1B* gene have been observed in nail-patella syndrome patients. The modular structure of LMX1B

prompts questions whether the severity of the symptoms in patients with nail-patella syndrome depends on the site of the mutation. So far, only one publication has reported a genotype-phenotype correlation, which describes mutations lying in the homeodomain, result in a stronger impact on the kidney function (Bongers *et al.* 2005). Interestingly, there is a study (Cross *et al.* 2014) reporting the identification of a missense mutation coding for Lmx1b (V242D), which shows a dominant-negative mode of action in mice, named *Lmx1b Icst*. In contrast to heterozygous *Lmx1b* knock-out mice, heterozygous *Lmx1b Icst* mice have buphthalmic eyes, display a glaucoma phenotype and some mice die due to development of postnatal kidney defects. These findings suggest another interpretation of the mode of action of mutant LMX1B in nail-patella syndrome (Cross *et al.* 2014).

1.5.5 Protein degradation pathways in the kidney

The amount of a respective protein in its functional state in the cell is required. In case of a misfolded or nonfunctional protein, physiological impairments develop finally resulting in a pathological condition. The amount of a specific protein is dependent on its transcriptional and post-transcriptional regulation, but rather from its turn-over. The proteome, meaning the total repertoire of cellular proteins of a cell, is determined by cellular processes of protein translation, folding, and degradation. Approximately 240 g protein are synthesized and degraded in a 60 kg adult human per day; the majority of which are intracellular proteins (Mitch & Goldberg 1996). Protein degradation is mainly achieved by two different processes: via the autophagosomal-lysosomal system and by the ubiquitin-proteasome system. In 2016, Yoshinori Ohsumi was awarded the Nobel Prize in Physiology or Medicine for his discoveries of mechanisms for autophagy. In his studies, he could show that autophagy controls important physiological functions by degradation and recycling of cellular components (Mizushima *et al.* 1998; Ohsumi 2014). Disrupted autophagy can be linked to several diseases, such as Parkinson´s disease, type 2 diabetes, cancer, but also to acute and chronic kidney diseases (Fujikake *et al.* 2018; Bhattacharya *et al.* 2018; Yun *et al.* 2018; Lenoir *et al.* 2016; Khandia *et al.* 2019).

Aside from the autophagosomal-lysosomal system, the proteolysis by the ubiquitin-proteasome system is accomplished by the synergy of specific enzymes. In 2004, Aaron Ciechanover, Avram Hershko and Irwin Rose were jointly awarded the Nobel Prize in Chemistry for the discovery of ubiquitin-mediated protein degradation. For proteasomal degradation, target proteins are ubiquitylated in a sequential, ATP-consuming process involving E1, E2, and E3 enzymes (Figure 1.8, [A]). The ubiquitin-activating enzyme E1 is responsible for ubiquitin-activation in mammalian cells. The E2 ubiquitin-conjugating and the E3 ubiquitin-ligating enzymes are involved in the transfer of the activated ubiquitin to the protein substrate. This mechanism finally results in a covalent bond between the carboxy-terminal carboxylate group of ubiquitin and a lysine, cysteine, serine or methionine of the target protein (Hershko *et al.* 2000; Meyer-Schwesinger 2019). Ubiquitylation is described as a reversible process meaning the removal of ubiquitin from substrates is tightly controlled by deubiquitylating enzymes (Figure 1.8, [B]). The activity of these enzymes represents an important role within the cell for recycling ubiquitin for

subsequent ubiquitylation reactions, for preventing a proteasome blocking, and for controlling protein turnover (Komander *et al.* 2009). Ubiquitin comprises seven lysine residues, Lys6, Lys11, Lys27, Lys29, Lys33, Lys48, and Lys63 forming up to seven different polyubiquitin chain linkages. The proteasome degrades branched polyubiquitylated proteins, in preference Lys48-linked polyubiquitylated proteins (Meyer & Rape 2014).

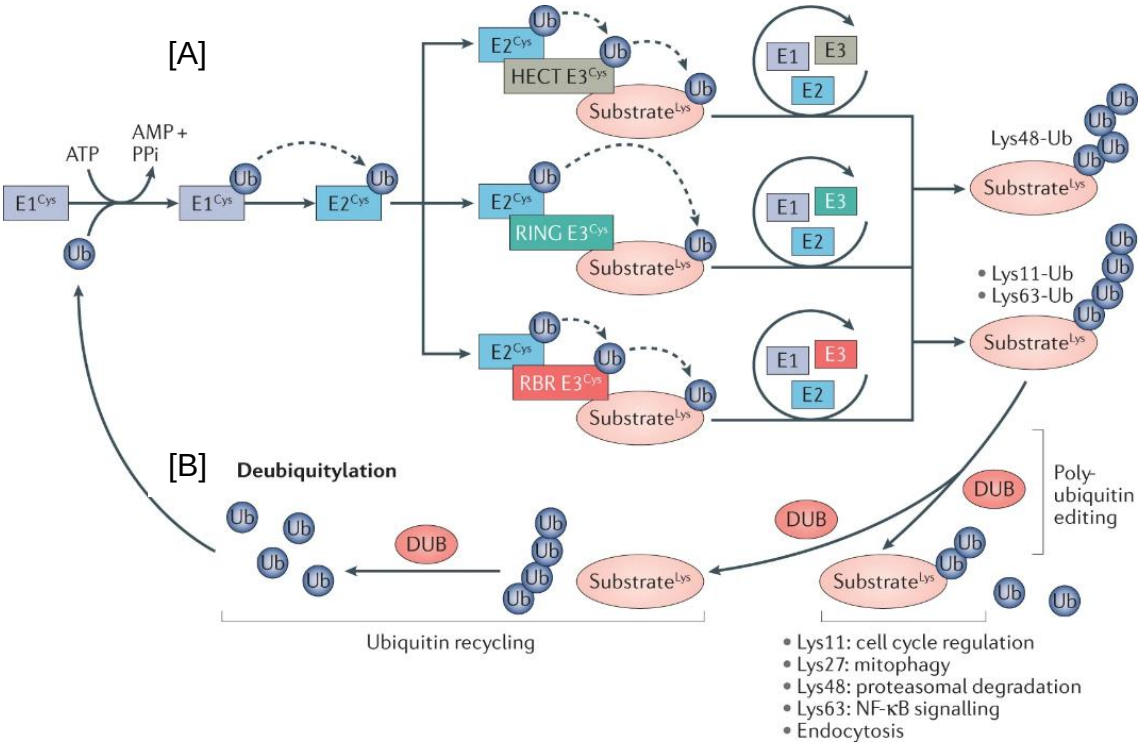

Figure 1.8 Ubiquitylation and deubiquitylation process.
[A] Covalent attachment of ubiquitin to the substrate protein by E1 ubiquitin-activating enzyme, followed by the transfer of the activated ubiquitin to the E2 ubiquitin-conjugating enzyme. Finally, with a specific E3 ligase, polyubiquitin is bound to a lysine residue of the substrate. **[B]** Deubiquitylating enzymes tightly control ubiquitylation by reversing and recycling of ubiquitin monomers. Abbreviations: (ATP), adenosine triphosphate; (AMP+PPi), adenosine monophosphate + pyrophosphate; (Ub), ubiquitin; (Cys), cysteine; (HECT) Homologous to the E6-AP Caroxyl Terminus; (RING), RING finger-like ligase; (RBR), RING-between-RING; (Lys), lysine; (DUB), deubiquitylating enzymes (Meyer-Schwesinger 2019)..

Despite ubiquitylation was long considered sufficient to mark proteins for degradation, previous studies validated that the presence of loosely folded regions within the substrate are additionally necessary for an efficient and rapid protein decay by the proteasome (Yu *et al.* 2016). Interestingly, recent studies could demonstrate that a protein degradation by the 20S proteasome does not necessarily require previous ubiquitin tagging or the presence of the 19S regulatory particle (Figure 1.9, [C]). It rather relies on the inherent structural disorder of the protein being degraded (Singh Gautam *et al.* 2012; Ben-Nissan & Sharon 2014). One example that has been identified as a substrate of the proteasome without pervious ubiquitin tagging is the enzyme ornithine decarboxylase, which is important for cell proliferation (Zhang *et al.* 2003).

The proteasome has a molecular mass of >2.5 MDa and consists of ~60 core subunits as well as other associated proteins of unknown functions. It is composed of a barrel-shaped proteolytic core complex, the 20S proteasome, and capped at both ends by the 19S regulatory complexes, which recognize ubiquitylated proteins. The regulatory sites are in addition implicated in unfolding and translocation of ubiquitylated substrates into the interior of the 20S complex. The 20S core complex contains 28 subunits which are arranged as a cylindrical stack of 4 rings, 2 outer α-rings and 2 inner β-rings (Figure 1.9, [A] and [B]). The α-rings serve as a gate for the substrate to enter the proteolytic chamber. Once the substrate has reached the proteolytic chamber, which is formed by the β-rings, it is cleaved to oligopeptides (Voges *et al.* 1999; Meyer-Schwesinger 2019). The subunits β1, β2, and β5 of the 20S core complex represent three distinct proteolytic activities such as the caspase-like activity (β1), the trypsin-like activity (β2), and the chymotrypsin-like activity (β5) (Meyer-Schwesinger 2019).

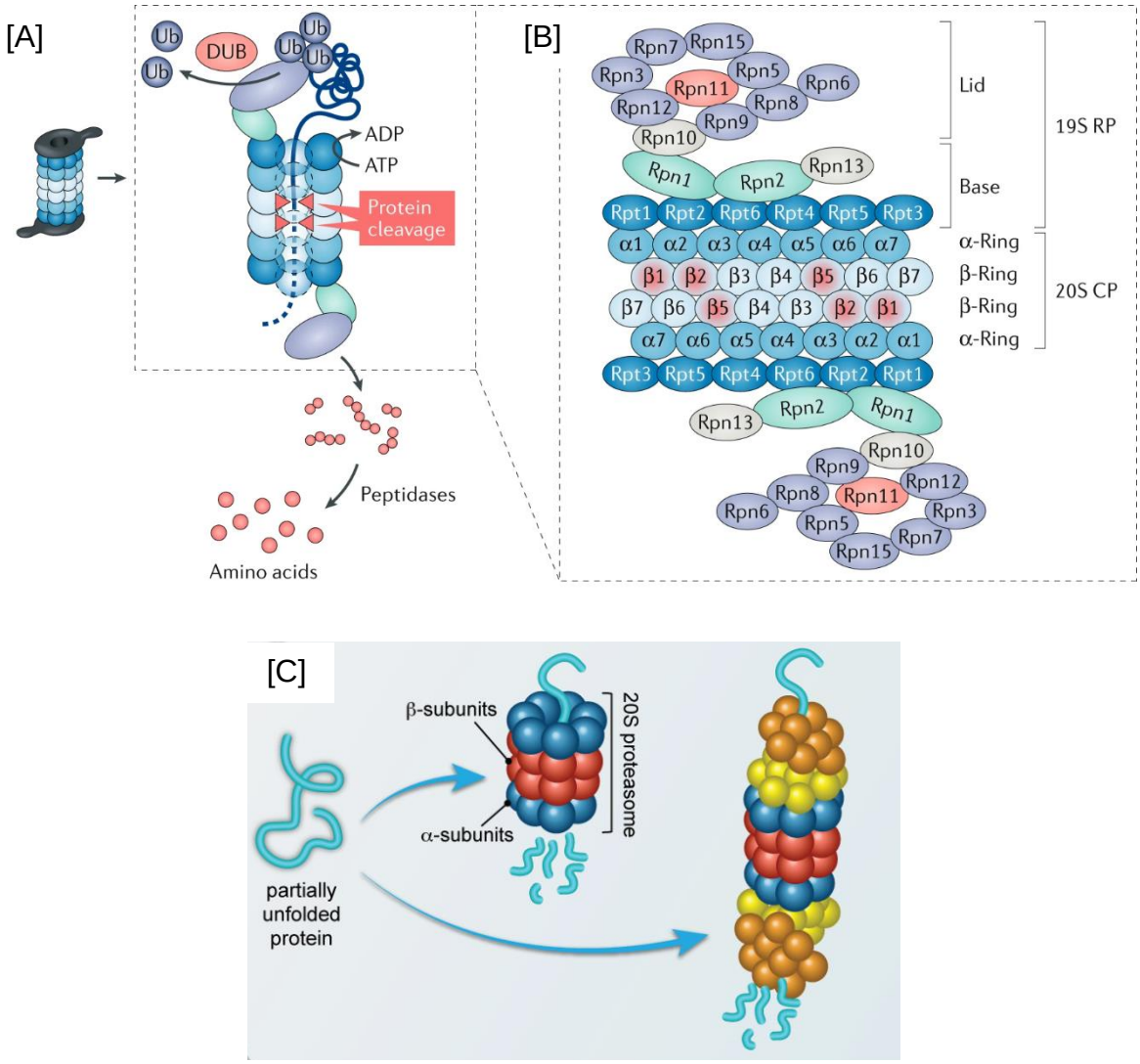

Figure 1.9: Proteasome composition.
[A] The proteasome is composed of a barrel-shaped 20S core particle with its cleavage site for proteolysis and a 19S regulatory particle. Initial association of the ubiquitin bound substrate with the proteasome is followed by proteasomes disassemble, release of the ubiquitin chain from the substrate and transfer of the deubiquitylated substrate into the proteolytic chamber, where it is degraded to peptides. These peptides are loaded on major histocompatibility complex class I molecules for antigen presentation or are further processed to amino acids by cytosolic peptidases. **[B]** The proteasome consists of a 19S regulatory particle, which is build up by a base and lid complex. The 20S core particle comprises four stacked rings containing either seven α or seven β subunits. The β1, β2, and β5 subunits incorporate the proteolytic activities of the 20S core particle. Abbreviations: (ATP), adenosine triphosphate; (ADP), adenosine diphosphate; (Ub), ubiquitin; (RP), regulatory particle; (CP), core particle; (Rpn), regulatory particle of non-ATPase subunit; (Rpt) regulatory particle of ATPase subunit (Meyer-Schwesinger 2019). **[C]** Ubiquitin-independent protein degradation by the 20S proteasome is accomplished due to the inherent structural disorder of loosely or misfolded proteins. Figure adapted from (Ben-Nissan & Sharon 2014).

1.6 Mouse lines

The inheritance pattern of nail-patella syndrome in humans differ from mice. Heterozygous *Lmx1b* knock-out mice exhibit no phenotype up to 12 months after birth (Rohr *et al.* 2002), thus, showing a recessive mode of inheritance. A convenient tool in order to study nail-patella syndrome apart from the cell culture had first to be implemented, to better understand the mechanism of the disease.

1.6.1 The conventional *Lmx1b* knock-out mouse

As previously shown by Chen et al. (1998), a constitutive inactivation of the *Lmx1b* gene in conventional *Lmx1b* knock-out mice reproduces many features of the human disease. Exons 2 – 7 are deleted by homologous recombination. In addition, there are important differences in the mode of inheritance. Homozygous *Lmx1b* knock-out mice die on the day of birth and feature skeletal defects (Chen *et al.* 1998a). Re-emphasizing the role of LMX1B during dorso-ventral axis formation, the conventional *Lmx1b* knock-out mice develop foot pads not only on the ventral but in addition on the dorsal side of their foot paws. Beyond the disturbed dorso-ventral patterning, these mice also display skeletal defects. In the forelimbs, the distal ulna is absent, and the scapula is smaller relative to that of wild-type animals. In addition, the clavicle is abnormally bent projecting along the surface to the scapula instead of away from it. The hindlimbs are affected in the iliac region of the pelvis and fibula. Unlike the ulna, the fibula is not missing, but those mice lack patellae. Furthermore, the skull of homozygous *Lmx1b* knock-out mice exhibit various clavaria-specific defects. The interparietal and supraoccipital bones are either absent or severely reduced. The sutures between frontal, parietal, and interparietal bones are severely anomalous due to an early ossification (Chen *et al.* 1998a; Dai *et al.* 2009). Homozygous *Lmx1b* knock-out mice also suffer from structural defects in the anterior portion of the eyes (Pressman *et al.* 2000). Another study described a drastic reduction in size of the tectum and cerebellum (Guo *et al.* 2008) and a loss of neuronal markers, such as serotonin (5-HT) and Pet1, in the raphe nuclei of the brain (Ding *et al.* 2003; Rohr *et al.* 2002) in homozygous *Lmx1b* knock-out mice.

Of most interest within the present work, are the effects in the kidney after inactivation of *Lmx1b*. The renal phenotype of homozygous *Lmx1b* knock-out mice can be described by a small size of the kidneys. The glomerular tuft appears smaller (Rohr *et al.* 2002) and so-called 'protein casts' can be found in the tubules referring to a leaky glomerular filtration barrier using light microscopy (Chen *et al.* 1998a). On an ultrastructural level this hypothesis can be confirmed by an arrest of the podocyte development in the cuboidal stage in addition to absent foot processes and slit diaphragms (Miner *et al.* 2002; Rohr *et al.* 2002). Further, the glomerular basement membrane is split in some capillary loops and finally the glomerular endothelial cells form less fenestrations in *Lmx1b* knock-out mice (Rohr *et al.* 2002). The genes *Col4α3*, *Col4α4*, and *Nphs2* are downregulated in the conventional *Lmx1b* knock-out mice, however this appears to be incoherent to the observations in nail-patella syndrome patients showing no affection of those genes.

1.6.2 Constitutive podocyte-specific *Lmx1b* knock-out

Since the conventional *Lmx1b* knock-out mouse (Chen *et al.* 1998a) does not represent a convenient tool to address the molecular pathways evoking podocyte foot process effacement and proteinuria, different models had to be implemented. One of these models is the constitutive podocyte-specific *Lmx1b* knock-out mouse (Figure 1.10) (Suleiman *et al.* 2007). A cassette encoding Cre recombinase was placed under control of the human 2.5 kbp promoter fragment of *NPHS2* (also referred to as "P2.5") leading to a podocyte-specific *Cre* expression (Moeller *et al.* 2003). For a Cre dependent recombination, *Lmx1b* is mutated by introducing *loxP* sites upstream of exon 4 and downstream of exon 6 resulting in a truncated Lmx1b protein lacking the homeodomain. Since the *Cre* expression is restricted to podocytes, the *Lmx1b* expression in other cell types remains unaffected. Homozygous podocyte-specific *Lmx1b* knock-out mice survive for approximately two weeks after birth while they develop foot process effacement associated with severe proteinuria. In addition, they mimic the human disease more closely since they show a downregulation of *Col4α3*, *Col4α4*, and *Nphs2* genes (Suleiman *et al.* 2007).

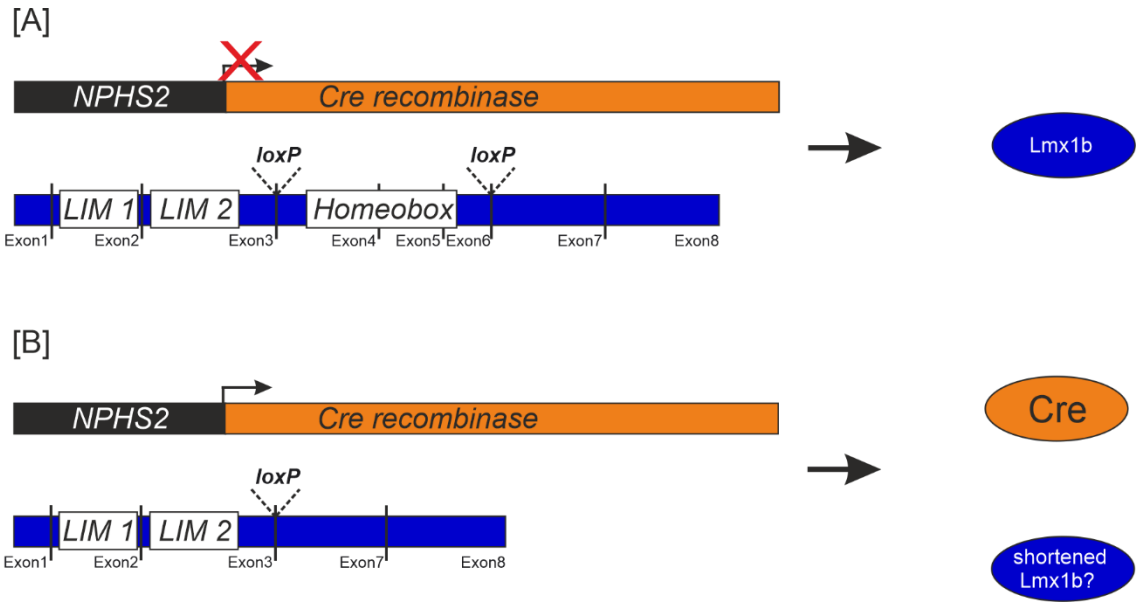

Figure 1.10: Demonstration of the podocyte-specific inactivation of *Lmx1b*. **[A]** In all cells of the murine organism except the podocytes, the 2.5 kbp promoter fragment of the *NPHS2* gene is inactive resulting in a full-length *Lmx1b* expression. **[B]** The *NPHS2* promoter is exclusively active in podocytes resulting in a tissue-specific Cre recombinase expression. Due to the location of *loxP*-sites in intron 3 and 6 of *Lmx1b* gene, the podocyte-specific Cre recombination leads to a deletion of the homeobox located in the exons 4 to 6. The deletion is in-frame and results in a shortened non-functional protein. Model according to (Setzer 2020).

1.6.3 Inducible podocyte-specific *Lmx1b* knock-out

Since LMX1B is not only expressed in the developing kidney, but also in mature podocytes, the protein might play a crucial role in maintenance of podocyte structure and function. Due to the perinatal lethality of the conventional *Lmx1b* knock-out mice and the death 14 days after birth of the constitutive podocyte-specific *Lmx1b* knock-out mice, research of the role of Lmx1b in podocyte maintenance is impossible by use of this mouse model. To study the function of Lmx1b in adult mice, an inducible, podocyte-specific *Lmx1b* knock-out mouse model was generated by crossing four single transgenic mouse lines: *Nphs2::*rtTA, *tetO::*Cre, *Lmx1b*$^{flox/flox}$, and *mTmG* (Burghardt *et al.* 2013). This model uses an enhanced version of the reverse tetracycline-controlled transcriptional transactivator (rtTA), which binds to tet operator sequences (*TetO*) in the presence of a tetracycline, for example

doxycycline (Tet-on system; (Urlinger *et al.* 2000)), Figure 1.11, [A.] Originally, the tetracycline controlled regulatory system arises from the *Escherichia coli* tetracycline-resistance operon (Gossen & Bujard 1992a). The *rtTA* gene is under *NPHS2* promoter control and therefore exclusively expressed in podocytes (Shigehara *et al.* 2003). The Cre recombinase construct contains seven *tetO* repeats flanked by two cytomegalovirus (CMV) minimal promoters resulting in a bidirectional promoter. This promoter controls the expression of the Cre recombinase due to firefly luciferase dependent rtTA binding (Schönig *et al.* 2002). Upstream of exon 4 and downstream of exon 6 of the *Lmx1b* gene, two *loxP* sites are inserted that lead to a recombination event of the respective exons through the Cre recombinase activity resulting in a deletion of exons 4 to 6. Finally, the mTmG reporter construct harbors a modified version of *tdTomato* (*mT*) under control of a chicken β-actin promoter and a CMV enhancer (*pCA*). Further downstream a polyadenylation sequence (*pA*) determines the ubiquitious expression of the membrane-targeted tdTomato. The sequence of *mT* and *pA* is in addition flanked by two *loxP* sites. In the presence of the Cre recombinase, the *mT* and *pA* sequence is also cut-out and the expression of the downstream membrane-targeted EGFP (mG) proceeds (Muzumdar *et al.* 2007).

In the absence of e.g. doxycycline, this transgene system leads to the expression of rtTA, Lmx1b, and mT. When doxycycline is present, the rtTA binds to the *tetO* promoter resulting in the Cre recombinase expression in podocytes, which evokes a recombination of *mTmG* and *Lmx1b*. The membrane targeted EGFP and the potential shortened version of Lmx1b are synthesized in the same podocytes, Figure ***1.11***, [B]. Nonetheless, these recombination events could be detected only in ~60% of podocytes by estimation of *Lmx1b* mRNA levels (Burghardt *et al.* 2013).

Inducible podocyte-specific *Lmx1b* knock-out mice show progressive proteinuria starting at day 5 of doxycycline administration via the drinking water. The proteinuria peaks at around two weeks and after four weeks, the severity of proteinuria decreases, but does not completely disappear. Mice survive the doxycycline administration for at least four weeks (Burghardt *et al.* 2013). Similar to the constitutive podocyte-specific *Lmx1b* knock-out, *Col4α3*, *Col4α4* and *Nphs2* genes are not downregulated after one week of doxycycline treatment, even though proteinuria has already developed (Burghardt *et al.* 2013).

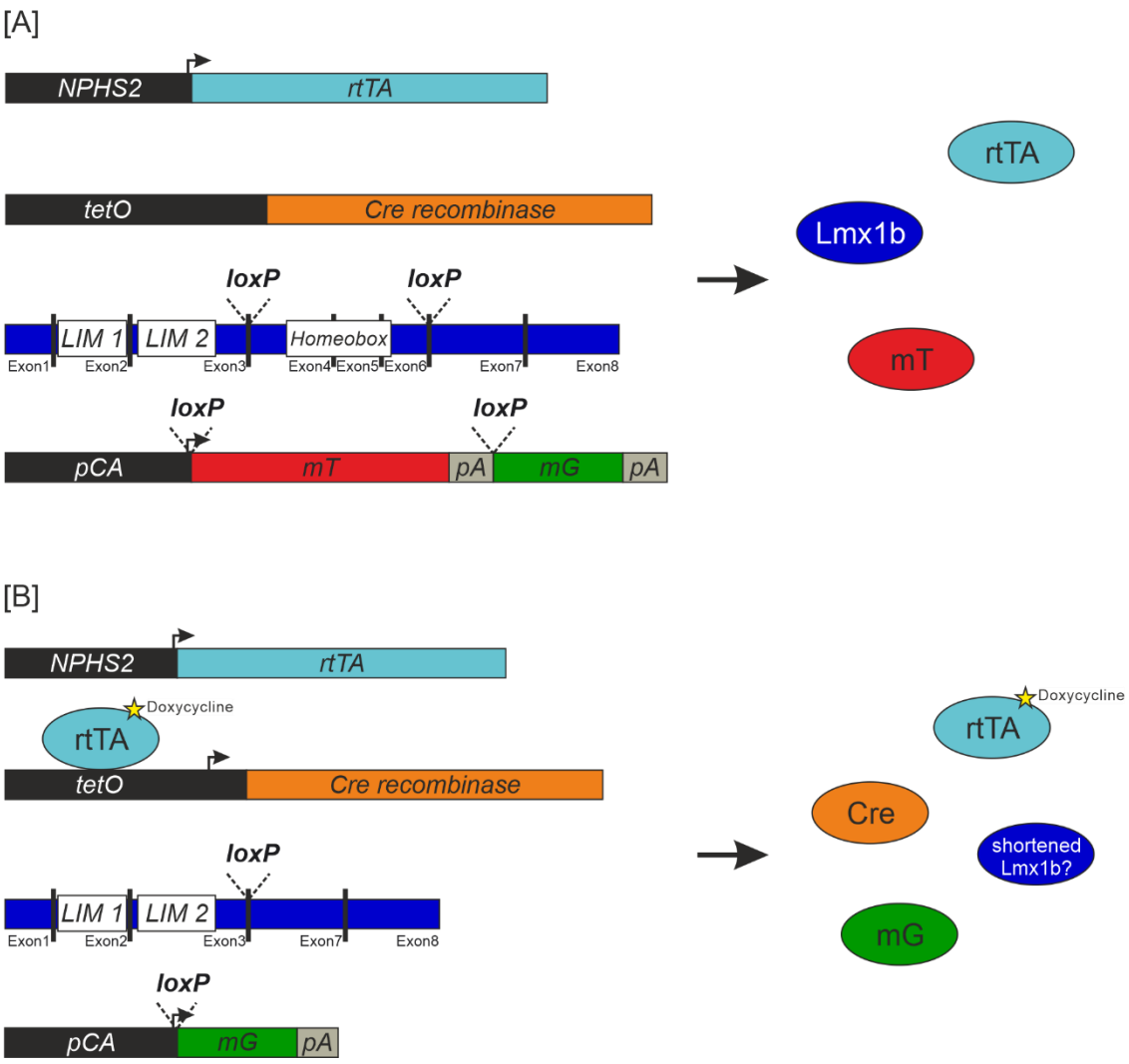

Figure 1.11 Model of the inducible, podocyte-specific Lmx1b knock-out system in absence [A] and presence [B] of doxycycline.
Red fluorescent protein mT (membrane-targeted tdTomato) is expressed in all cell types when the Cre recombinase is absent. Under control of the *NPHS2* promoter, rtTA is exclusively expressed in podocytes. During doxycycline treatment of those mice, rtTA is capable to bind and to activate the *tetO* promoter in order to induce the Cre expression. The Cre recombinase leads to a deletion of *Lmx1b* exons 4-6 and the *mT* sequence due to recombination at the respective loxP-sites of *Lmx1b* and the *mTmG* reporter construct. In the end, the expression of green fluorescent protein only occurs in podocytes synthesizing Cre and the in-frame deletion of the homeobox of *Lmx1b*. So far it is still not known, if there is a persisting expression of a shortened Lmx1b transcript containing the LIM domains. Model adapted from (Setzer 2020).

1.7 Aim of this study

The cause of the disease nail-patella syndrome has been identified more than 20 years ago. Nevertheless, the precise molecular mechanisms which are involved during the development of renal injury in some patients, remain still unknown. So far, the conventional *Lmx1b* knock-out mouse represented to be a convenient tool to investigate a range of structural and molecular alterations due to a Lmx1b defect. Disaccording to the human patients showing an autosomal dominant mode of inheritance, *Lmx1b* knock-out mice exclusively develop a nail-patella syndrome resembling phenotype when mice show a homozygous *Lmx1b* knock-out. By development of a constitutive podocyte-specific *Lmx1b* knock-out a further investigation of renal alterations could be obtained, but the discrepancy in the inheritance pattern is still unclarified. Therefore, it appears urgent to generate a more suitable animal model in order to better understand the pathogenesis of nail-patella syndrome in general and more specifically the role of the transcription factor LMX1B. The following four approaches were the aim of this thesis:

1. Characterization of the LIM domains of LMX1B: Do the LIM domains act in a cell-specific fashion?

The first goal of the present work was a detailed characterization of the LIM domain function of the transcription factor LMX1B using two different *Lmx1b* knock-in mouse lines. These transgenic mice (Burghardt *et al.*, unpublished) were generated carrying an amino acid substitution in one of the two LIM domains based on mutations of nail-patella syndrome patients, respectively. Within the present work, I systematically characterized all phenotypes of E18.5 *Lmx1b* knock-in mice in comparison to the conventional *Lmx1b* knock- out. The kidney histology was examined by hematoxylin / eosin staining and the number of filtration slits of neighboring podocytes was ascertained by electron micrographs. In addition, the skeletal development was analyzed by Alizarin red and Alcian blue staining, whereas the ossification of the skull was determined by µCT measurements.

2. What is the pathogenic mechanism of nail-patella syndrome?

On basis of the *Lmx1b* knock-in mice data, the possible pathogenic mechanisms of nail-patella syndrome should be discovered by protein turnover experiments as a second approach of this thesis. Since the group of (Cross *et al.* 2014) postulates a dominant-negative effect as pathogenic mechanism of nail-patella syndrome by the *Lmx1b Icst* mouse model, in addition, the protein turnover of the mutant protein LMX1B (V242D) was analyzed. This experiment should explain if we are dealing with a loss of function effect in *Lmx1b* knock-in mice compared to the dominant- negative effect in *Lmx1b Icst* mice. After the protein turnover experiments, the degradation pathway of the different LMX1B versions (WT, H54L, C95F, and V242D) should be identified in a second experiment by application of different inhibitors.

3. Do the amino acid substitutions H54L, C95F, and V242D evoke structural changes in LMX1B?

As the pathway of LMX1B protein degradation was discovered, in a next approach, the 3D structure of mutant proteins was analyzed. In cooperation with Gregor Madej from research group Ziegler, a homology modeling in addition to a calculation of the surface potential of LMX1B (WT), LMX1B (H54L), LMX1B (C95F), and LMX1B (V242D) was performed by use of the software UCSF chimera.

4. Does a stabilization of the mutant Lmx1b (H54L) and Lmx1b (C95F) protein rescue the phenotype *in vivo*?

Since the stabilization of the mutant LMX1B (H54L) as well as LMX1B (C95F) proteins in cell culture was successful, in a final approach, a potential candidate as a therapeutic target was initially tested on effects in proteinuria of compound heterozygous *Lmx1b* knock-out mouse lines, carrying point mutation coding for Lmx1b (C95F).

Overall goal of this thesis was to clarify the molecular mechanism of disease progression of nail-patella syndrome.

2. Material and Methods

2.1 Materials

2.1.1 Consumables and equipment

Equipment/Instrument	Source
Autoclave tape	VWR
Bottle top filter 0.22 µm	Sarstedt
Cannulas 21G x 1 ½ (0.8 x 40 mm)	Sterican
Cannulas 27G x ¾ (0.4 x 20 mm)	Sterican
Cell culture dish,100 mm	Sarstedt
Cell culture flask (25 cm^2, 75 cm^2)	Sarstedt
Cell scraper, 39 cm	Sarstedt
Chromatography paper	Whatman
Cover glasses, 24x60 mm	Roth
CryoPure tube, 1.8 ml	Sarstedt
Dispenser tips (0.5, 1.25, 2.5, 5.0, 12.5 ml)	VWR
Fabric thread terylene USP 2/0 DS-18, 24 x 50 cm	SERAG Wiessner
Filters, folded 90 mm	Schleicher & Schull
Glass coverslips, 12 mm	R. Langenbrinck
Glass Pasteur pipettes	VWR
Gloves, latex	Kimtech
Gloves, nitrile	Kimtech
Gravity flow column	Promega
Hypodermic needles	B. Braun
Line blades	Personna
Microtome blades A35 stainless steel	Feather
Microtome blades C35 carbon steel	Feather
Micro tubes (0.2, 0.5, 1.5, 2.0 ml)	Sarstedt
Microscope slides	Roth
Microscope slides, Superfrost® Plus	Thermo Fisher

Parafilm	Pechinery Plastic
Pipette filter tips	Sarstedt
Pipette tips	Sarstedt
Plates, 6-, 12-, 24-, 96-wells	Sarstedt
PVDF transfer membrane, pore size 0.45 µm	Merck; GE Healthcare
Q-tips	ISANA
Scalpel blades	Bayha
Serological pipettes (5, 10, 25 ml)	Sarstedt
Semi-micro cuvettes, 1.6 ml	Sarstedt
Snap cap vials	VWR
Super PAP Pen Liquid Blocker	Science Services
Syringes (1, 3 ml)	B. Braun
Task wipes, Kimtech	Kimberly-Clark Professional
Tube (12, 15, 50 ml)	Sarstedt

2.1.2 Chemicals and reagents

Chemicals and reagents	Source
Acetic acid	Merck
Acetone	Merck
Acrylamide, 30% / Bisacrylamide, 0.8% solution	Serva
Agarose, NEEO quality	Roth
Alcian Blue 8GX	Chroma Gesellschaft Schmidt & Co.
Alizarin Red	Chroma Gesellschaft Schmidt & Co.
Amido black 10B	Merck
Ampicillin sodium salt	Roth
APS (Ammonium persulfate)	Fluka
Bafilomycin A1 (Baf-A1), H^+-ATPase inhibitor	Selleck Chemicals
Bortezomib (PS-341), 20S proteasome inhibitor	Selleck Chemicals

Bromphenol blue	Serva
BSA (Bovine serum albumin), fraction V	Sigma-Aldrich
Calcium chloride	Roth
cOmplete™, EDTA-free Protease Inhibitor Cocktail	Roche
Creatinine	Merck
DePeX	Serva
Dipotassium hydrogen phosphate	Merck
di-Sodium hydrogen phosphate	Merck
DMEM: Dulbecco´s modified Eagle medium; high glucose	PAA
DMP-30	Roth
DMSO (Dimethylsulfoxide)	Sigma-Aldrich
dNTPs (Deoxynucleotide triphosphates)	Fermentas
Doxycycline hyclate	AppliChem
EDTA, disodium salt (Ethylendiaminetetraacetic acid)	Roth
Eosin	Agar scientific
Epon embedding medium	Sigma-Aldrich
Epon hardener DDSA	Sigma-Aldrich
Epon hardener MNA	Sigma-Aldrich
Ethanol	Sigma-Aldrich
Ethidium bromide	Sigma-Aldrich
FCS (Fetal calf serum)	PAN Biotech
Ficoll™ 400	Serva
Geneticin (G418)	Invitrogen
Glucose	Merck
Glutaraldehyde, 25 %	Serva
Glycerol	Roth
Glycine	Sigma-Aldrich
Hematoxylin, Gill No. 3	Sigma-Aldrich
HEPES (4-(2-hydroxylethyl)-1-piperazineethanesulfonic acid	Roth
Histoacryl®	B. Braun
Hoechst stain # 33258	Hoechst AG
Hydrochloric acid, 1 M	Merck
Hydrochloric acid, 32%	Merck

Hygromycin B	PAN
Immersol™ 518 F	Zeiss
Isopropanol	Merck
Lead citrate, 3% (Ultrostain 2)	Leica
MG-132, proteasome inhibitor	Selleck Chemicals
Magnesium chloride	Merck
Methanol	Merck
Mowiol® 40-88	Sigma-Aldrich
Narcoren	Merial
Nonidet-P40	AppliChem
Osmiumtetroxide 25 %	Plano
Paraplast Plus® (Paraffin)	Leica
Periodic acid	Sigma-Aldrich
PFA (Paraformaldeyhde)	Merck
Picric acid (2,4,6-trinitrophenol TNP)	Sigma-Aldrich
Poly-L-ornithine	Sigma-Aldrich
Potassium chloride	Merck
Potassium dihydrogen phosphate	Merck
Protein G PLUS Agarose	Santa Cruz
Puromycin	PAA
Roti-Phenol/Chloroform/Isoamylalcohol, 25:24:1 P/C/I	Roth
Roti-Quant	Roth
RT-PCR Grade Water ready for RT-PCR	Thermo Fisher
SDS (Sodium dodecyl sulfate)	Serva
Skim milk powder	Sucofin
Sodium acetate	Roth
Sodium cacodylate trihydrate	Fluka
Sodium chloride	Merck
Sodium dihydrogen phosphate	Roth
Sodium hydroxide solution, 1 M	Fluka
Sucrose	Merck
SuperSignal West Pico	Thermo Fisher
TEMED (Tetramethylethylenediamine)	Roth
Tissue-Tek®	Sakura Finetek

Trichloroacetic acid	Riedel-deHaen
Tris base (Tris(hydroxymethyl)aminomethane)	Sigma-Aldrich
Trisodium citrate dihydrate	Merck
Triton-X-100	Roth
Tween 20	Roth
Uranyl acetate dihydrate	Merck
Urea	Merck
WesternBright ECL	advansta
Xylene cyanol FF	Serva
Xylol	Merck
β-mercaptoethanol	Merck

2.1.3 Buffers, solutions, and media

Commercial buffers and media

Buffer/Medium	Source	Cat. No.
10x Pfu Buffer	Promega	M776A
10x Thermopol® Buffer	NEB	B9004S
10x CutSmart® Buffer	NEB	B7204S
10x NEBuffer 3.1	NEB	B7203S
5x Phusion® Reaction Buffer	NEB	B0518S
DMEM: Dulbecco´s modified Eagle Medium; high Glucose	PAA	6429

Media/solutions for bacteria work

Buffer/Solution	Ingredients		
LB	10 g/L	Bacto tryptone	Autoclaved
	5 g/L	Bacto yeast	
	10 g/L	NaCl	
Ampicillin stock solution	50 g/L	Ampicillin sodium salt	Sterile filtrated

Buffers/solutions for SDS-PAGE

Buffer/Solution	Ingredients		
4x Stacking gel buffer	0.5 M	Tris base	pH 6.8, HCl
	4 g/L	SDS	
4x Separating gel buffer	1.5 M	Tris base	pH 8.8, HCl
	4 g/L	SDS	
5x SDS sample buffer	625 mM	Tris base	pH 6.7, HCl
	125 g/L	SDS	
	12.5%	β-mercaptoethanol	
	0.5 g/L	Bromphenol blue	
	50%	Glycerol	
10x SDS running buffer	0.25 M	Tris base	
	1.9 M	Glycine	
	10 g/L	SDS	
Amido black staining solution	1.5 mM	Amido black 10 B	
	50%	Methanol	
	10%	Acetic acid	

Buffers for western blotting

Buffer/Solution	Ingredients		
Transfer buffer	50 mM	Tris base	
	384 mM	Glycine	
	0.1 g/L	SDS	
	20%	Methanol	
10x TBS	0.25 M	Tris base	pH 7.4, HCl
	1.4 M	NaCl	autoclaved
	26.8 mM	KCl	
TBS-T	0.1%	Tween 20	
		in 1x TBS	

Solutions for mouse work

Buffer/Solution	Ingredients	
Induction solution	2 g/L	Doxycycline
	50 g/L	Sucrose
Physiological saline solution	9 g/L	NaCl
Narcoren working solution	1:50	dilution of Narcoren in physiological saline solution

Buffers/solutions for epon embedding

Buffer/Solution	Ingredients	
Epon	4.6 g	Epon embedding medium
	2.85 g	Hardener DDSA
	2.51 g	Hardener MNA
	0.15 g	Accelerator DMP-30

Buffers for DNA isolation and genotyping

Buffer/Solution	Ingredients		
Tail buffer	100 mM	Tris base	pH 8.0, HCl
	200 mM	NaCl	autoclaved
	5 mM	$Na_2EDTA \times 2\ H_2O$	
	2 g/L	SDS	
TE buffer	10 mM	Tris base	pH 8.0, HCl
	1 mM	$Na_2EDTA \times 2\ H_2O$	autoclaved
50x TAE buffer	2 M	Tris base	pH 8.0, HAc
	0.1 M	$Na_2EDTA \times 2\ H_2O$	
5x DNA loading buffer	50 mM	$Na_2EDTA \times 2\ H_2O$	pH 8.0
	1.25 g/L	Bromphenol blue	
		Or xylene cyanol FF	
	1.5 g/L	Ficoll type 400	
	5 g/L	SDS	

Buffers for tissue and cell fixation

Buffer/Solution	Ingredients		
4% PFA	40 g/L	PFA solved in water with 20 drops of 1 M NaOH added under heating to max. 60 °C; add 10x PBS following complete dissolving	pH 7.4
2% Glutaraldehyde	1:12.5	dilution of Glutaraldehyde 25% in Caco buffer	pH 7.4
Caco buffer	0.1 M	Sodium cacodylate trihydrate	pH 7.4
Sucrose buffer	180 g/L	Sucrose in 1x PBS	pH 7.4

Buffers for immunofluorescence staining

Buffer/Solution	Ingredients		
Retrieval buffer	10 mM	$Na_3C_3H_5(COO)_3$ x 2 H_2O	pH 6.0
Histoblock buffer	20 g/L 0.1%	BSA Triton-X-100 in 1x PBS	pH 7.4
3% BSA buffer	30 g/L	BSA in 1x PBS	pH 7.4
Permeabilization buffer cells	0.2%	Triton-X-100 in 1x PBS	pH 7.4
Permeabilization buffer, tissue	0.3%	Triton-X-100 in 1x PBS	pH 7.4
Hoechst staining buffer		Hoechst AG # 33258 1:5 000 in 1x PBS pH 7.4	
Mounting buffer		Mowiol	

Buffers/solutions for skeletal staining

Buffer/Solution	Ingredients		
Fixation solution	95%	Ethanol	4 °C; 1-2 days
	100%	Acetone	RT; overnight
Cartilage stain	15 mg	Alcian blue 8GX	RT; overnight
	80 mL	Ethanol (95%)	
	20 mL	Acetic acid (100%)	
Wash solution	95%	Ethanol	RT; overnight
Clearing	1%	Potassium hydroxide	RT; 2-3 h
Bone stain	50 mg	Alizarin red	
	1%	Potassium hydroxide	
Storage	100%	Glycerol	

Buffers and media for work with cells

Buffer/Solution	Ingredients		
10x PBS	1.27 M	NaCl	pH 7.4
	27 mM	KCl	
	14.7 M	KH_2PO_4	
	80.9	Na_2HPO_4 x 2 H_2O	
Growth medium:	90%	DMEM	
HtTA-1/myc-LMX1B (WT)	10%	FCS	
	200 µg/mL	Geneticin (G418)	
	300 µg/mL	Hygromycin B	
	100 ng/mL	Doxycycline	

Growth medium:	90%	DMEM
HtTA-1/myc-LMX1B (H54L)	10%	FCS
HtTA-1/myc-LMX1B (C95F)	200 µg/mL	Geneticin (G418)
HtTA-1/myc-LMX1B (V242D)	1 µg/mL	Puromycin
	100 ng/mL	Doxycycline

Buffer for cell lysis

Buffer/Solution	Ingredients		
Urea lysis buffer	6 M	Urea	pH 7.4
	1%	Triton-X-100	
		in 1x PBS	

2.1.4 Enzymes, kits, and markers

Enzymes

Enzyme	Source	Cat. No.
BspEI	NEB	R0540L
RNase-Free DNase Set	Qiagen	79254
DpnI	NEB	R0176S
Proteinase K	Roth	7528.2
Phusion® HF DNA Polymerase	NEB	M0530S
Pfu DNA Polymerase	Promega	M774A
Taq DNA Polymerase	NEB	M0267L
XhoI	NEB	R0146S

Kits

Kit	Source	Cat. No.
Wizard® *Plus* Midipreps DNA Purification System	Promega	A7640
RNeasy Mini Kit	Qiagen	74104
iScript™ cDNA Synthesis Kit	Biorad	1708891
SensiFAST™ SYBR® No-ROX Kit	Bioline	BIO-98020

Markers

Marker	Source	Cat. No.
1 kb Plus DNA ladder	NEB	N3200S
PageRuler prestained protein ladder	Thermo Fisher	26616
TriDye™ Ultra Low Range DNA ladder	NEB	N0358S

2.1.5 Antibodies and peptides

Primary antibodies and peptides

Title	Immunogen	Species	Dilution	Source
Anti-GAPDH	GAPDH, h, m, r	Rabbit polyclonal	1:7 500 (WB)	Sigma-Aldrich G9545
BMO8	Lmx1b, h, m	Rabbit Polyclonal	1:2 000 (WB) 1:500 (IF-P)	Own Lab

Secondary antibodies

Immunogen	Conjugate	Species	Dilution	Source
Goat IgG	Alexa 568	Donkey	1:600 (IF)	Invitrogen A-11057
Rabbit IgG	HRP	Goat	1:15 000 (WB)	Sigma-Aldrich A-0545

2.1.6 Oligonucleotides

Oligonucleotides were purchased from the company Metabion, Martinsried.

Genotyping

Gene	Primer	Sequence	Amplicon
Cre	forward	TGGACATGTTCAGGGATCGC	613 bp
	reverse	TCAGCTACACCAGAGACGGA	
Lmx1b, C95F	forward	GTTTGGCTATGGGGTTGAGG	428 bp (WT)
	reverse	CATAGTCACCCTTGCACAGC	526 bp (TG)
Lmx1b, H54L	forward	AAAGGAGCGTGCTGTCTAGG	493 bp (WT)
	reverse	GCTGGAAGGAGATGATTCG	585 bp (TG)
Lmx1b,	forward	GATAGGGCATTCAACCAGGACGAGCAAAGA	272 bp (WT)
knock-out	reverse (WT)	AAACAGAAGCCACAGAGAGCCAAGGAGAAG	397 bp (TG)
	reverse (TG)	GGTGCCACTCCCACTGTCCTTTCCTAATAA	
Lmx1b, flox	forward	AGGCTCCATCCATTCTTCTC	220 bp (WT)
	reverse	CCACAATAAGCAAGAGGCAC	330 bp (TG)
mTmG	forward	CTCTGCTGCCTCCTGGCTTCT	330 bp (WT)
	reverse (WT)	TCAATGGGCGGGGGTCGTT	250 bp (TG)
	reverse (TG)	CGAGGCGGATCACAAGCAATA	
rtTA	forward	AAACGGCGCTCTGGAATTAC	418 bp
	reverse	CTGTTCCTCCAATACGCAGC	

qPCR and PCR

Gene	Primer	Sequence	Amplicon	
Lmx1b	forward	AAAGAGCAAAGATGAAGAAGAAGCTG	93 bp	qPCR
	reverse	CGGCTTGACAGAACCTCTTG		
Lmx1b transcript	forward	ATCAAGATGGAGGAGCACGC	959 bp	PCR
	reverse	GAGTCGTTCCCTGGCATTTG		
S9	forward	GCAAGATGAAGCTGGATTAC	340 bp	qPCR
	reverse	GGGATGTTCACCACCTG		
LMX1B (H54L)	forward	GTTTGGCTATGGGGTTGAGG		site directed mutagenesis PCR
	reverse	CATAGTCACCCTTGCACAGC		
LMX1B (V242D)	forward	AGTGTGCGCGTGGTCCAGGACTGGTT TCAGAACCAAA		site directed mutagenesis PCR
	reverse	TCACACGCGCACCAGGTCCTGACCAA AGTCTTGGTTT		

2.1.7 Plasmids and cell lines

Plasmids

Plasmid	Bacterial strain	Resistance	Source
pUHD10-3/myc-LMX1B (WT)	DH5α	Amp	Own lab
pUHD10-3/myc-LMX1B (H54L)	DH5α	Amp	Own lab
pUHD10-3/myc-LMX1B (V242D)	DH5α	Amp	Own lab
pWE3	DH5α	Amp	ATCC

Cell lines

Cell line/ bacterial strain	Description	Source
HtTA-1/myc-LMX1B (WT), clone 34	HeLa cells, inducible LMX1B protein expression via the Tet-off-system	C. Rohr Universitäts-klinikum Innere Medizin III, Heidelberg
HtTA-1/myc-LMX1B (C95F), clone 351	HeLa cells, inducible LMX1B C95F mutant protein expression via the Tet-off-system	Own lab
HtTA-1/myc-LMX1B (H54L), clone 141	HeLa cells, inducible LMX1B H54L mutant protein expression via the Tet-off-system	Own lab
HtTA-1/myc-LMX1B (V242D), clone 90	HeLa cells, inducible LMX1B V242D mutant protein expression via the Tet-off-system	Own lab
DH5α	*Escherichia coli* strain Competent strain used for mammalian plasmid reproduction	DSMZ

2.1.8 Equipment and instruments

Equipment / Instrument	Source
Absorbance microplate reader ‘Sunrise’	TECAN
Agarose gel electrophoresis chamber ‘Horizon 58’	Gibco
Agarose gel electrophoresis chamber ‘Owl™ EasyCast™ B2’	Thermo Fisher
Autoclave ‘2540 ML’	Tuttnauer
Autoclave ‘5050 ELV’	Tuttnauer
Blotting chamber ‘Tank Blot SE 600’	Hoefer
Bunsen burner	Usbeck
Centrifuge ‘Avanti® J-26 XP’ with rotor Ja-10	Beckman Coulter
Centrifuge ‘Heraeus Pico 17’	Thermo Fisher
Centrifuge ‘Hitachi himac CT15RE’ with rotor T15A61-1041	VWR
Centrifuge ‘Multifuge 3 L-R’ with rotor 75006445	Heraeus
Centrifuge ‘Sigma-Aldrich 3K20’ with rotor 12158	Sigma
Chemiluminescence system ‘Fusion-FX7’	Vilber Lourmat
CO_2 incubator ‘CB210’	Binder
Cryostat ‘CM3050s’	Leica
Digital slide scanner ‘NanoZoomer-SQ’	Hamamatsu
Freezers -20 °C	Privileg
Freezers -80 °C ‘Herafreeze™’	Thermo Fisher
Gel documentation system ‘GelDoc™ XR+’	Bio-Rad
Gel electrophoresis cell ‘Mini Protean 3’	Bio-Rad
Glassware (beakers, bottles, flasks)	Schott; VWR
Heating plate with a magnetic stirrer ‘MR 2002’ and ‘MR 3001’	Heidolph
Hybridization oven ‘HB-1000’	UVP
Hybridization oven ‘OV3’	Biometra
Ice machine	Ziegra
Incubator ‘Kelvitron t’	Thermo Fisher
Incubator ‘Multitron standard’	Infors
Inverted microscope ‘Eclipse TS100’	Nikon
Laboratory pH Meter ‘CG 842’	Schott

Laminar flow bench ‘Lamin Air HA 2448 GS’	Heraeus
Liquid nitrogen container ‘Arpege TP 170’	Air Liquide Medical
µCT ‘phoenix v|tome|xs 240/180 research edition’	GE Sensing & Inspection Technologies GmbH
Microtome ‘RM2255’	Leica
Microwave ‘8016 G’	Privileg
Multi-dispenser ‘HandyStep® electronic’	BRAND
NanoDrop 2000	Thermo Fisher
Neubauer counting chamber (depth 0.1 mm)	Marienfeld
Paraffin embedding module ‘EG1150 H’	Leica
pH electrode ‘SenTix 60’	WTW
Pipettes	Gilson
Pipettor ‘IPS Pipetboy acu’	Integra Bioscience
Power supply ‘PS 608’	Life technologies
Power supply ‘Standard Power Pack P25’	Biometra
Refrigerators	SEG, Privileg
Rocking platform shaker ‘Duomax 1030’	Heidolph
Rocking platform shaker ‘Polymax 2040’	Heidolph
Spectrophotometer ‘NanoDrop™ 2000’	Thermo Fisher
Tissue processor ‘TP-1020’	Leica
Thermal cycler ‘MyCyclerTM’	Bio-Rad
Thermal cycler ‘T100’	Bio-Rad
Thermal cycler ‘LightCycler® 480 Instrument’	Roche
Transmission electron microscope ‘EM Zeiss 902’	Zeiss
Ultrapure water unit ‘Seralpur PRO 90 CN’	Seral
Vacuum gas pump	VWR
Vertical gel electrophoresis cell ‘Mini Protean Tetra cell’	Bio-Rad
Weighing scale ‘BL 1500 S’	Sartorius
Weighing scale ‘Kern 770’	KERN & Sohn

Epifluorescence microscope

	Title	Source
Microscope	Axiovert 200M	Zeiss
Light source	LEJ (HXP-120)	Visitron Systems
Objectives	Ultrafluar, 20x/0.6	
Camera	CoolSnap ES	Visitron Systems

Epifluorescence microscope with motorized x,y-stage

	Title	Source
Microscope	Observer.Z1	Zeiss
Light source	Colibri.2	Zeiss
Objectives	EC Plan-Neofluar 20x	Zeiss
Camera	Axiocam MR R3	Zeiss

2.1.9 Software and tools

Software	Version	Purpose	Company
Bio1D	15.07	WB quantification	Vilber Lourmat
Citavi	6	Citation and references	Swiss Academic Software
Coot	0.9	Rotamer generation	coot
Excel	Office 2019	Data processing	Microsoft
Fiji (ImageJ)	1.51s	Image processing	National Institutes of Health
FileMaker Pro	6	Database	FileMaker, Inc.
Fusion	15.18	WB imaging	Vilber Lourmat
ImageLab	5.2	Gel documentation	Bio-Rad

Magellan™	7.2	Photometric measurement	TECAN
MODELER	9v22	Homology Modeling	MODELER
myVGL	3.3.6	µCT Image processing	Volume Graphics GmbH
NanoDrop 2000/2000c Operating Software	1.6	Photometric measurement; DNA/RNA quantification	Thermo Fisher
NanoZoomer Digital Pathology.view	2	Image visualization	Hamamatsu
Origin 2020Sr1	9.7.0.188	Data processing, diagrams	OriginLab
SnapGene Viewer	4.2.5	Gene/plasmid handling	GSL Biotech, LLC
UCSF-Chimera	1.15	3D imaging, daily build 42153	Chimera
VisiView	2.1.4	Image recording	Visitron Systems
Word	Office 2019		Microsoft
Z-DOPE score	9v22	Statistical potential	MODELER
ZEN 2011 SP3 (black edition)	8.1	Image recording	Zeiss MicroImaging

Internet databases and tools

Title	Address
BLAST	https://blast.ncbi.nlm.nih.gov/Blast.cgi
ensemble	https://www.ensembl.org/index.html
HGMD	http://www.hgmd.cf.ac.uk/ac/index.php
Pubmed	https://www.ncbi.nlm.nih.gov/pubmed/
UCSC Genome Browser	https://genome.ucsc.edu/
Primer3 Design	https://primer3.ut.ee/

2.2 Working with bacteria

2.2.1 Cultivation of *E. coli*

E. coli were cultivated under sterile conditions. All media and glass vessels were previously autoclaved before use. A long-term storage of bacteria was obtained by freezing cells in LB medium with glycerol (6:1) at -80 °C. Inoculation of cultures was achieved near the flame. For plasmid isolation 5 mL LB medium cultures supplemented with 0.1 mg/mL ampicillin were directly inoculated with a small quantity of frozen cells or transformed and grown overnight at 37 °C under constant shaking (250 rpm). On the following day, 100 µL of grown cell culture was transferred into 100 mL of LB medium supplemented with 0.5 mg/mL ampicillin and grown at 37 °C under constant agitation for approximately 16 h.

2.2.2 Transformation of *E. coli*

Between 200 and 600 ng/µL of plasmid DNA of sequenced plasmid was added to 50 µL DH5α competent partially thawed cells for transformation and incubated on ice for 30 minutes. In order to facilitate the plasmid uptake by the bacteria, they were exposed to a heat shock at 42 °C in a water bath for precisely 45 seconds. Subsequently, bacteria were stored on ice for 2 to 5 minutes and then 500 µL of LB medium without antibiotics was supplemented followed by an incubation for 1 hour at 37 °C for regeneration. Then 50 µL, 150 µL, and 250 µL of bacterial suspension were plated on LB agar containing 100 µg/mL of Ampicillin. Plates were then incubated overnight at 37 °C followed by inoculation of 5 mL LB culture medium on the next day.

2.3 Working with DNA

2.3.1 Site-directed mutagenesis PCR of pUHD10-3/LMX1B (WT)

For studies of LMX1B counterpart mutants LMX1B (H54L) and LMX1B (V242D), first plasmids had to be generated by site-directed mutagenesis PCR of the plasmid pUHD10-3/myc-LMX1B (WT). This PCR reaction was performed using the *Pfu* polymerase from Fermentas, oligonucleotides were used according to Table 2.1 and 2.1.6. First 37.5 µL of Mix 1 were pipetted into a PCR reaction tube and placed into the thermal cycler followed by starting the heat step at 99 °C for 5 minutes. Then PCR run was briefly paused in order to add 12.5 µL of Mix 2 into tubes and thereafter the run proceeded. PCR program was conducted as described in Table 2.2.

Table 2.1: Mastermix of mutagenesis PCR.

Ingredients	Mix 1	Mix 2
10x PCR buffer	3.75 µL	2.5 µL
Primer forward (1 µg/µL)	0.88 µL	-
Primer reverse (1 µg/µL)	0.89 µL	-
dNTPs (10 mM)	-	5 µL
Template (100 ng/µL)	2 µL	-
Pfu (3 U/µL)	-	0.83 µL
H_2O	Ad 37.5 µL	Ad 12.5 µL

Table 2.2: Protocol for mutagenesis PCR.

Step	T	t		
Melting DNA	99 °C	5 min		Mix 1
Pause, add Mix 2				
Melting amplicon	94 °C	30 sec		Mix 1 + 2
Annealing	58 °C ± 8°C	1 min	35 cycles	
Elongation	72 °C	10 min		
Final elongation	67 °C	5 min		
Hold	4 °C	∞		

2.3.2 Phenol/Ethanol precipitate of plasmid DNA

To separate amplified plasmid DNA from the remaining PCR components after PCR reaction, plasmid DNA was phenolized and ethanol-precipitated using the PCI (Roti-Phenol/Chloroform/Isoamylalcohol, 25:24:1, Roth) mixture. 50 µL of the PCI mixture were added to 50 µL of PCR product and mixed by vortexing for 30 seconds. Thereafter, the samples were centrifuged at 14 000 rpm for 20 minutes at room temperature. Phase separation occurred and DNA fraction in the aequous phase was collected and transferred into a fresh 1.5 reaction tube. In the following, DNA was precipitated by adding 5 µL of 3 M sodium acetate pH 5.2 and 150 µL of 100% ethanol. Samples were mixed by inverting and afterwards centrifuged at 14 000 rpm for 1 hour at 4 °C. DNA-pellet was resuspended in 600 µL of 70% ethanol and again centrifuged at 14 000 rpm for 10 minutes at 4°C. Finally, DNA- pellets were dried at 37 °C and solved in 50 µL of nuclease-free H_2O.

2.3.3 *DpnI* digestion

Common lab *E. coli* K12 strains, such as DH5α used for this study, contain methylases that recognize and methylate different stretches of DNA. For useful removal of the cell-derived plasmid template from the mutagenized PCR product, samples were digested by *DpnI* (Mierzejewska *et al.* 2014). This enzyme was able to recognize and cut methylated DNA, which is produced during plasmid synthesis by the *dam+ E. coli* strain DH5α. When PCR products were digested by *DpnI*, only the non-mutated and methylated template was abolished leaving the amount of mutated plasmid for further analysis. 40 µL of respective samples were digested by 1.0 µL of *DpnI* (10 U per PCR reaction) at 37 °C for 1 hour followed by a heat inactivation step of *DpnI* at 80 °C for 20 minutes. Thereafter, *E. coli* DH5α cells were exclusively transformed with mutagenized PCR products followed by isolation of mutated plasmid DNA.

2.3.4 Plasmid DNA isolation

Preparation of plasmid DNA was achieved with the Promega Wizard® *Plus* Midipreps DNA Purification System according to manufacturer´s instructions. In a first step, 600 µL of the overnight grown cell culture were mixed with 100 µL of glycerol (100%) for long-term storage of bacteria glycerol culture at -80 °C. Subsequently, 100 mL overnight cultures were centrifuged at 4 000 g for 20 min at 4 °C. The cell pellet was then resuspended in 3 mL of Cell Resuspension Solution by pipetting up and down. Afterwards, first 3 mL of Cell Lysis Solution were added, mixed by inverting and second, 3 mL of Neutralization Solution were added and inverted to mix. Next, samples were centrifuged at 14 000 rpm for 30 min at 4 °C and subsequently, the supernatant was filtered by use of Kimtech Science™ Precision Wipes, then mixed with 10 mL of resin, and transferred into a Midicolumn. The solution was drawn through the Midicolumn by applying vacuum. The bound DNA was twice washed with 15 mL Column Wash Solution containing ethanol. After the second wash, the vacuum was continued for 30 seconds after liquid has passed through the Midicolumn. After drying, the Midicolumn was separated from the reservoir and placed in a 1.5 mL microcentrifuge tube followed by a centrifugation step at 10 000 g for 2 minutes. For elution, the Midicolumn was placed on a new 1.5 mL tube and the plasmid DNA was incubated for 1 min with 300 µL of 70 °C preheated sterile H_2O_{bidest}. Finally, the DNA was eluted by centrifugation at 10 000 rpm for 20 seconds. The DNA concentration was measured with the NanoDrop spectrophotometer.

2.3.5 Sequencing

Sequencing of plasmid DNA or PCR products was carried out by the company Microsynth Seqlab requiring 100 ng/µL for plasmid DNA and 30 ng/µL for PCR products in a volume of 12 µL. Two reaction tubes for one sample were prepared containing 3 µL either of the forward Primer (20 µM) or the reverse Primer (20 µM) as listed in 2.1.6. Sequencing data was further analyzed using the SnapGene Viewer.

2.4 Working with RNA

2.4.1 RNA Isolation

For purification of total RNA from E18.5 murine kidneys or from HeLa cells of a confluent P10 dish, the appropriate protocol of the RNeasy Mini Kit from Qiagen was conducted according to the manufacturer´s instructions. Briefly, flash-frozen kidneys in liquid nitrogen or cells were stored at -80 °C until RNA isolation procedure. Prior to the isolation, 10 µL of β- Mercaptoethanol were added to 1 mL of buffer RLT. The buffer RPE was supplied as a concentrate and before using it for the first time, 4 volumes of 100% ethanol were added. Furthermore, an on-column *DNase* digestion was performed using the RNAse-free *DNase* set from Qiagen. The *DNase* I stock solution was prepared by dissolving the lyophilized DNase I, 1500 Kunitz units, in 550 µL of the provided RNAse-free water. The DNase I stock solution was aliquoted and stored at -20 °C for up to 9 months.

Kidney as well as cell samples were removed from storage followed by an immediate disruption in 600 µL of buffer RLT. Lysates were well homogenized by careful pipetting, in case of the kidney samples, a 21 G canula and a 1 mL syringe were used for homogenization and shearing the tissue material. Thereafter, 1 volume of 70% ethanol, diluted in DEPC water, was added to the cleared lysates, and immediately mixed by pipetting. In the following, 700 µL of the samples were transferred to a RNeasy spin column placed in a 2 mL collection tube and centrifuged for 15 seconds at 13 000 x g. The flow-through was discarded and the rest of the samples were loaded on the column by centrifugation for 15 seconds at 13 000 x g. Subsequently, 350 µL of buffer RW1 were added to the RNeasy spin column, centrifuged for 15 sec at 8 000 x g to wash the column membrane and the flow-through was discarded. In a next step, the on-column DNase digestion was conducted by adding 70 µL of buffer RDD to the 10 µL DNase I aliquot and pipetting the 80 µL of *DNase* I incubation mix directly onto the column membrane. Digestion was carried out for 1 hour at 28 °C in a hybridization oven. Afterwards, 350 µL of Buffer RW1 were added to the column, centrifuged for 15 seconds at 8 000 x g followed by a column wash step by adding 500 µL of buffer RPE. Columns were centrifuged for 15 seconds at 8 000 x g, flow-through was discarded and the RPE

wash step was repeated. Centrifugation was carried out for 2 minutes at 8 000 x g and finally, columns were placed in a new 1.5 mL collection tube. In case of E18.5 kidney samples, total RNA was eluted in 30 µL of RNAse-free water and centrifuged for 1 minute at 10 000 x g. This step was repeated by pipetting 15 µL of the eluate back onto the column to enhance the expected RNA yields. For samples from cells, total RNA was eluted in 100 µL of RNAse-free water and centrifuged for 1 minute at 13 000 x g. The concentration of RNA samples was determined using the NanoDrop spectrophotometer. For quality control of the 18S and 28S rRNA band intensities from cells, 200 ng RNA were applied on a 1% agarose gel, as described in 2.6.3.

2.4.2 cDNA synthesis

The isolated RNA was transcribed into cDNA using the iScript™ cDNA Synthesis Kit from Bio- Rad. For this purpose, a 20 µL synthesis reaction was applied according to Table 2.3. As a last component 1 µL of the Reverse Transcriptase and in case of the non-Reverse Transcriptase control (non-RT control) 1 µL of RNAse- free water were added. After a quick mix, the samples were placed into a thermal cycler and the cDNA synthesis program was started (Table 2.4).

Table 2.3: Reaction setup for cDNA synthesis.

Ingredients	Volumes
5x iScript Reaction Mix (Oligo(dT)-Primer and random hexamers)	4 µL
iScript Reverse Transcriptase	1 µL
Nuclease-free water	Variable
RNA template (1 µg)	Variable
Total volume	20 µL

Table 2.4: Reaction protocol of cDNA synthesis.

Step	T	t
Priming	25 °C	5 minutes
Reverse transcription	46 °C	20 minutes
RT inactivation	95 °C	1 minute
Optional step	4 °C	hold

2.4.3 Quantitative real-time PCR

This method was applied to measure the amount of transcribed mRNA levels of distinct genes within the cell. The calculated ratio of a reference gene, such as ribosomal protein S9, and a target gene determines the amount of expression level at that moment. For these analyses, initially RNA was isolated and transcribed into cDNA according to previous chapters 2.4.1 and 2.4.2. The cDNA served as a DNA template in the following qPCR analysis containing a fluorescent dye, referred to SYBR Green. This dye emits fluorescence when it is bound to double-stranded DNA, but not in an unbound state (Bustin 2000). After each PCR cycle, the amplificons were doubled accompanied by the fluorescence signal. After exceeding the background fluorescence, the crossing point (Cp-value) is manifested. The fluorescent threshold values are selected regarding the beginning of the exponential phase and therefore correlate linearly with the relative mRNA copy numbers (Gibson *et al.* 1996). The ratio of the expression rates of the target gene and the reference gene revealed the relative quantification of target gene expression, also described as a normalization of the mRNA expression results (Heid *et al.* 1996). Data in this thesis were normalized to murine ribosomal protein S9 and expressed as relative mRNA levels.

Assay performance

Due to the high sensitivity of this method, the handling process was performed with a high accuracy. To achieve a consistent approach and to avoid inaccuracies because of small volumes, large approaches were mixed and distributed to single samples. The method was carried out using white 96-well plates appropriate for the LightCycler® 480 Instrument from Roche. Every sample consisted of triplicates to enhance specificity of the results. To exclude possible DNA contaminations and primer dimer formation, non-RT controls of each sample and one water control were additionally analyzed within each qPCR run. All samples were pipetted on one plate and run of one experiment was repeated three times. The SensiFAST™ SYBR® No-ROX kit from Bioline was used for qPCR reactions. The kit was provided as a 2x

mastermix comprising all components that were necessary for the qPCR reaction, including an antibody-mediated hot-start DNA polymerase, the SYBR® Green I dye, dNTPs, stabilizers, and enhancers. The kit consisted of a ready-to-use premix, only respective primers and templates needed to be added. cDNA was diluted 1:16 prior to qPCR analysis and for each qPCR run, a serial dilution of respective reference and target genes was prepared to determine the standard curve. For a single qPCR reaction reagents and volumes were applied according to Table *2.5* and primers were applied as listed in chapter 2.1.6. Immediately after pipetting reactions on ice, the 96 well-plate was covered with a sealing foil and centrifuged at 2,750 rpm for 2 minutes at room temperature. Subsequently, the 96-well plate was placed into the LightCycler® 480 Instrument from Roche and the qPCR program was started (Table 2.6).

Table 2.5: Composition of a single qPCR reaction.

Ingredients	Volumes
2x SensiFAST™ SYBR® No-Rox mix	10 µL
Primermix (forward and reverse; 10 µM, respectively)	5 µL
H_2O	3 µL
cDNA	2 µL
Ad	20 µL

Table 2.6: qPCR protocol for E18.5 analysis.

Step	T	t	
Melting DNA	95 °C	7 minutes	
Melting amplicon	95 °C	20 seconds	55 cycles
Annealing	60 °C	10 seconds	
Elongation	72 °C	20 seconds	
Melting curve			
Hold	40 °C	hold	

Analyses

Signals of non-RT and water samples were monitored if there were any DNA contaminations or primer dimer formation. In the case of signals in the non-RT controls or in the water control, samples were excluded from the analysis due to possible contaminations and the run was repeated. Analysis of the melting curves should show specific amplificons for genes to be analyzed or possible contaminations.

The quantification analysis was performed according to LightCycler® 480 Instrument Software Version 1.5. The standard curve comprised five samples prepared by serial dilution. The concentrations chosen for the standard curve lied between the expected concentration range of the gene to be analyzed. The slope of the standard curve described the kinetics of the qPCR amplification referred to as the *Efficiency*. A perfect amplification reaction would produce a standard curve with an efficiency of '2' since the amount of the gene to be analyzed would double with each amplification cycle. The qPCR efficiency was automatically calculated by the LightCycler® 480 Instrument Software according to the following formula. Efficiency of qPCR runs lied consistently between 1.8 and 2, respectively.

$$E = 10^{-1/slope} \; (e.g., slope = -3.3 \rightarrow E = 2)$$

The *Error* value, mean squared error of the single data points fit to the regression line, based on the standard curve should stay below 0.2.

The Cp-values for further analysis were obtained by the Second Derivative Maximum method of the LightCycler® 480 Instrument Software. Using this method, the turning point (Cp-value) is identified and corresponds to the maximum of the second derivative of the amplification curve. The efficiencies and Cp-values were transferred to an Excel-chart and the ratios of the genes of interest were calculated according to following formula:

$$Ratio = \frac{E_{target}^{Cp_{target}}}{E_{ref}^{Cp_{ref}}}$$

The mean values and standard deviations of ratios were calculated from triplicates of respective samples and finally, depicted in a graph.

2.5 Working with proteins

2.5.1 Determination of protein mass concentration

To determine the whole protein content in solutions, the Bradford assay was applied (Bradford 1976). The protein concentration is basically measured by the colorimetric shift of the absorption maximum from 450 nm to 595 nm. This colorimetric shift is obtained by the complex formation of the dye Coomassie Brilliant Blue-G250 with proteins changing the cationic into an anionic milieu. Since the absorption shift is directly proportional to the protein concentration, a determination of the protein content can be directly calculated by use of a BSA standard curve. The assay was conducted either in cuvettes or in 96-well plates. First for assay performance in cuvettes, a BSA standard curve (5 mg/mL, 2.5 mg/mL, 1.5 mg/mL, 0.5 mg/mL, 0.25 mg/mL, 0.1 mg/mL) was diluted using a 10 mg/mL BSA stock solution. 1 mL of the diluted Roti-Quant reaction solution (1:4 in H_2O_{bidest}) was pipetted into the cuvettes. Samples to be analyzed and blank were pipetted into the cuvettes with the final concentration of 1:2. Samples were thoroughly mixed, and the absorbance was measured with 450 nm and 595 nm filters after a reaction time of 5 minutes.

In case of an assay procedure in 96-well plates, the BSA standard curve (160 mg/L, 80 mg/L, 40 mg/L, 16 mg/L and 8 mg/L) was diluted in water using a 10 g/L BSA stock solution. Samples and blanks containing only the sample buffer were diluted in the range of 1:10 and 1:200 in water. 50 µL/well of BSA dilutions, protein samples and blanks (buffer and water only blank) were pipetted in doublets on the 96-well plate Roti-Quant reaction solution (1:4 dilution, 200 µL/well) was added in fast succession with a multi-dispenser, air bubbles were removed, and the absorbance was measured with 450 nm and 595 nm filters after a reaction time of 5 – 10 minutes. To receive the mass concentration (β) of protein in the samples, ratios of the absorbance at 450 nm to 595 nm were calculated and corrected by the respective blank ratio. The linear regression of the standard curve determined a slope to achieve the y-intercept and the mass concentration according to following equation.

$$\beta(\text{protein}) = dilution\ factor\ x\ \frac{corr.ratio\ x\ y - intercept}{slope}$$

2.5.2 Separation of proteins and peptides

For a further precise analysis, proteins needed to be separated by SDS-PAGE. Different sizes and polyacrylamide concentrations were used according to the size and amount of protein of interest. Small proteins < 20 kDa were separated on 15% gels, proteins larger than 20 kDa with 10% gels. Polyacrylamide gels were cast at least one day before electrophoresis according to Table 2.7 for mini gels and Table 2.8 for maxi gels. TEMED and APS were added as last components to the mixtures and separation gel was then immediately poured into the apparatus and covered with 5 mL isopropanol (100%). The gel was allowed to polymerize at least 45 min before the isopropanol was discarded and the stacking gel was poured on top followed by the insertion of a comb. After one hour, the gel was wrapped into wet paper towels, sealed with aluminum foil and stored at 4 °C.

Gels were mounted into separation chambers and filled with 1x running gel buffer. Before samples were applied on the gel, respective amounts of protein solutions were mixed with 5x loading buffer and H_2O_{bidest} and boiled for 5-10 min afterwards. Following short cooling on ice and centrifugation, a maximum of 30 µL for mini gels and 80 µL for maxi gels were loaded into the gel pockets. For estimation of protein sizes 3 µL of pre-stained protein marker were used as a size reference. Separation was conducted by application a constant voltage of 150 V for mini gels and 500 V for maxi gels while buffer within the chamber was mixed by a stirring bar and cooled to 10 °C in case of the maxi gels. When the run was finished, stacking gel was removed and either used for western blotting or stained with amido black solution for 10 min. Destaining was carried out with water by several cycles of heating in the microwave and mild shaking for approximately 30 minutes. Polyacrylamide gels were documented by use of an image scanner.

Table 2.7: List of components and amounts of mini gels.

Gel	Ingredients	
4% stacking gel	0.75 mL	4x stacking gel buffer
2.5 mL		
	1.82 mL	H_2O
	0.40 mL	Acrylamid, 30% / Bisacrylamid, 0.8% solution
	2.25 µL	TEMED
	22.5 µL	APS, 100 g/L solution
10 % separation gel	2.50 mL	4x separation gel buffer
7.2 mL		
	4.10 mL	H_2O
	3.33 mL	Acrylamid, 30% / Bisacrylamid, 0.8% solution
	5 µL	TEMED
	50 µL	APS, 100 g/L solution
15 % separation gel	2.50 mL	4x separation gel buffer
7.2 mL		
	2.44 mL	H_2O
	5.00 mL	Acrylamid, 30% / Bisacrylamid, 0.8% solution
	5 µL	TEMED
	50 µL	APS, 100 g/L solution

Table 2.8: List of components and volumes used for maxi gels.

Gel	Ingredients	
4% stacking gel	3.00 mL	4x stacking gel buffer
10 mL		
	7.30 mL	H_2O
	1.60 mL	Acrylamid, 30% / Bisacrylamid, 0.8% solution
	9 µL	TEMED
	90 µL	APS, 100 g/L solution
10% separation gel	7.50 mL	4x separation gel buffer
25 mL		
	10.00 mL	H_2O
	10.00 mL	Acrylamid, 30% / Bisacrylamid, 0.8% solution
	15 µL	TEMED
	150 µL	APS, 100 g/L solution
15% separation gel	7.50 mL	4x separation gel buffer
25 mL		
	7.33 mL	H_2O
	15.00 mL	Acrylamid, 30% / Bisacrylamid, 0.8% solution
	15 µL	TEMED
	150 µL	APS, 100 g/L solution

2.5.3 Western blotting

The quantification of the relative amount of specific proteins was conducted by western blotting. For this method, the wet blotting technique and a 0.45 µm pore size PVDF membrane was used. SDS-PAGE gel and six pieces of Whatman 3MM papers were equilibrated in transfer buffer for 10 min. The PVDF membrane was activated for 1 minute in 100% methanol p.A. and in addition subsequently equilibrated. For the protein transfer, a stack of three Whatman papers, the PVDF membrane, the SDS-PAGE gel and again three Whatman papers was build ensuring that air bubbles were removed. The stack was consequently put between porous sponges and mounted into the transfer chamber with the membrane orientated towards the anode.

The transfer was performed at a constant current of 1 A for 2 hours and 15 minutes under stirring the transfer buffer and cooling to 10 °C. After the run, the membrane was cropped and marked into respective pieces of interest. To avoid unspecific binding, membrane blocking was carried out for 30 minutes with skim milk blocking buffer or 2% BSA in 1x TBS-T at room temperature. The primary antibody was diluted in blocking buffer, applied on the membrane, and incubated under constant agitation at 4 °C overnight. The next day, the membrane was washed 4x with 1x TBS-T for 5 minutes, respectively. The appropriate secondary antibody-HRP conjugate was diluted in blocking buffer and incubated for 45 min at room temperature under constant shaking. Thereafter, the membrane was once again washed 4x for 5 minutes in 1x TBS-T and finally in 1x TBS.

The protein amount was detected using chemiluminescence reactions catalyzed by HRP. Luminophore and oxidation reagent were freshly mixed 1:1 and incubated for one minute on the membrane. In the following, the signal was measured with an appropriate resolution and exposure time in the ‘Fusion-FX7’ chamber. The signal was quantified by measurement of the band intensity within a defined area using the software Bio 1D. For the final determination of protein amount, values were blank corrected.

2.5.4 Homology modeling of LMX1B mutants

Homology modeling was performed using the default-modeling schedule of MODELER (version 9v22) with “Thorough Variable Target Function Schedule” and “Slow MD Annealing” (Sali & Blundell 1993) in cooperation with Gregor Madej from AG Ziegler. The X-ray structure of the Isl1 LIM domains with Ldb1 LIM-interaction domain, (PDB ID code 4JCJ) (Gadd *et al.* 2013) was used as template for LMX1B (aa 33-151). The initial sequence alignment was generated by aligning sequences of LMX1B on Isl1 LIM domain, and then improved manually by removing gaps within the secondary structure elements. For each template structure and alignment, 100 models were generated. Using Z-DOPE, a normalized atomic distance-dependent statistical potential based on known protein structures (Shen & Sali 2006), the quality of the initial models was assessed. The final models were visually inspected, and unmodeled loop regions were removed. The homeodomain of LMX1B (aa 199-257) was modeled in the same way using the X-ray structure of the Aristaless and Clawless homeodomains bound to DNA (PDB ID code 3A01) (Miyazono *et al.* 2010). The DNA double-strand was transferred from the template manually, the position and orientation were concluded from the structure alignment of the template and target molecules. Mutations were introduced by virtual mutagenesis and subsequent compensation of the charges by selecting a suitable rotamer in coot (version 0.9) (Emsley & Cowtan 2004). All images were generated using UCSF-Chimera (version 1.15, daily build 42153) (Pettersen *et al.* 2004).

2.6 Working with mice

2.6.1 Mouse transgenes

LC1

LC-1 is a transgene with direct control of luciferase and Cre recombinase expression under the bidirectional promoter P_{tet}bi-1 (Schönig *et al.* 2002). The promoter comprises seven *tetO* repeats flanked by two hCMV derived minimal promoters and is activated upon rtTA binding.

Lmx1b (H54L) knock-in

This transgenic mouse line was designed to study the LIM 1 domain function of Lmx1b. The construct *Lmx1b* (H54L) exhibits a point mutation in the LIM 1 domain of *Lmx1b*. The amino acid histidine was changed into a leucine on position 54 thereby disrupting the zinc-binding motif. These mice were generated in the own laboratory, (Lucke et al., unpublished), and display the main tool of this thesis.

Lmx1b (C95F) knock-in

These mice harbor an amino acid substitution of a cysteine into a phenylalanine on position 95 of the *Lmx1b* gene, Lucke et al., unpublished. Likewise, the H54L construct, the point mutation C95F abolishes the zinc-binding in the LIM 2 domain. This transgenic mouse line was used to further investigate the LIM 2 domain function of Lmx1b.

Lmx1b knock-out

This mouse line was designed to study *Lmx1b* during limb development (Chen *et al.* 1998a). In literature, characterization of *Lmx1b* knock-out mice demonstrated an essential function of Lmx1b during nail-patella syndrome, since mutations in the human *LMX1B* gene result in nail-patella syndrome. Mice carry a deletion of exons 3 to 7 of the *Lmx1b* gene. These exons encode the second LIM domain, the homeodomain and most of the carboxy-terminal region of *Lmx1b* (Chen *et al.* 1998a). Mice heterozygous for this deletion displayed no defects on a BL6 background. Within this study, *Lmx1b* knock-out mice served as control mice. Mice were kindly provided by the lab of R. Johnson.

Lmx1b, flox

This transgenic mouse line harbors two loxP sites that were introduced into introns downstream of exon 4 and upstream of exon 6 of the endogenous murine *Lmx1b* (Suleiman *et al.* 2007). The expression of Cre recombinase results in an in-frame deletion of the homeobox sequence from exons 4 to 6. Mice were kindly provided by the lab of R. Johnson (affiliation).

mTmG transgene

The reporter construct *mTmG* consists of membrane-targeted versions of tdTomato (mT) and EGFP (mG) under the control of a chicken β-actin core promoter with a CMV enhancer (Muzumdar *et al.* 2007). The tdTomato and a downstream polyadenylation (pA) signal are flanked by *loxP* sites resulting in a mT expression in all kinds of tissue under normal conditions. In case of a Cre recombinase expression, mT and the pA signal are removed, and the mG expression starts. This construct allows to mark specific cell types with green fluorophores by specific promoter controlled Cre expression. Mice were kindly provided by T. B. Huber (affiliation).

NPHS2 rtTA

The *rtTA* gene (reverse tetracycline-controlled transcriptional transactivator) originally derived from the *E. coli* tetracycline-resistance operon. The encoded protein binds to the *tetO* region and activates the transcription exclusively if tetracyclines, for example doxycycline, are present. The gene was set under the regulatory control of a 2.5 kbp fragment of the human *NPHS2* promoter (Shigehara *et al.* 2003).

2.6.2 General handling and breeding

Mice have been bred in Eurostandard type II and III cages in a conventional animal laboratory of the University of Regensburg. 21 days after birth the offspring was separated from the mother and biopsied for genotyping. The tissue was collected by ear punching according to a standardized code serving to mark the animals. Animals had unlimited access to drinking water and complete food in 12 hours day/night cycle. Knock-in mouse lines were mated with C57BL/6J mice of the company ‘Charles River Laboratories’ at least ten times to ensure a homogenous genetic background. The multiple transgenic mouse lines were mated between each other since backcrossing of every single transgenic mouse line on a C57BL/6J background extended to ten times. The animal experiment for analyses of the therapeutic approach for the treatment of nail-patella syndrome was accomplished according to the application documents of the ‘Regierung von Unterfranken’ that were approved under reference number 55.2 2532-2-1170.

2.6.3 Genotyping

DNA isolation

Mouse biopsies were digested with 0.2 g/L proteinase K in 700 µL tail buffer overnight at 50 °C under constant rotation. The following day, samples were vortexed and centrifuged at 10,000 x g for 30 minutes, room temperature to remove insoluble material. Subsequently, the supernatant was transferred to a fresh micro vial containing 600 µL of 100% isopropanol and was mixed thoroughly by inverting to precipitate DNA. After centrifugation at 10,000 x g for 30 minutes, room temperature, the supernatant was discarded and 500 µL of 70% ethanol were added and mixed by inverting several times. In a last step, the vial was centrifuged at 10,000 x g for 15 min, room temperature, the ethanol was discarded, and DNA was completely dried at 40 °C for at least 30 min. To resolve the DNA, 30 µL of TE buffer were added and the vials were incubated overnight at 50 °C under constant rotation in a hybridization oven.

PCR

For assessment of the mouse genotypes for all transgenes, the PCR method was applied. In all cases, 0.5 µL DNA were diluted with DNA free water to 20 µL in a 0.2 mL micro tube. The master mix containing the appropriate primers of respective genotype to be analyzed, was freshly prepared according to Table 2.9. Immediately after pipetting, samples were mixed, put into a thermal cycler, and the PCR program was started (Table 2.10). After the run finished, the samples were kept at 4 °C. For each PCR run a water control was prepared in addition to a positive control of a known sample of the respective genotype. A complete list of used primers can be found in chapter 2.1.6.

Table 2.9: Master mixes for genotyping mouse transgenes: *Cre*, *Lmx1b* floxed, *Lmx1b* (H54L), *Lmx1b* (C95F), *Lmx1b* (KO), *mTmG*, *P2.5 rtTA*.

Ingredients	Volume for all transgenes
10x Thermopol buffer	2.5 µL
Primer (100 µM), respectively	0.15 µL
dNTPs (10 mM)	0.5 µL
Taq polymerase	0.25 µL
H_2O	Ad 25 µL

Table 2.10: PCR protocols for all transgenes.

Step	T	t	
Melting DNA	94 °C	3 min	
Melting amplicon	94 °C	30 sec	35 cycles
Annealing	58 °C	1 min	
Elongation	68 °C	1 min	
Final elongation	68 °C	5 min	

Agarose gel electrophoresis

DNA loading buffer (5x) was added to PCR samples and mixed thoroughly. For amplicons with a size of < 300 bp, xylene cyanol FF was applied as a dye, in case the desired amplicons were > 300 bp, bromophenol blue was used. A 2% agarose gel was prepared by solving 3 g of agarose in 150 mL 1x TAE buffer via heating in a microwave oven. In order to visualize the DNA, ethidium bromide (60 µL/gel) was added as an intercalation dye. The dissolved gel was poured in the apparatus, the combs were placed, and remaining air bubbles were removed. After approximately 30 minutes incubation at room temperature, the gel cooled down and became solid. Thereafter, 12.5 µL of the PCR product including the loading buffer were applied per well. The 2-log DNA ladder served as a size estimation standard. The electrophoresis run was carried out in 1x TAE buffer at a constant voltage of 150 V for 20 to 40 minutes. DNA bands were visualized and documented by the ultraviolet illumination in the GelDoc™ system.

2.6.4 Collection and analysis of urine samples

Urine samples of animals were spontaneously voided urine samples (spot urine). For a qualitative determination of urinary proteins, SDS-PAGE with 1 µL spot urine was performed. To estimate the urine albumin content, different BSA amounts were loaded on the gel, such as 1, 3, 10, and 30 µg of BSA. The protocol for SDS-PAGE is described in 2.5.2. For calculation of the protein creatinine ratio, the protein content was measured using the Bradford test with a sample dilution of 1:20 according to description in 2.5.1.

The urine creatinine mass concentration was analyzed by the Jaffe reaction. Due to urine volume limitations, urine creatinine was measured only once with 5 µL/well in a 96-well plate. Urine was diluted to 50 µL with water (1:10), whereas water blank (50 µL) and a creatinine standard curve (30, 15, 7.5 and 3.75 mg/L) were pipetted in doublets. 150 µL of the master mix according to Table 2.11. Were added in a fast sequence. After 30 minutes of reaction time, the colorimetric product was analyzed spectrophotometrically at 540 nm. To determine the mass concentration of the samples, a linear regression of the standard curve was calculated yielding the mass concentration by means of the equation (3)

$$\beta(creatinine) = \text{dilution factor x } \frac{corr.\ A520\ x\ y-intercept}{\text{slope}} \quad (3)$$

Table 2.11: Master mix for Jaffe reaction for one urine sample.

Volume	Ingredients	
50 µL	1.2 M	Trichloroacetic acid
50 µL	35 mM	Picric acid
50 µL	1.6 M	Sodium hydroxide solution

2.6.5 E18.5 breeding and preparation

Lmx1b homozygous knock-out or knock-in mouse embryos were obtained by mating heterozygous male with heterozygous female mice. Matings were time-dated using noon on the day of putting mice into a common cage until the next morning post coitum, when they were separated. 18.5 days later, embryos were harvested from the pregnant mother. External phenotypes were manifested and documented. Then, kidneys were isolated and fixed in 4 % PFA in 1x PBS pH 7.4 for histology (2.8.2), or in 2% glutaraldehyde in 0.1 % cacodylate buffer for electron microscopy (2.8.5). Some kidneys were directly cryo-embedded for immunofluorescence staining according to 2.8.4. In addition, some embryos were further processed for skeletal imaging by µCT (2.7.2). All embryos were genotyped to confirm homozygous, heterozygous or wild-type *Lmx1b* of animals.

2.6.6 Breeding of inducible *Lmx1b* knock-out and *Lmx1b* knock-in mice

To receive fivefold transgenic mice, that harbor one copy of the *Lmx1b* gene flanked by *loxP*-sites and one copy of the *Lmx1b* knock-in, either H54L or C95F, inducible podocyte-specific *Lmx1b* knock-out mice as described in (Burghardt *et al.* 2013) were mated either with *Lmx1b* (H54L) or *Lmx1b* (C95F) knock-in mice (Lucke *et al.*, unpublished). The induction of the podocyte specific *Lmx1b* knock-out was performed as described before (Setzer 2020). Briefly, mice with an age of seven weeks received 2 mg/mL of doxycycline in the drinking water to induce the Cre expression for seven consecutive days. Normal drinking water as replaced by induction solution containing doxycycline and sucrose in the morning. The solution was administered in lightproof bottles in excess and freshly prepared when spot urine samples were collected every second day.

2.6.7 Bortezomib treatment of inducible podocyte-specific compound heterozygous *Lmx1b* mice

Inducible podocyte-specific compound heterozygous *Lmx1b* mice with an age of seven weeks received 2 mg/mL of doxycycline and 5% sucrose in the drinking water to induce the Cre expression for seven consecutive days. On the day of beginning the experiment, normal drinking water was replaced by a solution containing doxycycline and sucrose. The solution was administered in lightproof bottles in excess and freshly prepared every second day. In addition, mice were weighed, injected with bortezomib at a dose of 0.3 µg/g body weight and meanwhile spot urine was collected every other day Figure 2.1. The experimental group was intraperitoneally injected with bortezomib, whereas the control group received DMSO injections according to the same procedure in order to exclude potential effects of the solvent of bortezomib. Injections were dissolved in sterile 1x PBS pH7.4. On day seven, mice were perfused, spot urine was analyzed by SDS-PAGE and protein/creatinine ratio was determined according to 2.6.4. The animal experiment was accomplished according to the approval of the 'Regierung von Unterfranken' under reference number 55.2 2532-2-1170.

Experimental group received bortezomib (0.3 µg/g body weight in 1x PBS pH 7.4):

Nphs2::rtTA, *tetO*::Cre, *mTmG* he, *Lmx1b* $^{H54L/lox}$ or *Lmx1b* $^{C95F/lox}$ or *Lmx1b* $^{+/lox}$

Control group received the solvent DMSO (0.3 µg/g body weight in 1x PBS pH 7.4):

Nphs2::rtTA, *tetO*::Cre, *mTmG* he, *Lmx1b* $^{H54L/lox}$ or *Lmx1b* $^{C95F/lox}$ or *Lmx1b* $^{+/lox}$

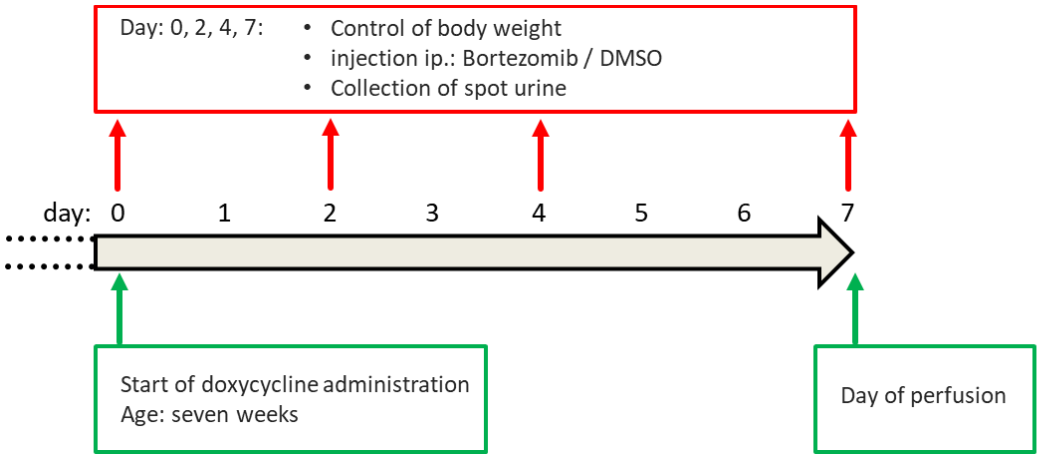

Figure 2.1: Timeline of bortezomib treatment in inducible podocyte-specific compound heterozygous *Lmx1b* mice.

2.7 Working with mice embryos (E18.5)

2.7.1 Whole-mount skeletal staining

E18.5 embryos were collected following euthanization of timed pregnant females and placed in 1x PBS pH 7.4 at room temperature. Extraembryonic membranes encircling the embryo were removed. Thereafter, embryos were eviscerated by creating a horizontal slit in the skin at the abdomen using dissecting scissors. Then, organs were isolated for further processing. In a next step, in addition the skin from arms was removed by generation a vertical slit on the ventral and dorsal surfaces of the fore and hind limbs. Embryos were placed in glass scintillation vials containing 95% ethanol and were fixed 1-2 days at 4 °C under constant agitation. In a next step, the 95% ethanol was replaced with 100% acetone and incubated overnight at room temperature under constant shaking. On the next day, acetone was removed, washed twice with 95% ethanol, and incubated in the Alcian blue solution for at least 36 hours to stain cartilage. Thereafter, the Alcian blue stain was removed, embryos were washed twice in 95% ethanol and incubated in 95% ethanol overnight at room temperature under constant agitation. At next, the embryo tissue was cleared by incubation in 1% KOH for 2-3 hours shaking at room temperature followed by the Alizarin red stain for 3 hours. Alizarin red was removed and replaced with 1% KOH for 12 hours overnight for clearing the embryos. Finally, embryos were transferred to a 50% glycerol:50% (1%) KOH solution at room temperature until the tissue appears transparent. Once cleared, embryos were transferred to a 100% glycerol for long-term storage

2.7.2 µCT analysis of skull, reconstructing of volumes, 3D measurements

For µCT analysis, E18.5 mice were previously fixed in 95% ethanol at 4 °C for at least 2 days. µCT analysis was performed using the phoenix v | tome | x s 240/180 research edition from Baker Hughes Digital Solutions GmbH in cooperation with Dr. Birgit Striegl from the Department of Mechanical Engineering at the Ostbayerische Technische Hochschule Regensburg. The scanning parameters for the images were as followed: 23 kV voltage, 600 µA current, 500 ms exposure time, 1000 images, voxel size 30 – 32 µm. Reconstruction volumes were processed using the respective manufacturer´s software phoenix datos |x 2 reconstruction 2.4.0. The threshold value defining the material and background was set to 0.200 ± 0.005 absorption coefficient, respectively. The 3D images, the surface area and the volume parameters were determined using Volume Graphics VG Studio Max 2.2.3. We gratefully thank RCBE (Regensburg Center of Biomedical Engineering) for the support by µCT facility and we acknowledge the support from the Deutsche Forschungsgemeinschaft (DFG) in frame of the program ‘Forschungsgeräte’ (INST 102/11 – 1 FUGG).

2.8 Working with kidney sections

2.8.1 Kidney perfusion fixation

Perfusion procedure was performed as described before (Setzer 2020). On the day of perfusion, mice were first weighed, and a final spot urine sample was collected. Thereafter, mice were anesthetized by two intraperitoneal injections (0.12- 0.15 mg/g body weight for adult animals) of a Narcoren working solution and tail biopsies were taken for re-genotyping. After opening the *peritoneum*, the *arteria* and *vena iliaca communis* in addition to the aorta below the renal arteries were clamped. The abdominal aorta was sectioned horizontally halfway, and the tubing was inserted and tightly fixed with a string. In a final step, the *vena cava inferior* was sectioned, subsequently, the aorta clamp was removed, and the perfusion fixation was initiated with 4% PFA in 1x PBS pH 7.4. The perfusion flow was carried out at a constant pressure of 180 – 200 mbar for three minutes. In the following, the fixation tubing was removed and flushed with heparin. Both kidneys were isolated and bisected vertically to the longitudinal axis and further processed depending on the embedding technique.

2.8.2 Embedding and slice preparation

Paraffin embedding and slice preparation

For a further analysis of kidney sections, the tissue was embedded in paraffin. Kidneys were additionally fixed in 4% PFA in 1x PBS pH 7.4 for one day at constant agitation. After post-fixation, the tissue was washed two times with 1x PBS followed by an incubation of an ascending alcohol series using an automated tissue processor according to liquids and intervals listed in Table 2.12. The paraffin-embedding was conducted on a heated paraffin dispensing module with an orientation of the slice plane towards the bottom of the paraffin block. Paraffin blocks

were stored at room temperature and cooled down previously cutting. Tissue slices were produced by use of a microtome with the diameter of 6 µm and immediately relaxed in a 40 °C water bath. Two to three slices were fielded onto one microscope slide and after drying on a 40 °C heated plate, the control of the slice quality with a light microscope followed. In case of a slice preparation for immunofluorescence staining, Superfrost™ Plus microscope slides were used. In a final step, the slices were completely dried overnight at 37 °C.

Table 2.12: Liquids and intervals applied for the ascending alcohol series.

Liquid	Intervals
Isopropanol, 50%	90 minutes
Isopropanol, 70%	90 minutes
Isopropanol, 80%	90 minutes
Isopropanol, 96%	90 minutes
Isopropanol, 100%	90 minutes
Isopropanol, 100%	90 minutes
Isopropanol, 100%	90 minutes
Xylol, 100%	90 minutes
Xylol, 100%	90 mintues
Melted paraffin (60 °C)	240 minutes
Melted paraffin (60 °C)	240 minutes
Melted paraffin (60 °C)	240 minutes

Cryo embedding and slice preparation

In this study, another embedding method was applied, particularly, the cryo embedding. 4% PFA in 1x PBS pH 7.4 fixed kidneys were further processed in 18% sucrose in 1x PBS pH 7.4 for 4 hours under constant agitation. In case of E18.5 kidney preparation, the tissue was directly put into the cryomold® with the cutting edge orientated towards the bottom and embedded in Tissue-Tek®. After ensuring that air bubbles are removed, the cryomold including the tissue was frozen in the gas phase above liquid nitrogen and stored at -80 °C. Tissue slices were taken with

a cryostat with the diameter of 7 µm, dried at room temperature for 20 minutes and further used for immunofluorescence staining.

Epon embedding and slice preparation

Kidneys, perfused or in case for E18.5 tissue non-perfused, were post-fixed in 2% glutaraldehyde in 0.1 M sodium cacodylate buffer pH 7.4 for at least three days at 4 °C under constant agitation. In the following, kidneys were divided into small pieces with a maximum edge length of 2 mm. Kidney particles were washed with 0.1 M sodium cacodylate buffer and further processed with osmium tetroxide at room temperature for contrast enhancement and tissue conservation during dehydration. Towards another washing step, samples were dehydrated in ethanol and acetone. Subsequently, tissue was treated with an acetone / epon mixture and transferred into freshly prepared epon. The epon with the embedded tissue polymerized at 60 °C for at least two days. The procedure was carried out according to listed steps in Table 2.13. Finally, tissue slices were received by an ultramicrotome with the diameter of 50 – 70 nm and placed on a grid for transmission electron microscopy analysis.

Table 2.13: List of liquids and intervals for epon embedding of glutaraldehyde-fixed kidney pieces.

Liquid	Intervals
0.1 M sodium cacodylate buffer	3x, 20 minutes
10 g/L Osmium tetroxide in 0.1 M sodium cacodylate buffer	2 hours
0.1 M sodium cacodylate buffer	4x, 5 minutes
Ethanol, 50%	30 minutes
Ethanol, 70%	30 minutes
Ethanol, 90%	30 minutes
Ethanol, 96%	30 minutes
Ethanol, 100%	30 minutes
Acetone, 100%	3x, 15 minutes
Acetone / epon (1:1 mixture)	overnight

Epon	3 hours (30 °C) and 2 days (60 °C)

2.8.3 Staining of paraffin sections

Deparaffinization and rehydration

For proper staining of tissue slices on the microscope slide, in a first step the paraffin must be eliminated from the tissue and the tissue must be rehydrated. This was guaranteed by treating the slices with a descending alcohol series according to Table 2.14 (I). In this connection, slides were placed into a glass cuvette and shifted from one reservoir to the next one. Slides were shortly incubated in double-distilled water until all slides were rehydrated.

Table 2.14: List of the descending alcohol series for deparaffinization and rehydration of paraffin slices (I). List of ascending alcohol series for dehydration of H&E stained slices (II).

Liquid	Intervals (I)	Intervals (II)
Xylol, 100%	10 minutes	10 minutes
Xylol, 100%	10 minutes	10 minutes
Isopropanol, 100%	2 minutes	2 minutes
Isopropanol, 100%	2 minutes	2 minutes
Isopropanol, 96%	2 minutes	2minutes
Isopropanol, 80%	2 minutes	8 seconds
Isopropanol, 70%	2 minutes	3 seconds
Isopropanol, 50%	2 minutes	
bidest. H_2O	> 1 minute	

H&E staining of paraffin sections

Previously to staining of deparaffinized and rehydrated sections with hematoxylin, the basophilic stain solution was filtered through a folded filter to get rid of precipitated particles. Hematoxylin staining was performed for 3 minutes at room temperature followed by a short tap water washing step. Subsequently, the sections were differentiated two times with 0.1% HCl in 70% isopropanol for few seconds for removal of excess color. Thereafter, sections were additionally washed by tap water for 10 minutes. The acidophilic staining was carried out with a freshly prepared, 1 g/L eosin solution and one drop of acetic acid per 100 mL stain solution. The eosin staining was realized for 40 seconds at room temperature followed by a short tap water washing step. For removal of any water from the sections, finally the ascending alcohol series was conducted according to Table 2.14 II. Completely dehydrated and stained sections were fixed by DePeX embedding medium and cover slips. Slides were documented with a slide scanner equipped with a 40x objective.

Immunofluorescence staining of paraffin sections

Due to the paraffin embedding, epitopes of the desired proteins are not accessible for antibodies. First, epitopes were unmasked by an autoclaving step in a retrieval buffer for 10 minutes at 121 °C. After cooling down for 20 minutes, the container including the slides was removed and further cooled down for 20 minutes. Subsequently, the slides were washed in tissue permeabilization buffer in a glass cuvette. Prior to blocking the tissue with 30 µL of histoblock buffer for 30 minutes at room temperature, a water-repellent circle was drawn around the tissue sections using Super PAP Pen Liquid Blocker. All primary antibodies were diluted in histoblock buffer and 25 µl of antibody solution were pipetted onto the tissue after removal of prior blocking buffer. The slides were incubated in a humidity chamber at 4 °C overnight. On the next day, the slides were washed 3x in tissue permeabilization buffer in a glass cuvette. Thereafter, the water-repellent circle was

dried carefully with a task wipe and the tissue sections were incubated with 25 µL of secondary antibodies diluted in histoblock buffer for 45 minutes at room temperature in a humidity chamber under exclusion of light. Next to the incubation, slides were washed 3x with 1x PBS pH 7.4 followed by liquid removal from the slides by tapping. For the DNA staining, tissue sections were incubated with 30 µL of Höchst in 1x PBS pH 7.4 solution for 1 minute at room temperature and subsequently washed 3x with 1x PBS pH 7.4. Finally, sections were fixed air bubble freely in Mowiol and cover slips. The viscous embedding medium was allowed to solidify at 4 °C for at least 2 hours. Sections were subsequently analyzed using a confocal microscope.

2.8.4 Staining of cryosections

Cryosections were used to stain Lmx1b of E18.5 *Lmx1b* knock-in and knock-out murine kidneys. First, sections were washed using tissue permeabilization buffer in a glass cuvette. Prior to encircling each section with the water-repellant Super PAP Pen Liquid Blocker, slides were dried with task wipes. The cryosections then were blocked with 30 µL histoblock buffer, subsequently, the blocking buffer was removed and 30 µL of the Lmx1b antibody solution, diluted in histoblock buffer was pipetted onto the slides and incubated overnight at 4 °C. On the next day, slides were washed 3x with tissues permeabilization buffer in a glass cuvette and the water-repellent circle was dried with a task wipe. 30 µL of the secondary antibody dilution in histoblock buffer were pipetted onto the tissue sections and incubated for 45 minutes at room temperature in a humidity chamber under exclusion of light. After incubation, slides were washed 3x in 1x PBS pH 7.4 and the liquid was removed from the slides. Nuclei staining was performed using a Höchst staining buffer for 1 minute at room temperature followed by a 3x washing step with 1x PBS pH 7.4. In a final step, tissue sections were mounted with Mowiol and cover slips allowing to solidify for at least for 2 hours at 4 °C prior to confocal microscope analysis.

2.8.5 Contrasting of epon sections and quantification of filtration slits

The sections placed in the grid were washed with filtered double distilled H2O (ddH2O), negative stained with 1% uranyl acetate solution for 30 minutes under exclusion of light and washed again 10x with filtered ddH20. Finally, a contrast enhancement with 3% lead citrate solution for 1 minute was conducted and sections were washed once more 10x with filtered ddH2O. Transmission electron microscopy pictures of two glomeruli per mouse were taken at magnifications of 400x, 700x, 3 000x, 7 000x and 20 000x. To quantify the frequency of filtration slits, blinded 7 000x magnified micrographs were examined. The length of the basement membrane was measured at the border to neighboring podocytes using the software ImageJ and gaps between podocyte foot processes were counted to calculate the ratio slits/µm.

2.9 Working with cells

2.9.1 Cultivation of mammalian cells

General handling

To ensure that cells were kept under sterile conditions, general handling was performed in a laminar flow bench. Cells were cultivated with 5% CO_2 and 95% relative humidity in a CO_2 incubator. For cultivation cell culture flasks with a filter cap harboring a size of 25 cm^2 or 75 cm^2 were used with either 5 mL or 10 mL of specific medium. Before placing the equipment into the bench, it was sterilized with 70% ethanol, self-made liquids were autoclaved or sterile filtered. Consumables were purchased sterile. Depending on the specific cell line, media with different additives were used according to Table 2.15.

Table 2.15: List of cell culture media and additives.

Cell line	Medium	Additive	
HtTA-1	DMEM	10%	FCS
		200 µg/mL	G418
HtTA-1/myc-LMX1B (WT)	DMEM	10%	FCS
		200 µg/mL	G418
		300 µg/mL	Hygromycin
		100 ng/mL	Doxycycline
HtTA-1/myc-LMX1B (H54L)	DMEM	10%	FCS
HtTA-1/myc-LMX1B (C95F)		200 µg/mL	G418
HtTA-1/myc-LMX1B (V242D)		1 µg/mL	Puromycin
		100 ng/mL	Doxycycline

Subculture

Cells were passaged when reached approximately 100% confluency manifested by light microscopy. For sub-culturing, cells were washed twice with 1x PBS pH 7.4 and thereafter were incubated with 1 mL (T25 cell culture flask) or 1.5 mL (T75 cell culture flask) of a Trypsin/EDTA solution for approximately 5 – 10 minutes. After complete detachment of the cells estimated by light microscopy, at least 4 mL of cell culture medium including FCS was added and cells were split 1:5 – 1:20 depending on cell growth rate and density.

Cell freezing

For storage, cells in a T75 cell culture flask were frozen with 80% confluency. Cells were washed twice with 1x PBS pH 7.4 and subsequently trypsinized. In the following, trypsin reaction was stopped by 8.5 mL of specific medium. The cell suspension was transferred into a 15 mL tube and centrifuged at 365 g for 5 minutes at 4 °C. The cell pellet was resuspended in 4.5 mL of 90% FCS and 10% DMSO as a cryoprotectant. In a next step, 1.5 mL of the cell suspension was immediately transferred to a 1.8 mL cryovial (1.8 mL per 1 – 2 million cells) and placed into polystyrene container at -80 °C to guarantee slow freezing at a rate of approximately 1 °C per minute. For short-term storage, cells were kept at -80 °C, for long-term storage cells were placed in the gas phase of a liquid nitrogen container.

Cell thawing

Frozen cells were rapidly defrosted by hand warmth until they were thawed by pipetting specific cell culture medium on top. The cell suspension was diluted in 10 mL of cell culture medium and transferred in a T75 cell culture flask. On the next day, cell culture medium was replaced by fresh medium.

Mycoplasma testing

To exclude a potential mycoplasma contamination meanwhile cell cultivation, cells in culture were tested for mycoplasma every three months. Briefly, cells were cultivated in antibiotic-free medium until 100% confluency for at least 3 days. 100 µL of the cell medium were collected and centrifuged for 3 minutes at 17,000 x g at room temperature. Samples were tested by a nested PCR experiment listed in Table 2.16 and Table 2.17. Preparation of PCR reactions was performed under a laminar flow bench. After completion of the PCR runs, products were analyzed on a 2% agarose gel according to procedure described in 2.6.3. The PCR 2 product with a size of 145-240 bp was critical for assessing a mycoplasma contamination. All cell clones used in this study, were negative for mycoplasma throughout experiments.

Table 2.16: Mastermix of PCR for Mycoplasma test.

Ingredients	PCR 1 (360-380 bp)	Ingredients	PCR 2 (145-240 bp)
10x Thermopol buffer	5 µL	10x Thermopol buffer	5 µL
Primer F1 (0.2 µM)	1 µL	Primer F2 (0.2 µM)	1 µL
Primer R1 (0.2 µM)	1 µL	Primer R2 (0.2 µM)	1 µL
dNTPs (0.2 mM)	1 µL	dNTPs (0.2 mM)	1 µL
Template: supernatant	5 µL	PCR 1 product	0.5 µL
/positive control pJET/Myco	50 ng		
/RT-PCR grade H_2O	5 µL		
Taq (1.25 U)	0.25 µL	Taq (1.25 U)	0.25 µL
RT-PCR grade H_2O	Ad 36.75 µL	RT-PCR grade H_2O	Ad 41.25 µL

Table 2.17: Protocol for Mycoplasma PCR 1 and 2.

Step	T	t	
Melting DNA	94 °C	3 min	
Melting amplicon	94 °C	30 sec	35 cycles
Annealing	55 °C	2 min	
Elongation	68 °C	1 min	
Final elongation	68 °C	5 min	
Hold	10 °C	∞	

2.9.2 Generation of stably transfected cell lines

To establish the tet-off human HeLa (HtTA) cell lines stably expressing the human wild-type LMX1B (WT) protein (HtTA-1/myc-LMX1B (WT)) and its mutated counterparts LMX1B (H54L) (HtTA-1/myc-LMX1B (H54L)), LMX1B (C95F) (HtTA-1/myc-LMX1B (C95F)), and LMX1B (V242D) (HtTA-1/myc-LMX1B (V242D)) the parental HtTA-1 cell line (kind gift from H. Bujard; (Gossen & Bujard 1992b)) was transfected according to Table 2.18. Stable transfection was performed using poly-L-ornithine in the presence of a plasmid conferring resistance either hygromycin or puromycin as listed in Table 2.18.

Table 2.18: List of plasmids for stable transfection of HtTA-1 cells.

Plasmid	Resistance plasmid	Source
pUHD10-3/myc-LMX1B (WT)	pWE4, hygromycin	(Rascle *et al.* 2009)
pUHD10-3/myc-LMX1B (H54L)	pWE3, puromycin	Present work
pUHD10-3/myc-LMX1B (C95F)	pWE3, puromycin	(Rascle *et al.* 2009)
pUHD10-3/myc-LMX1B (V242D)	pWE3, puromycin	Present work

For this study, the stably transfected cell lines HtTA-1/myc-hLMX1B (WT) and HtTA-1/myc-hLMX1B (C95F) already existed from a previous work (Rascle *et al.* 2009), hence the other two cell lines were generated as previously described (Dong *et al.* 1993). Briefly, one day prior to transfection, cells were split 1:5 in a T25 flask. On the next day, for transfection medium was thoroughly mixed as described in Table 2.19.

Table 2.19: Components for stable transfection of HtTA-1 cells.

Ingredients		Quantity
DMEM, including 10% FCS	Medium	3 mL
Poly-L-ornithine (10 mg/mL Sigma P3655)	Transfection reagent	10 µg/mL
DNA	Respective plasmid	8.0 µg
pWE3	Resistance plasmid	0.8 µg

The medium of cells in the T25 flask with a confluency of 70% was sucked off, the transfection mix was promptly added, and cells were incubated for 6 hours at 37 °C. Thereafter, medium was aspirated, and cells were incubated for 3.5 minutes at room temperature with DMEM medium including 10% FCS and 30% DMSO. The cells were then rapidly washed twice in 1x PBS pH 7.4 and incubated overnight at 37 °C in 5 mL of fresh medium (DMEM, 10% FCS, G418 [200 µg/mL] and doxycycline [100ng/mL]). The day after, cells were washed twice in 1x PBS pH 7.4 and trypsinized in 1 mL of Trypsin/EDTA solution for 5 min at 37 °C. Trypsin reaction was stopped by addition of 14 mL medium (DMEM, 10% FCS, G418 [200 µg/mL], doxycycline [100ng/mL]) followed by seeding the cells in 4 different P10 cell culture dishes with 0.3 mL, 1.0 mL, 3.0 mL or 10 mL of cell suspension. The volume of the P10 plates was adjusted up to 10 mL with medium (DMEM, 10% FCS, G418 [200 µg/mL], doxycycline [100ng/mL]), respectively. Transfected cells were incubated for one day at 37 °C and subsequently, medium was replaced by medium including selective antibiotic puromycin (DMEM, 10% FCS, G418 [200 µg/mL], puromycin [1 µg/mL], doxycycline [100ng/mL]). Cells, which had successfully implemented the resistance plasmid within the genome, were able to develop a resistance against puromycin. Medium was changed every 2 days accompanied by screening of positive clones that survived the presence of puromycin after approximately 10 days. Definite circular clones with a size of 100-200 cells were isolated in a volume of 200 µL, transferred into a 24-well plate and grew further until 70-80% of confluency followed by splitting for clone testing. Antibiotic resistant clones were split into two separate P6 dishes and once confluent tested for proper LMX1B expression. One third of the trypsinized cell suspension was transferred back into the respective 24-well plate for further cultivation. To test clones, protein expression in one P6 dish was induced by doxycycline-free medium for 4 to 5 days until 70% confluency compared to non-induced cells of the counterpart P6 dish containing doxycycline in the medium. Analysis of positive clones was performed applying immunofluorescence staining and western blotting as described in chapters 2.5.3, 2.9.4, and 2.9.4.

2.9.3 Induction of LMX1B expression in stably transfected cells

In stably transfected HtTa-1/myc-LMX1B cells the expression of LMX1B was repressed under the presence of doxycycline [100 ng/mL]. To start the protein synthesis of LMX1B, doxycycline was removed from the medium. For testing the optimal LMX1B protein expression of all stably transfected cells described in 2.9.2, an induction series was applied for 0, 1, 3, 5, 6, and 7 days in doxycycline-free medium to identify appropriate protein levels for further analyses. As a negative control, uninduced cells were additionally analyzed. After successful clone testing, LMX1B protein expression was induced for at least 6 days in following different approaches, respectively. In parallel throughout all experiments, cells with medium comprising doxycycline [100 ng/mL] were analyzed as a control. In case of analysis of expression levels over time, the 0h sample always referred to point in time of LMX1B expression after a 6-day induction.

2.9.4 Fixation and immunofluorescence staining

For immunofluorescence staining of cells, coverslips were fixed onto the bottom of cell culture dishes prior to cell seeding. Cells were cultivated until 80% confluency. Then, coverslips were cautiously extracted using fine forceps, transferred into a 24- well plate, and washed twice with 1x PBS pH 7.4. Afterwards, cells were fixed by adding 200 µL of 4% PFA in 1x PBS pH 7.4 for 30 minutes at room temperature. Subsequently, fixation reagent was discarded, and cells were washed twice with 1 mL of 1x PBS pH 7.4. In a next step, cells were permeabilized with 500 µL of histoblock buffer for 30 minutes at room temperature. Primary antibodies were diluted in histoblock buffer and 250 µL of antibody dilution were pipetted on top of the coverclips. The 24-well plates were air-tightly sealed using Parafilm® and incubated at 4 °C overnight. On the next day, cells were washed 3x with 1 mL of cell permeabilization buffer and incubated with secondary antibodies, diluted in histoblock buffer, for 30 minutes at room temperature in a humidity chamber under exclusion of light. Thereafter, cells were washed again 3x with 1 mL of cell

permeabilization buffer and nuclei were stained with Hoechst diluted in 1x PBS pH 7.4 for 1 minute at room temperature. After final washing steps with 3x 1 mL cell permeabilization buffer, coverslips were inversely mounted with Mowiol on microscopy slides. The viscous embedding medium was allowed to solidify at 4 °C for at least 2 hours. Slides were subsequently analyzed using an epifluorescence microscope.

2.9.5 Cell lysis

For lysis of HeLa cells, cells were harvested at 100% confluency. Different lysis buffers were used depending on the nature of experiments. All buffers and solutions were pre-cooled and cells were kept on ice. After removal of the medium, cells were carefully washed twice in 5 mL 1x PBS pH 7.4. Then, 600 µL of ice cold 1x PBS pH 7.4 were pipetted onto the cells followed by scraping off with a cell scraper. The cell suspension was transferred into a fresh reaction tube and centrifuged at 5 000 rpm for 5 minutes at 4 °C. For a harsh cell lysis using a urea lysis buffer, the supernatant was sucked off and the pellet was resuspended in 200 µL - 400 µL of denaturing urea lysis buffer followed by an incubation on ice for 15 minutes. Afterwards, the denatured cell lysates were centrifuged for 30 minutes at 15 000 rpm and 4 °C for pelleting nucleic acids. Finally, the DNA pellet was sucked off with a pipette tip and the lysates were stored at -80 °C until further analysis. Finally, protein concentration was determined according to 2.5.1 and lysates were directly forwarded to following experiments or stored at -80 °C until further analysis.

2.9.6 Analysis of LMX1B protein stability by the Cycloheximide Chase Assay

The comparison of LMX1B protein stability in HeLa cells has been achieved by treatment with cycloheximide. This is an inhibitor of protein biosynthesis due to its prevention in translational elongation. It is broadly used in terms of determination of the half-life of a given protein. The cycloheximide chase assay was carried out as briefly described. LMX1B protein expression in stably transfected HeLa was induced for 6 days in doxycycline-free medium. Respective medium was changed every 2 days. The day prior to the cycloheximide chase assay, cells were split from 2-3 P10 dishes, pooled and resuspended in 5.5 mL of respective medium. Subsequently, 500 µL of cell suspension was seeded in 10 separate P6 dishes and cultivated overnight at 37 °C, respectively. On day 6 of LMX1B induction, the cycloheximide stock with 10 mg/mL in sterile water was diluted in respective medium at the working concentration of 100 µg/mL. The medium in P6 dishes was removed and medium containing cycloheximide [100 µg/mL] was added into each dish. Cells were incubated at 37 °C in an ascending time course. As a control one non-induced and one induced P6 dish without cycloheximide were first harvested and lysed in urea buffer (t=0) according to 2.9.5. For analysis of the protein turnover, cells were harvested after 30 minutes, 1, 1.5, 2, 4, 8, 12, 14, and 24 hours. Finally, the protein mass concentration of urea lysates was determined, the protein amount further analyzed and quantified by means of western blotting, as mentioned in chapters 2.5.1 and 2.5.3.

2.9.7 Analysis of the degradation pathway of LMX1B protein

After determination of protein half-lives of LMX1B and its counterpart mutants, different degradation pathways in addition to protein synthesis were blocked. In separate experiments, the protein degradation was blocked by incubating the cells with different proteasomal inhibitors such as MG-132 [10 µM] or Bortezomib [PS-341, 10 µM] or by the lysosomal inhibitor Bafilomycin A_1 [Baf A_1, 10 µM] along with the cycloheximide [100 µg/mL] as noted in 2.9.6. Briefly, LMX1B protein expression was induced for 6 days according to 2.9.3. One day prior to experiments, cells were split from 2-3 P10 dishes, pooled and resuspended in 5.5 mL of respective medium. Subsequently, 500 µL of cell suspension was seeded in 5 separate P6 dishes and cultivated overnight at 37 °C, respectively. On day 6 of LMX1B induction, the cycloheximide stock with 10 mg/mL in sterile water was diluted in respective medium at the working concentration of 100 µg/mL. All stocks, MG-132 [10 mM], PS-341 [10 mM] and Baf-A_1 [10 mM] were dissolved in DMSO and diluted in respective medium at the final concentration of 10 µM, respectively. The medium in P6 dishes was removed and medium containing cycloheximide [100 µg/mL] in addition to MG-132 [10 µM] or PS-341 [10 µM] or Baf-A_1 [10 µM] or DMSO [10 µM] was pipetted into respective dish. Cells were incubated for 4 or 8 hours at 37 °C. As a control, one non-induced and one induced P6 dish without inhibitors were first harvested and lysed in urea buffer (t=0) according to 2.9.5. Finally, cells were harvested after 4 and 8 hours of inhibitor and solvent incubation, lysed in urea buffer and further processed for western blotting.

3. Results

The zinc finger motifs in the LIM domains of LMX1B are responsible for the interaction with other proteins. Amino acid substitutions affecting the zinc-coordinating residues of LMX1B have been made responsible for the development of nail-patella syndrome. In order to investigate the effect of such missense mutations and to understand the molecular mechanism of disease progression, *Lmx1b* knock-in mice were generated (Burghardt *et al.*, unpublished). In the following chapters, the results of the present study are outlined giving new insights on mutations in *LMX1B*, which are responsible for nail-patella syndrome.

3.1 *Lmx1b* knock-in mice

Previously, *Lmx1b* knock-in mice were generated with point mutations either in exon 2 of *Lmx1b* encoding the LIM 1, Figure 3.1, [A] or in exon 3 encoding the LIM 2 domain, Figure 3.1 [B] (Burghardt *et al.*, unpublished). The corresponding mutant proteins, Lmx1b (H54L) and Lmx1b (C95F), numbering was used according to the reference sequence of *LMX1B*/*Lmx1b* referred to NCBI RefSeq.: NM_002316.2, NP_002307.1 transcript variant 1 in human and to NCBI RefSeq.: NM_010725.3, NP_034855.3 in mice. These mutant proteins have been described in patients with nail-patella syndrome as disease-causing variants of LMX1B (Dunston *et al.* 2005).

[A] *Lmx1b* (H54L)

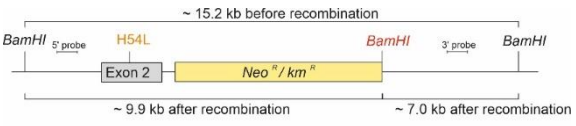

[B] *Lmx1b* (C95F)

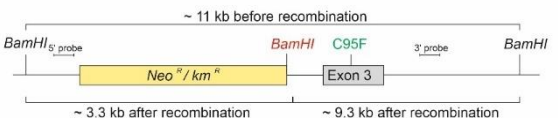

Figure 3.1: Targeting constructs of *Lmx1b* knock-in mice (Burghardt et. al, unpublished). [A] Targeting construct *Lmx1b* (H54L). Exon 2 contains the desired mutation encoding for p.H54L, the neomycin resistance gene flanked by frt-sites was introduced into intron 2. **[B]** Targeting construct *Lmx1b* (C95F). Exon 3 comprises the desired mutation encoding for p.C95F, the *frt*-flanked neomycin gene was introduced in intron 2.

3.1.1 Genotyping of *Lmx1b* knock-in mice

For successful genotype assessment of *Lmx1b* knock-in mice, primer for genotyping were designed flanking the neomycin resistance cassette. After deletion of the neomycin cassette by crossbreeding of the F1 generation with FLP-deleter mice, recombination leads to a cut out of the neomycin resistance cassette whereas an *frt*-site remains within the genomic sequence. If mice harbor the mutated *Lmx1b* (H54L) knock-in allele, the PCR amplicon with 585 bp resulted in a 92 bp higher product due to the remaining *frt*-sites after the FLP-recombination compared to the wild-type *Lmx1b* PCR product with 493 bp. In the case for mice with the mutated *Lmx1b* (C95F) knock-in gene, the PCR amplicon with 526 bp demonstrated a 98 bp higher product compared to the wild-type *Lmx1b* PCR product with 428 bp (Figure 3.2).

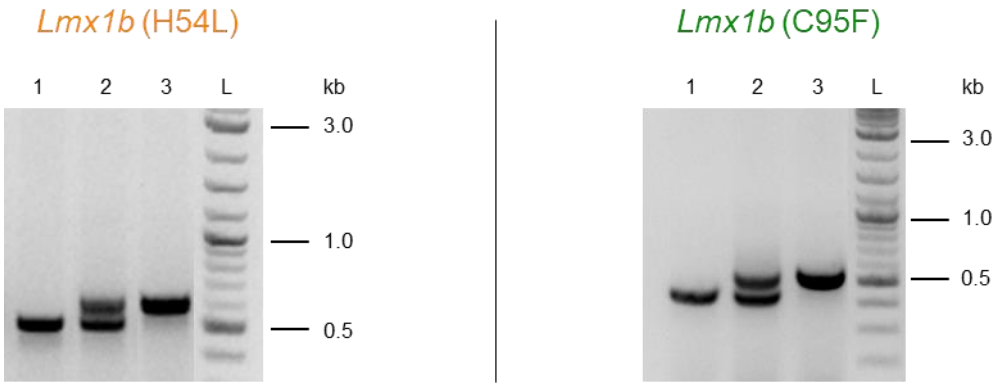

Figure 3.2: Genotyping of *Lmx1b* (H54L) and *Lmx1b* (C95F) mice.
Isolated genomic DNA from tail cuts of *Lmx1b* (H54L) and *Lmx1b* (C95F) mice was analyzed by PCR with primers listed in 2.1.6. The PCR product of the *Lmx1b* (H54L) transgene had a size of 585 bp and 493 bp for wild- type. PCR of *Lmx1b* (C95F) showed a size of 526 bp for the transgene and 428 bp for the wild- type mice. Lane 1: *Lmx1b* $^{+/+}$ wild-type, Lane 2: heterozygous *Lmx1b* $^{+/H54L}$ or *Lmx1b* $^{+/C95F}$, Lane 3: homozygous *Lmx1b* $^{H54L/H54L}$ or *Lmx1b* $^{C95F/C95F}$ mice. L, 1- kb DNA ladder (NEB).

3.1.2 Verification of *Lmx1b* knock-in mRNA in E18.5 kidneys

After evidence of the *Lmx1b* knock-in on genomic DNA level by Southern blot and PCR, performed by Tillmann Burghardt, the expression of the wild-type and mutant mRNA was confirmed by total RNA preparations from E18.5 *Lmx1b* knock-in kidneys. Total RNA was reversely transcribed into cDNA followed by a PCR reaction for further analyzing the successful knock-in sites. PCR products with a size of 959 bp were digested with respective restriction enzymes, due to the accompanied insertion of a *XhoI* site in case of the H54L knock-in and a *BspEI* site for the C95F knock-in. On an agarose gel, digested *Lmx1b* (H54L) mutant samples showed a product size of 811 bp (Figure 3.3, [A]) and *Lmx1b* (C95F) mutants a size of 694 bp (Figure 3.3, [B]). In addition, undigested bands were cut out of the agarose gel, purified using a gel extraction kit and sequenced by the company Microsynth Seqlab GmbH. Sequencing results of the undigested PCR products additionally approved the identity and expression of the desired mutations encoding: Lmx1b (H54L), Figure 3.3, [A] and Lmx1b (C95F), Figure 3.3, [B].

[A]

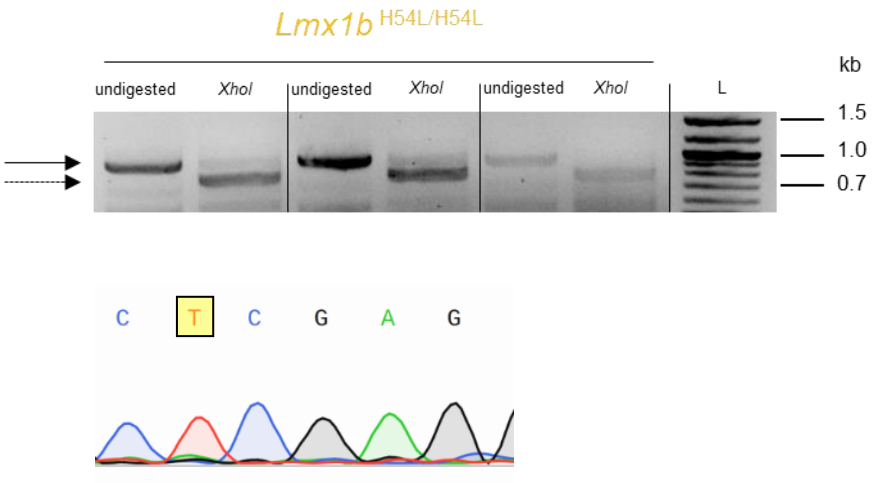

H54L:

CAC GAG → CTC GAG

→ *XhoI*

[B]

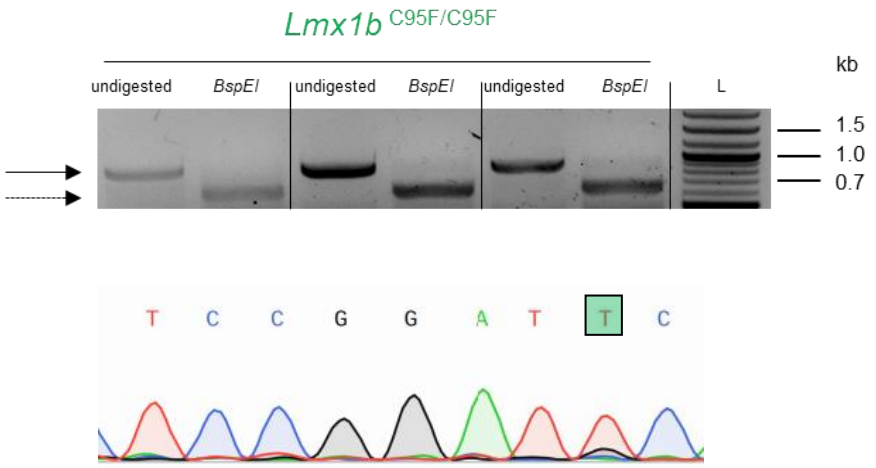

C95F:

AGC GGC TGC → TCC GGA TTC

→ *BspEI*

Figure 3.3: Verification of *Lmx1b* knock-in on transcriptional level.
To identify the desired mutations on mRNA level, total RNA was extracted from 3 homozygous E18.5 *Lmx1b* knock-in (H54L or C95F) mice. cDNA was reversely transcribed and *Lmx1b* was amplified using oligonucleotides listed in 2.1.6. Thereafter, PCR products were analyzed by agarose gel electrophoresis and specific band with sizes of 959 bp were isolated and purified using a gel extraction kit. Samples were sequenced by the company Microsynth Seqlab GmbH and chromatograms were created. Desired mutations were successfully identified on transcriptional level: **[A]** For the *Lmx1b* (H54L) (c.161A>T; p.H54L) and **[B]** the *Lmx1b* (C95F) (c.277-285 [AGCGGCTGC> TCCGGATTC]; p.C95F).

3.1.3 Phenotype of *Lmx1b* knock-in mice

After successful verification of the *Lmx1b* knock-in on the genomic level, the phenotype was systematically analyzed. Due to perinatal lethality of homozygous *Lmx1b* knock-in animals, all analyses were performed on day E18.5.

3.1.3.1 Kidney phenotype of *Lmx1b* knock-in mice

The prognosis of some nail-patella syndrome patients is determined by a characteristic nephropathy, which is caused by a malfunction of the podocytes. Therefore, at first the kidney phenotypes of *Lmx1b* knock-in mice were analyzed. In addition to the kidney histology, the ultrastructure of the filtration barrier was examined.

Histology

Analysis of 6 µm *Lmx1b* knock-in and control kidney sections by hematoxylin / eosin staining on the light microscopic level revealed differences in the kidney morphology Figure 3.4. Whereas heterozygous *Lmx1b* knock-in animals (*Lmx1b* $^{+/H54L}$ or *Lmx1b* $^{+/C95F}$), Figure 3.4, C, D and J, K, demonstrated no obvious phenotype and appeared similarly to the wild-type (*Lmx1b* $^{+/+}$), Figure 3.4, A, H, and heterozygous *Lmx1b* knock-out animals (*Lmx1b* $^{+/-}$), Figure 3.4, B,I, homozygous *Lmx1b* knock-in mice (*Lmx1b* $^{H54L/H54L}$ or *Lmx1b* $^{C95F/C95F}$), Figure 3.4, F, M and G, N developed an abnormal accumulation of eosinophilic materials in the convoluted tubules consistent with the homozygous *Lmx1b* knock-out mice (*Lmx1b* $^{-/-}$), Figure 3.4, E, L. In addition, the glomerular morphology appeared abnormal showing cuboidal podocytes that remain on top of the capillaries, not spreading out over the glomerular basement membrane. Furthermore, some of the renal corpuscles of homozygous *Lmx1b* knock-in mice displayed an abnormal arrangement accompanied by an enlarged bowman´s space in addition to a rudimentary glomerulus as seen in Figure 3.4, M and N. All in all, kidneys of *Lmx1b* knock-in mice resemble the picture of the *Lmx1b* knock-out mice.

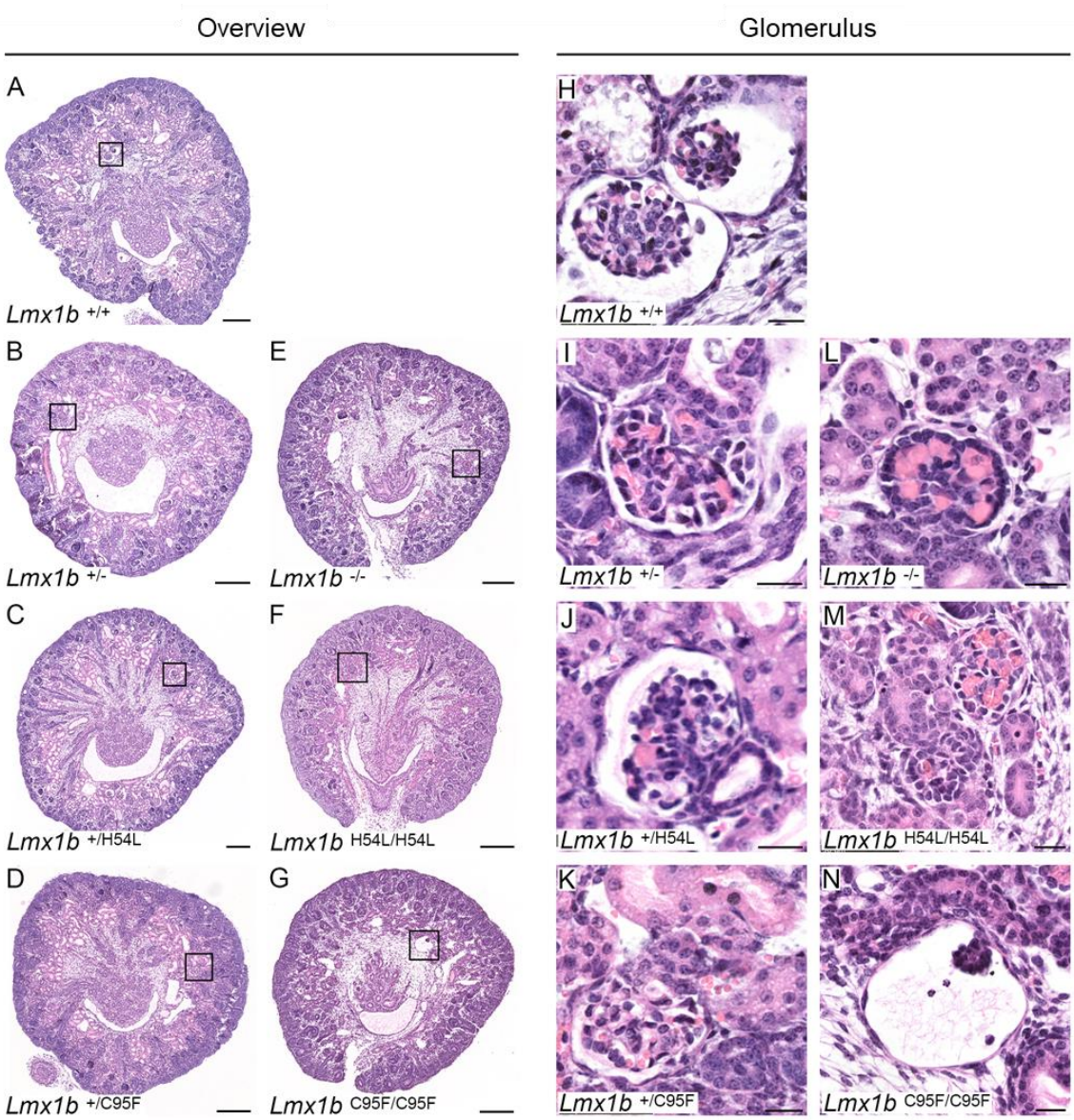

Figure 3.4: Hematoxylin / eosin staining of 6 µm paraffin sections from kidneys of E18.5 *Lmx1b* wild-type, knock-in, and knock-out mice.
Boxes highlight the 40x magnified juxtamedullary glomeruli pictured in the right panels. Illustrated are representative stainings of control mice **[A, B, E and H, I, J]**, heterozygous *Lmx1b* knock-in mice **[C, D and J, K]**, and homozygous *Lmx1b* knock-in mice **[F, G, and M, N]**.

Ultrastructure

On the ultrastructural level, *Lmx1b* knock-in mice were additionally analyzed compared to *Lmx1b* wild-type and *Lmx1b* knock-out control mice (Figure 3.5). Kidney sections were further examined by electron microscopy to investigate glomerular ultrastructure and podocyte foot process effacement. Electron micrographs revealed a consisting picture as described in the histology chapter. Control and wild-type mice showed a regular glomerular filtration barrier including the fenestrated endothelium, the glomerular basement membrane and delicate podocyte foot processes (Figure 3.5, A, B). Heterozygous *Lmx1b* knock-in animals (Figure 3.5, C, D) looked like *Lmx1b* wild-type and heterozygous *Lmx1b* knock-out mice (Figure 3.5, A, B). Apart from that, as expected, prominent structural abnormalities could be detected in homozygous *Lmx1b* knock-in mice (Figure 3.5, F, G) similar to the homozygous Lmx1b knock-out mice (Figure 3.5, E). Those animals demonstrated markedly broadened foot processes accompanied by a loss of filtration slits. Filtration slits per µm glomerular basement membrane were quantified (Figure 3.6) confirming the electron microscopic data as shown in Figure 3.5.

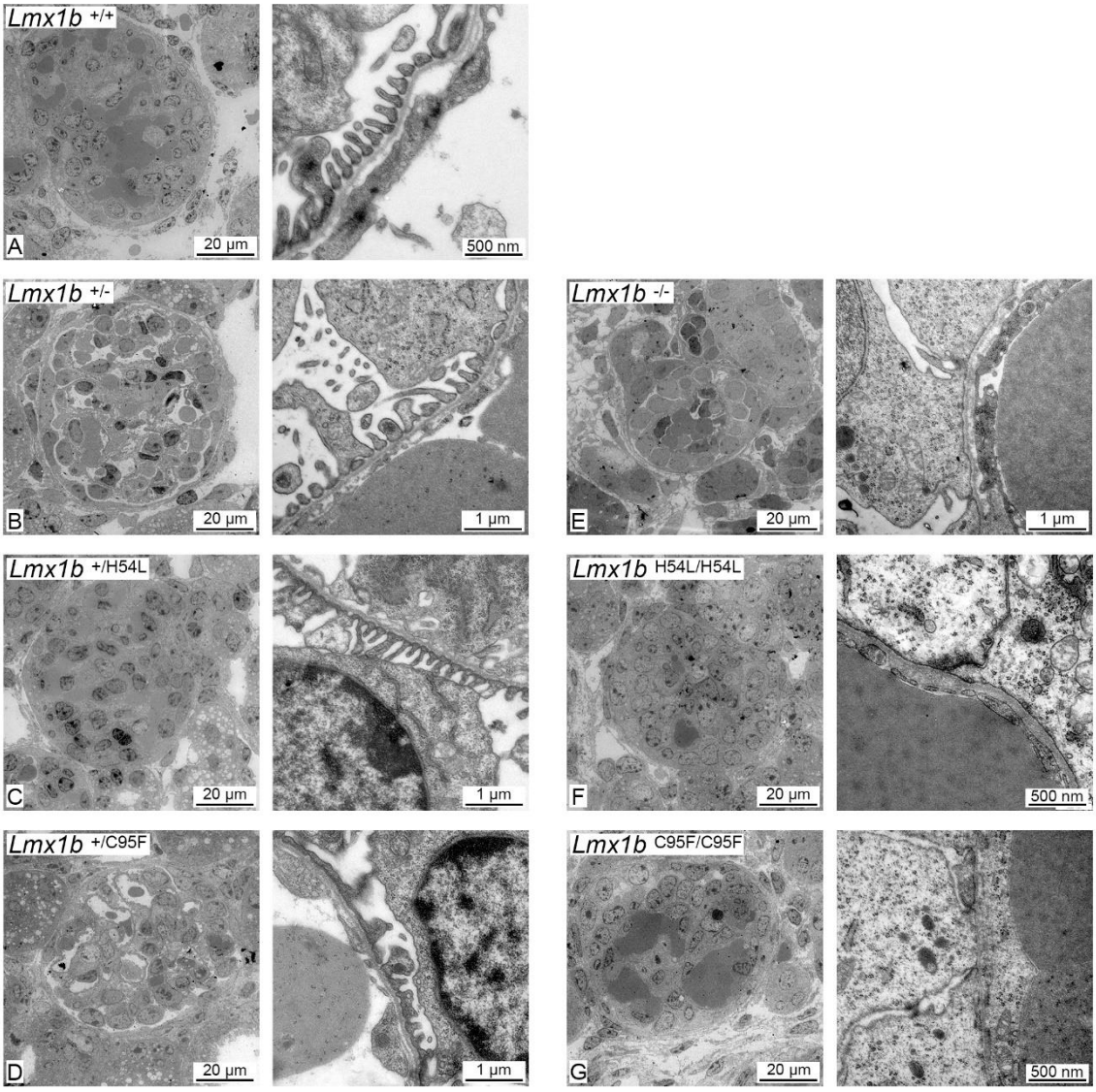

Figure 3.5: Transmission electron micrographs of a juxtamedullary glomerulus of E18.5 *Lmx1b* knock-in and knock-out mice.
Representative micrographs from **[A]** *Lmx1b* wild-type (*Lmx1b* $^{+/+}$, n = 5), **[B]** heterozygous *Lmx1b* knock-out (*Lmx1b* $^{+/-}$, n = 2), **[C]** heterozygous *Lmx1b* (H54L) (*Lmx1b* $^{+/H54L}$, n = 5) and **[D]** *Lmx1b* (C95F) (*Lmx1b* $^{+/C95F}$, n = 4) knock-in mice showed no renal abnormalities. **[E]** Homozygous *Lmx1b* knock-out (*Lmx1b* $^{-/-}$, n = 2), **[F]** homozygous *Lmx1b* (H54L) (*Lmx1b* $^{H54L/H54L}$, n = 5), and **[G]** homozygous *Lmx1b* (C95F) (*Lmx1b* $^{C95F/C95F}$, n = 5) knock-in mice demonstrated cuboidal shaped podocytes in the juxtamedullary glomeruli and on ultrastructural level a prominent foot process effacement. Magnification of electron micrographs of respective genotype: left panels, 700x; right panels, 20 000x.

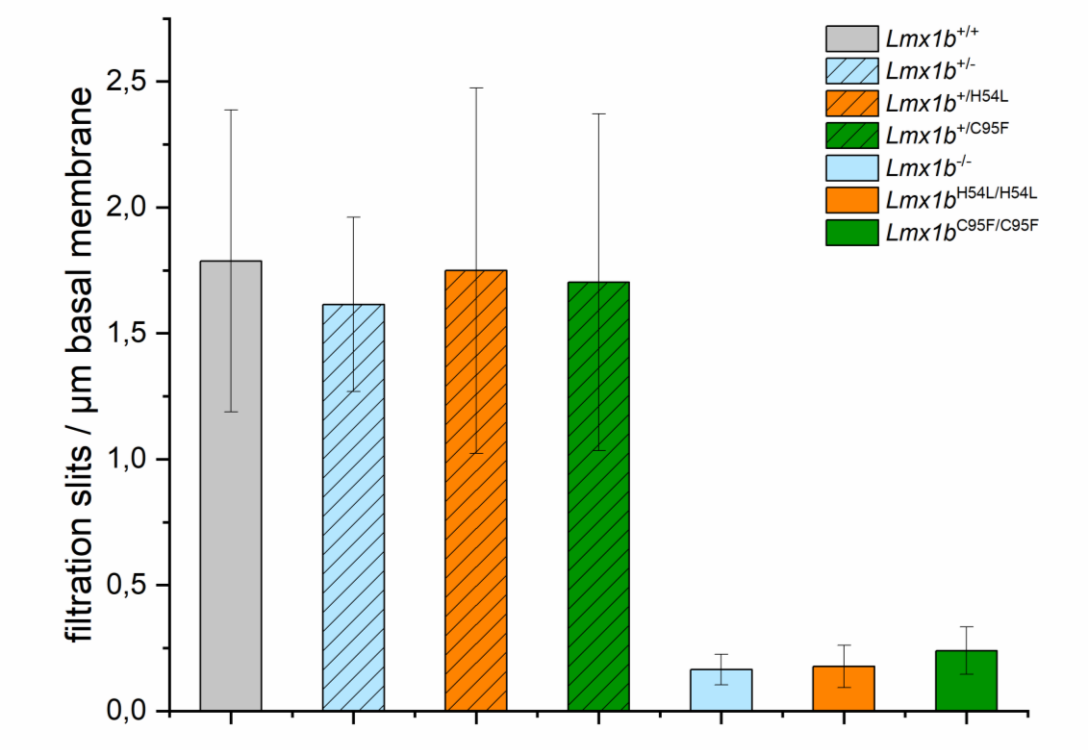

Figure 3.6: Quantification of filtration slits per micrometer basement membrane of E18.5 *Lmx1b* knock-in and *Lmx1b* knock-out mice.
To quantify the frequency of filtration slits, blinded 7,000x magnified electron micrographs were examined. The length of the basement membrane was measured using the software ImageJ. The gaps between podocyte foot processes were counted to calculate the number of filtration slits/µm. *Lmx1b* wild-type (*Lmx1b* $^{+/+}$, n = 5); heterozygous *Lmx1b* knock-out (*Lmx1b* $^{+/-}$, n = 2); heterozygous *Lmx1b* H54L (*Lmx1b* $^{+/H54L}$, n = 5); heterozygous *Lmx1b* C95F (*Lmx1b* $^{+/C95F}$, n = 4); homozygous *Lmx1b* knock-out (*Lmx1b* $^{-/-}$, n = 2); homozygous *Lmx1b* H54L (*Lmx1b* $^{H54L/H54L}$, n = 4); homozygous *Lmx1b* C95F (*Lmx1b* $^{C95F/C95F}$, n = 5). Data are presented as mean ± standard deviation.

3.1.3.2 Forelimb morphology of E18.5 *Lmx1b* knock-in mice

The forelimb morphology of E18.5 *Lmx1b* knock-in mice showed an obvious phenotype similar to the *Lmx1b* knock-out mice described in the literature (Chen *et al.* 1998a). The wild-type (*Lmx1b* $^{+/+}$) dorsal limb surface (Figure 3.7, A) exhibited small hair follicles and the ventral surface showed prominent bulges corresponding to developing footpads apparent in the palmar region (Figure 3.7, B). Homozygous *Lmx1b* knock-in (*Lmx1b* $^{H54L/H54L}$ and *Lmx1b* $^{C95F/C95F}$) limbs lack dorsal hair follicles (Figure 3.7, D, G) that were replaced by ectopic foot pads in the same number and arrangement as the ventral surface. Remarkably, homozygous *Lmx1b* knock-in mice demonstrated a strong bend of fore-paws (Figure 3.7, E, H). In addition, the characteristic ventral flexure of wild-type digits (Figure 3.7, C) was missing in homozygous mutant limbs (Figure 3.7, F, I).

Figure 3.7: Forelimb morphology of E18.5 *Lmx1b* knock-in mice.
Photographs show forelimbs of E18.5 wild-type (*Lmx1b* $^{+/+}$) and homozygous *Lmx1b* knock-in (*Lmx1b* $^{H54L/H54L}$ and *Lmx1b* $^{C95F/C95F}$) mice. **[A, D, G]** depict dorsal views; **[B, E, H]** demonstrate ventral views, and **[C, F, I]** anterior views. Dorsal features (hair follicles) were lost in mutants and replaced by ventral features, such as foot pads. In addition, the characteristic ventral flexure of digits was absent in mutants [F, I] compared to wild-type mice [C].

3.1.3.3 Skull phenotype of *Lmx1b* knock-in mice

Whole mount E18.5 *Lmx1b* knock-in animals were scanned using µCT 'phoenix v|tome|xs 240/180 research edition' system (Figure 3.8, [A] and [B]). µCT scans of the skull from wild-type (*Lmx1b* $^{+/+}$), heterozygous *Lmx1b* knock-out (*Lmx1b* $^{+/-}$) and *Lmx1b* knock-in (*Lmx1b* $^{+/H54L}$ or *Lmx1b* $^{+/C95F}$) as well as homozygous *Lmx1b* knock-out (*Lmx1b* $^{-/-}$) and *Lmx1b* knock-in mice (*Lmx1b* $^{H54L/H54L}$ or *Lmx1b* $^{C95F/C95F}$) were analyzed. Heterozygous *Lmx1b* knock-in mice did not display differences in ossification of the skull, thus appearing the same as *Lmx1b* wild-type mice. In contrast, the skulls of homozygous *Lmx1b* knock-in mice (*Lmx1b* $^{H54L/H54L}$ or *Lmx1b* $^{C95F/C95F}$) exhibited various calvaria-specific defects coincident with the homozygous *Lmx1b* knock-out (*Lmx1b* $^{-/-}$) mice. The supraoccipital and interparietal bones were either missing or severely reduced and the sutures between the frontal, parietal, and interparietal bones were anomalous showing a premature ossification (Figure 3.8, [A] and [B]). A number of six individuals per genotype was analyzed and confirmed the appearance of the calvaria abnormalities merely in homozygous *Lmx1b* knock-in (*Lmx1b* $^{H54L/H54L}$ or *Lmx1b* $^{C95F/C95F}$) mice.

[A]

Lmx1b $^{+/+}$

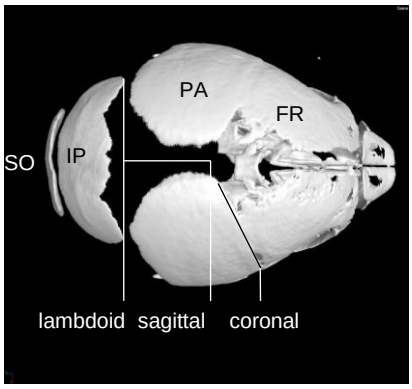

Lmx1b $^{+/-}$

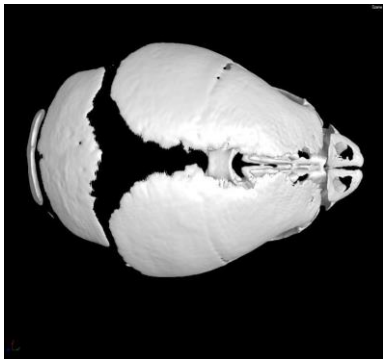

Lmx1b $^{+/H54L}$

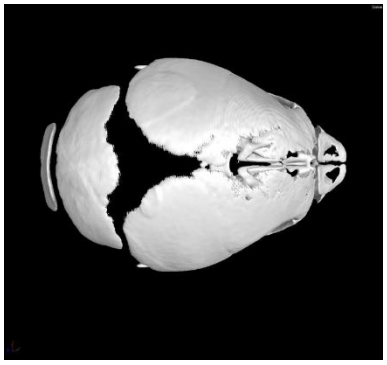

Lmx1b $^{+/C95F}$

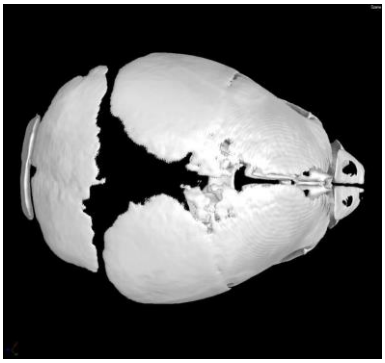

Lmx1b $^{-/-}$

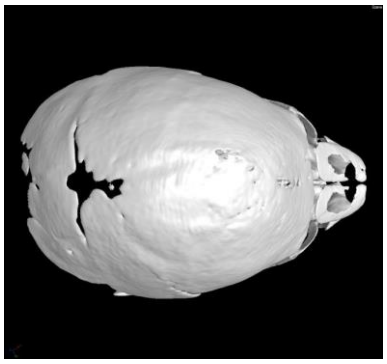

Lmx1b $^{H54L/H54L}$

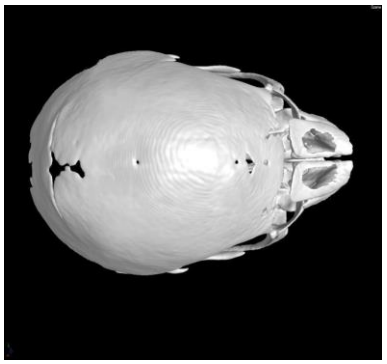

Lmx1b $^{C95F/C95F}$

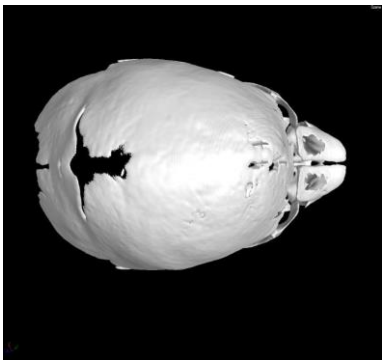

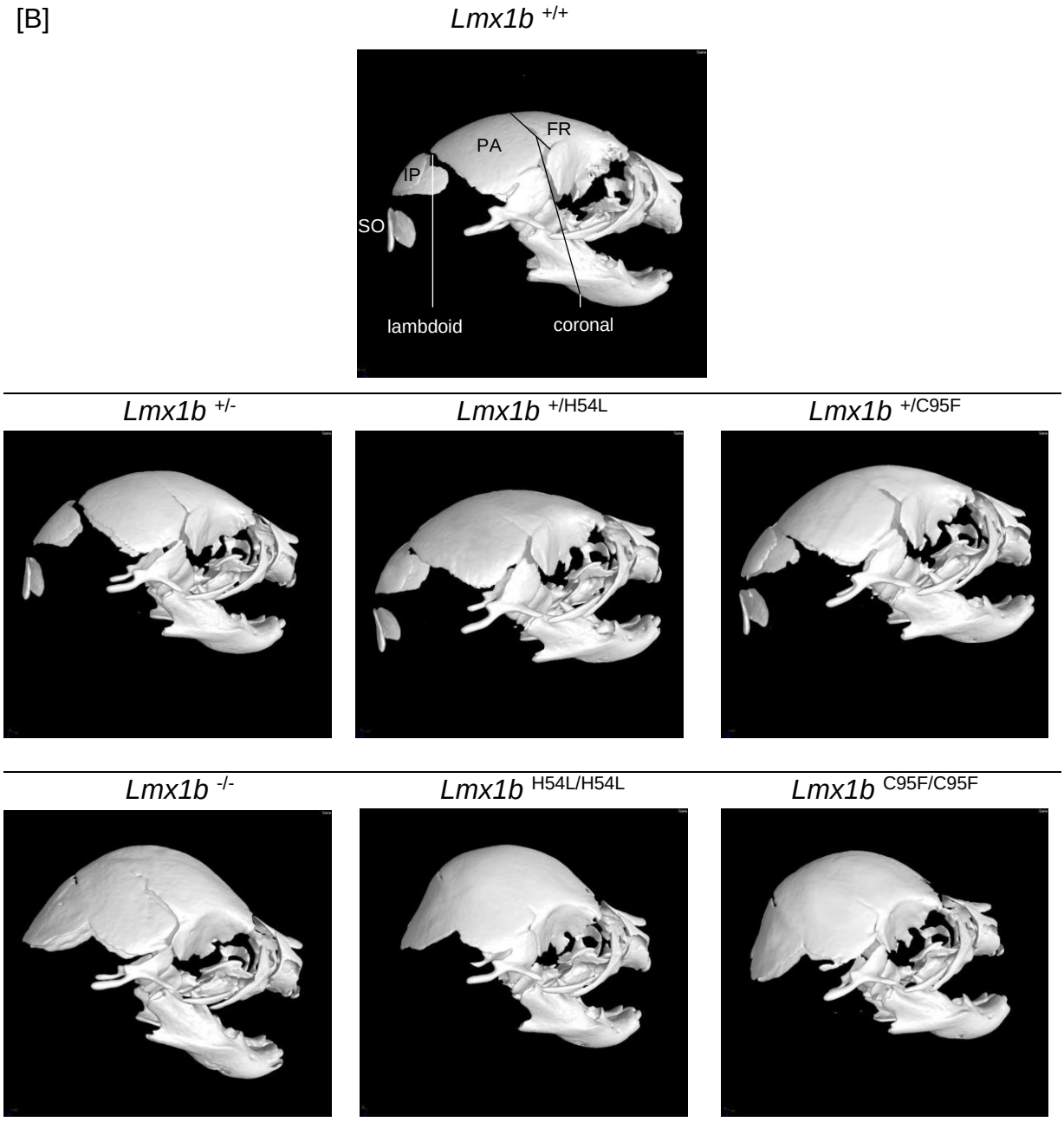

Figure 3.8: µCT scans of the skull of E18.5 *Lmx1b* knock-out and *Lmx1b* knock-in mice.
[A] Panels show the cranial and **[B]** the lateral view of the skull. In the *Lmx1b* knock-in mice, the abnormal interparietal and absent supraoccipital bones were depicted. The lambdoid, coronal, and metopic sutures appeared completely ossified. Genotypes as indicated. *Abbreviations*: FR, frontal; IP, interparietal; PA, parietal; SO, supraoccipital. µCT scans were obtained applying a voxel size of 30-32 µm. Magnification 6.5x; images: 1,000; time: 500 ms; voltage: 23 kV; current intensity: 600 µA; scan period: 8 minutes.

3.1.3.4 Skeletal phenotype of *Lmx1b* knock-in mice

The skeletal phenotype of *Lmx1b* knock-in mice was determined by a specific staining (Figure 3.9). Cartilages were stained by Alcian blue and bones were marked by Alizarin red. Examination of skeletal preparations of E18.5 mice revealed defects in homozygous *Lmx1b* mutants, such as *Lmx1b* $^{-/-}$, *Lmx1b* $^{H54L/H54L}$ and *Lmx1b* $^{C95F/C95F}$, Figure 3.9, [E], [F] and [G]. In forelimbs, the distal ulna was reduced or absent (n = 20, from 10 animals) and the scapula was smaller relative to that of wild-type animals and heterozygous *Lmx1b* mutants, Figure 3.9, [A], [B], [C] and [D]. The clavicle was also abnormally bent projecting along the surface of the scapula instead of away from it. The hindlimbs were similarly affected, showing defects especially in the iliac region of the pelvis. Unlike the ulna, the fibula was not significantly reduced or absent in length. Mutant *Lmx1b* knock-in mice were additionally lacking the patellae similar to *Lmx1b* knock-out mice (n = 10), Figure 3.9.

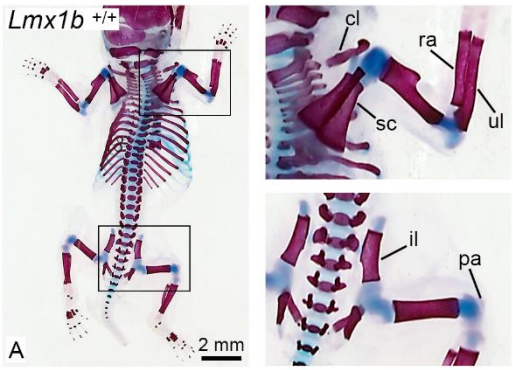
Lmx1b +/+
cl
ra
sc
ul
il
pa
2 mm
A

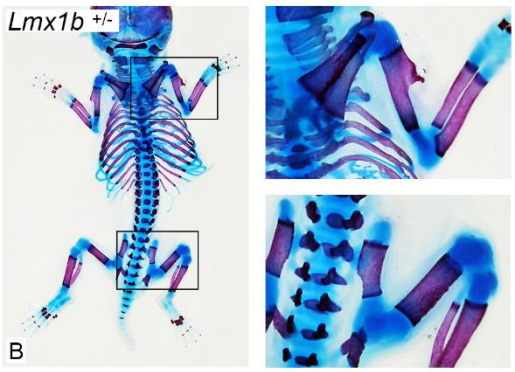
Lmx1b +/-
B

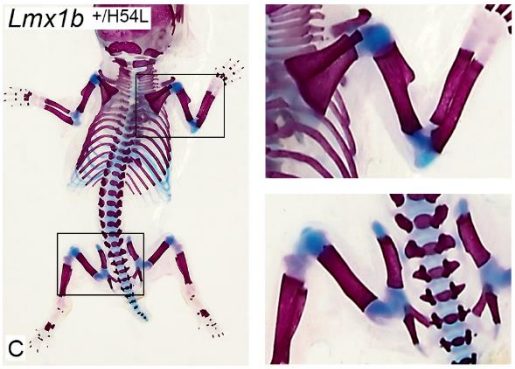
Lmx1b +/H54L
C

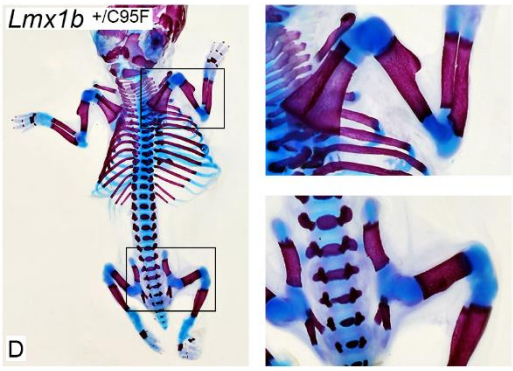
Lmx1b +/C95F
D

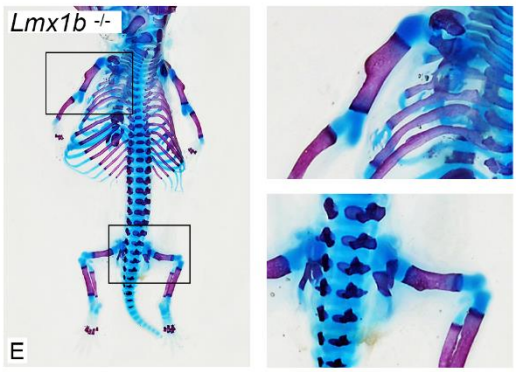
Lmx1b -/-
E

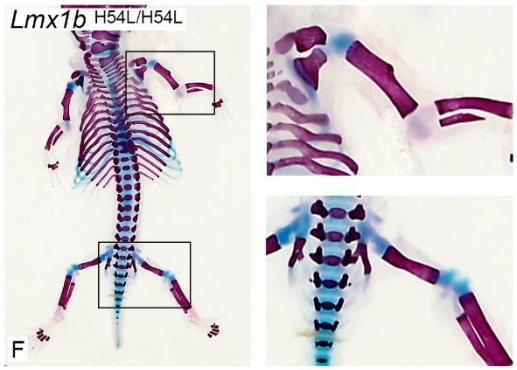
Lmx1b H54L/H54L
F


Lmx1b C95F/C95F
G

Figure 3.9: Skeletal staining with Alizarin red and Alcian blue of E18.5 *Lmx1b* knock-out and knock-in mice.
[A] Wild-type (*Lmx1b* $^{+/+}$), **[B]** heterozygous *Lmx1b* knock-out (*Lmx1b* $^{+/-}$), and **[C, D]** heterozygous *Lmx1b* knock-in mice (*Lmx1b* $^{+/H54L}$ or *Lmx1b* $^{+/C95F}$) showed normally developed forelimbs and hindlimbs. **[E]** Homozygous *Lmx1b* knock-out (*Lmx1b* $^{-/-}$), and **[F, G]** homozygous *Lmx1b* knock-in mice (*Lmx1b* $^{H54L/H54L}$ or *Lmx1b* $^{C95F/C95F}$) showed defects in the skeleton. In forelimbs, the ulnae were partially absent, the scapulae appeared smaller and the claviculae were bent. Hindlimbs of homozygous mutants were additionally affected. The patellae were absent, and mice showed defects in the iliac region of the pelvis. *Abbreviations:* cl, clavicula; sc, scapula; ul, ulna; ra, radius; il, ilium; pa, patella.

3.1.4 Lmx1b mRNA level of E18.5 *Lmx1b* knock-in mice

To confirm the expression of wild-type and mutant mRNA, quantitative PCR reactions were carried out with total RNA preparations from E18.5 kidneys (Figure 3.10). It turned out that the mRNA levels of homozygous *Lmx1b* (H54L) and *Lmx1b* (C95F) E18.5 kidneys are not decreased compared to *Lmx1b* wild-type mRNA levels. Mice were backcrossed onto a C57BL/6 background for ten generations, thus ensuring that introduction of the mutations had no negative effect on the transcription of the *Lmx1b* gene. In light of the fact, that quantitative PCR analysis revealed comparable Lmx1b mRNA levels of homozygous knock-in and wild-type mice, the successful expression of mutated *Lmx1b* transcript was confirmed. Figure 3.10 shows relative Lmx1b mRNA levels normalized to the housekeeper ribosomal protein S9 (Rps9) mRNA.

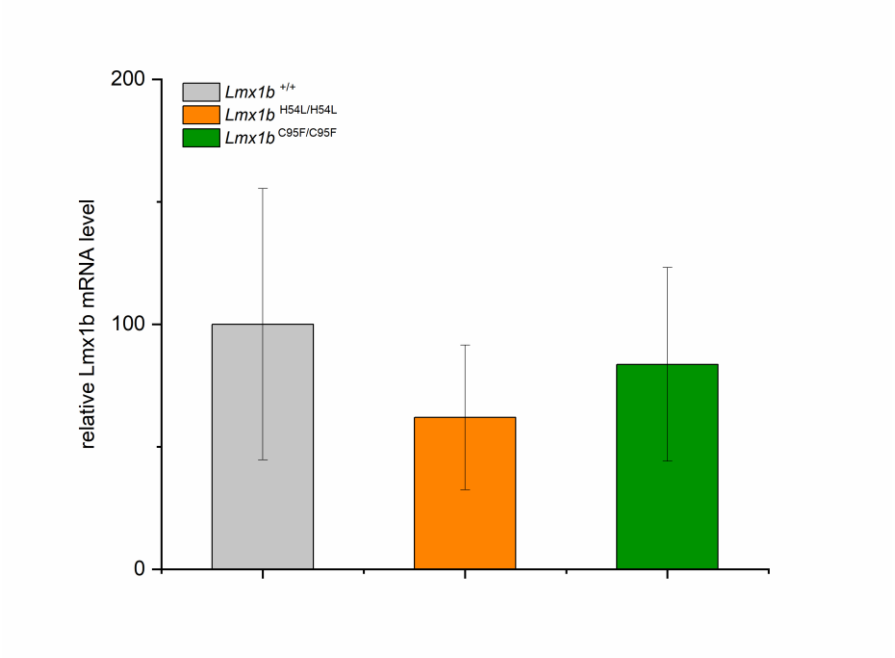

Figure 3.10: Quantitative PCR analysis of Lmx1b mRNA from E18.5 kidneys of *Lmx1b* wild-type, *Lmx1b* (H54L), and *Lmx1b* (C95F) mice.
Total RNA was isolated from E18.5 kidneys of *Lmx1b* wild-type and homozygous *Lmx1b* knock-in mice and reversely transcribed into cDNA. Thereafter Lmx1b levels were analyzed by quantitative PCR. Lmx1b mRNA levels of *Lmx1b* (H54L) (*Lmx1b* $^{H54L/H54L}$, n = 3) and *Lmx1b* (C95F) (*Lmx1b* $^{C95F/C95F}$, n = 3) mutants were normalized to Rps9 mRNA and were not decreased compared to *Lmx1b* wild-type (*Lmx1b* $^{+/+}$, n = 3) mice. Data are presented as mean values ± standard deviation.

3.1.5 Lmx1b protein screening in E18.5 *Lmx1b* knock-in kidneys

To confirm Lmx1b on the protein level, E18.5 kidney sections of *Lmx1b* wild-type and homozygous *Lmx1b* knock-out and *Lmx1b* knock-in mice were stained by immunofluorescence against Lmx1b, shown in Figure 3.11. A positive Lmx1b signal could solely be detected in *Lmx1b* wild-type mice. Homozygous *Lmx1b* knock-in mice resembled the picture of the homozygous *Lmx1b* knock-out. On the protein level, Lmx1b was not detectable in homozygous mutant mice.

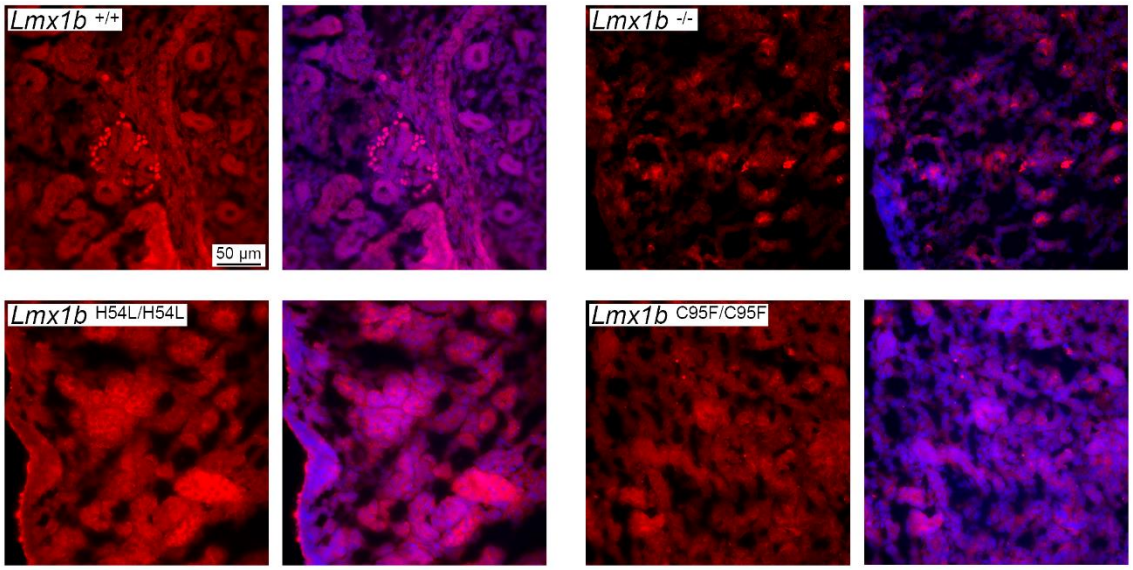

Figure 3.11: Immunofluorescence staining against Lmx1b of cryo-embedded E18.5 kidney sections.
Mice embryos were sacrificed on day E18.5 and kidneys were immediately shock-frozen in the gas phase above liquid nitrogen. Lmx1b staining was visualized in the red channel, nuclear staining was depicted in blue. A representative glomerulus of *Lmx1b* wild-type mice (*Lmx1b* $^{+/+}$, n = 3) showed a specific staining for Lmx1b. In homozygous *Lmx1b* (H54L, *Lmx1b* $^{H54L/H54L}$, n = 3), *Lmx1b* (C95F, *Lmx1b* $^{C95F/C95F}$, n = 3) and *Lmx1b* knock-out (*Lmx1b* $^{-/-}$, n = 3) individuals, a specific Lmx1b signal was not detectable.

3.2 LMX1B (H54L) and (C95F) protein stability

Since the expression of mutant *Lmx1b* knock-in proteins could not be detected *in vivo*, the mutant proteins LMX1B (H54L) and LMX1B (C95F) were further analyzed on the molecular level by *in vitro* experiments in cell culture. A possible protein degradation of mutated Lmx1b could not be excluded, since amino acid substitutions often lead to conformational changes of protein structure resulting in misfolding events. Therefore, it was the aim to further examine the protein stability of LMX1B in cell culture to draw potential conclusion to the picture of Lmx1b knock- in mice.

3.2.1 Generation of inducible stably transfected cell lines

As previously described by (Cross *et al.* 2014), the mutation LMX1B (V242D) showed a dominant-negative effect in mice, also see chapter 1.5.4. Heterozygous mutant mice showed glaucomatous eye defects and were semi-lethal, probably due to kidney failure. In this context, the properties of the mutant protein LMX1B (V242D) was additionally analyzed more precisely *in vitro* because *Lmx1b* knock-in mice did not reflect these phenotypes. To elucidate half-life experiments, stably transfected HtTA-1 cells with an inducible LMX1B construct were generated. HtTA- 1/myc- LMX1B (WT) and HtTA-1/myc-LMX1B (C95F) cell lines had been generated in the lab for a previous study (Rascle *et al.* 2009). The other cell lines, HtTA-1/myc-LMX1B (H54L) and HtTA-1/myc-LMX1B (V242D) were established for this thesis according to the cell lines that were designed by Anne Rascle (Rascle *et al.* 2009). LMX1B was under control of the *tetO* promoter and repressed in the presence of doxycycline. Protein expression of LMX1B was induced by the absence of doxycycline in the medium for at least 4 days. Testing for positive clones was carried out by western blot. Compared to the induced LMX1B (WT) expression of the already existing control clone 34 LMX1B (WT), several positive clones were detected for LMX1B (H54L) as well as LMX1B (V242D), Figure 3.12, [A] and [B]. Further *in vitro* experiments were performed with clone 141 for

HtTA- 1/myc- LMX1B (H54L) cells and in case of HtTA-1/myc-LMX1B (V242D) clone 90 was chosen.

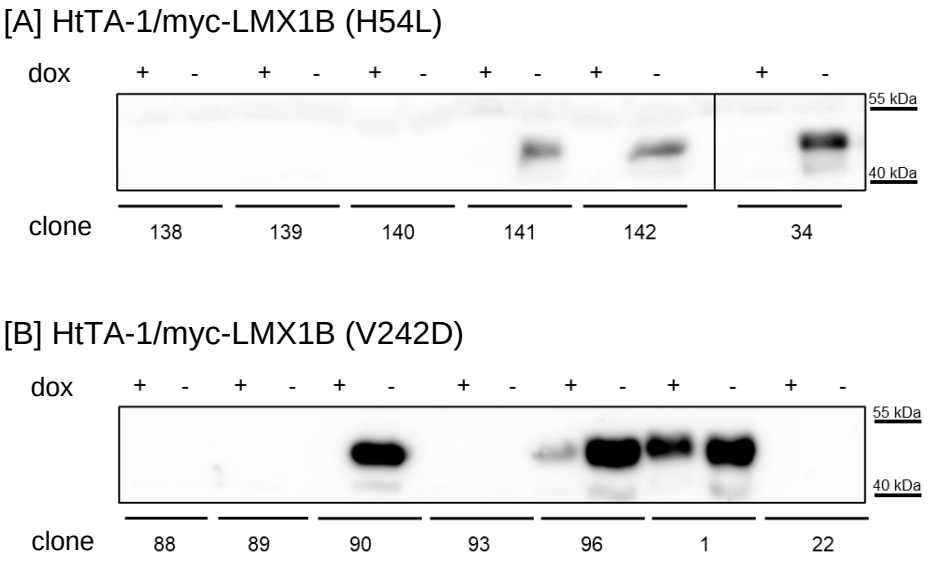

Figure 3.12: Screening of positive stably transfected clones by induction of LMX1B protein expression.
For verification of positive clones, after transfection cells were selected by puromycin and resistant clones were split in two P6 dishes, one with doxycycline- free medium and as a control one with doxycycline-containing medium. After 4 days of incubation, cells were harvested, lysed, and analyzed by western blot. Whole cell protein lysates (40 µg) were loaded, respectively. Myc- LMX1B showed a molecular weight at 46 kDa. **[A]** Cell line HtTA- 1/myc- LMX1B (H54L) showed two positive clones, 141 and 142, that demonstrated an induced LMX1B (H54L) expression compared to the control 34 LMX1B (WT). **[B]** For the cell line HtTA-1/myc-LMX1B (V242D), clone 90 showed a strong LMX1B (V242D) expression after 4 days. LMX1B (V242D) induction of clone 96 and 1 was not successful since LMX1B (V242D) was also expressed when doxycycline was present. *Abbreviations*: +, doxycycline containing cell lysate; -, doxycycline-free cell lysate.

3.2.2 Optimal expression levels of different LMX1B proteins (WT, H54L, C95F, and V242D)

To determine the optimal LMX1B expression levels of the different LMX1B proteins (WT, H54L, C95F, and V242D), an induction series of their expression was carried out in stably transfected cell lines. Cells were incubated for 0, 1, 3, 5, 6, or 7 days in doxycycline-free medium. For all different cell clones, the LMX1B expression level started to rise on day 1. Western blot analysis was accompanied by immunofluorescence staining showing intensifying signals from day 3 to day 7. The optimal expression levels of LMX1B were reached on day 6 for all LMX1B variants. All cells showed a clear band in the Western blot in addition to a positive immunofluorescence staining against LMX1B in the nuclei, Figure 3.13 - Figure 3.16, [A] and [B]. For further *in vitro* studies, expression of all LMX1B proteins (WT, H54L, C95F, and V242D) was induced for 6 days in all cell lines.

HtTA-1/myc-LMX1B (WT)

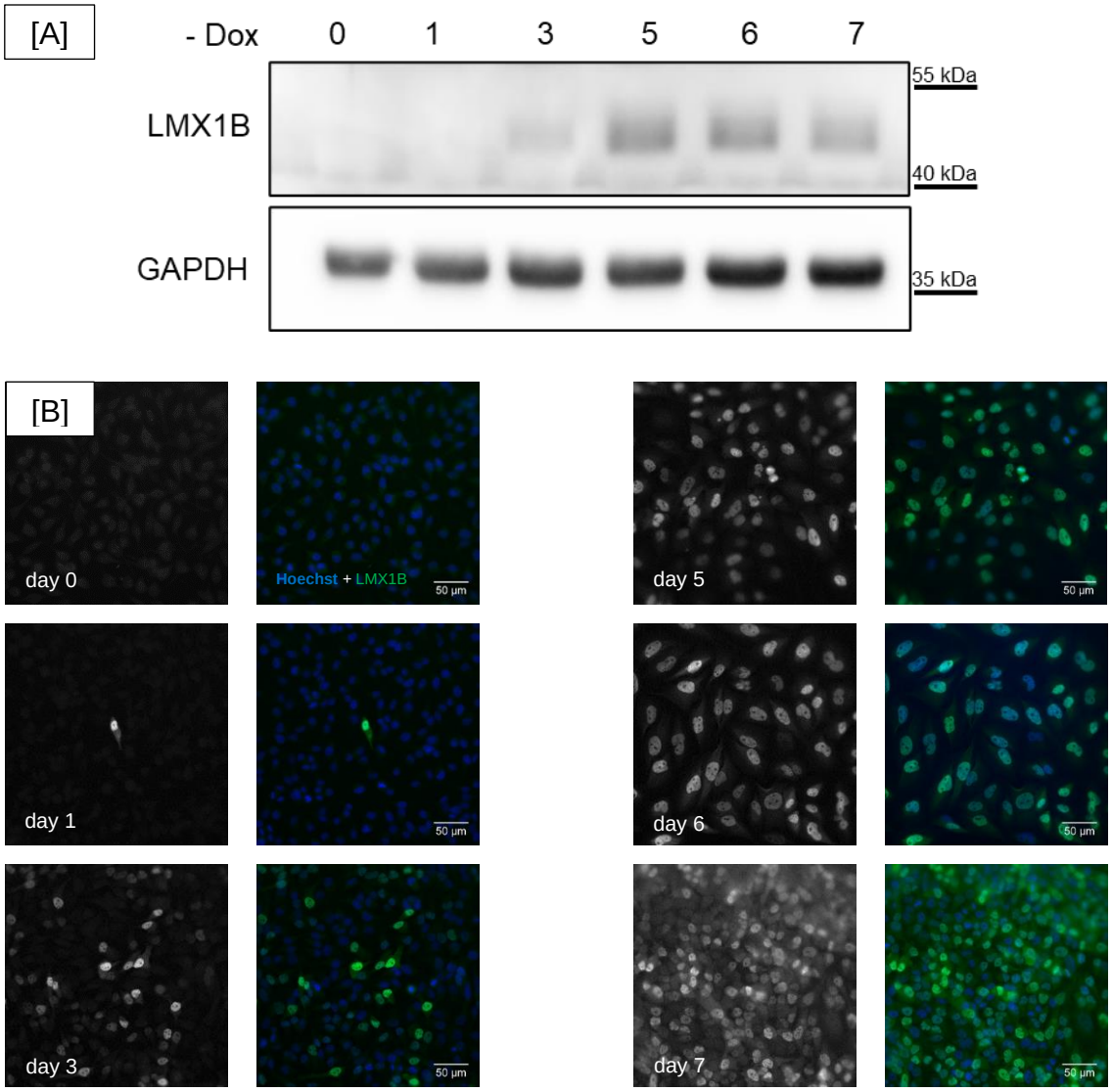

Figure 3.13: Induction series of LMX1B (WT) expression of stable transfected HtTA-1/myc-LMX1B (WT) cell line by the absence of doxycycline.

After 0, 1, 3, 5, 6 or 7 days of incubation, cells were harvested, lysed, and analyzed by western blot and immunofluorescence staining. **[A]** Western Blot against myc- LMX1B, 46 kDa, with 40 µg of whole cell protein lysates were loaded, respectively. Cell line HtTA- 1/myc- LMX1B (WT) showed an induced LMX1B (WT) expression from day 3 to 7. **[B]** Immunofluorescence staining of induction series visualized a positive LMX1B (WT) signal (green) from day 1 to 7. Nuclei staining was performed using Hoechst (blue).

HtTA-1/myc-LMX1B (H54L)

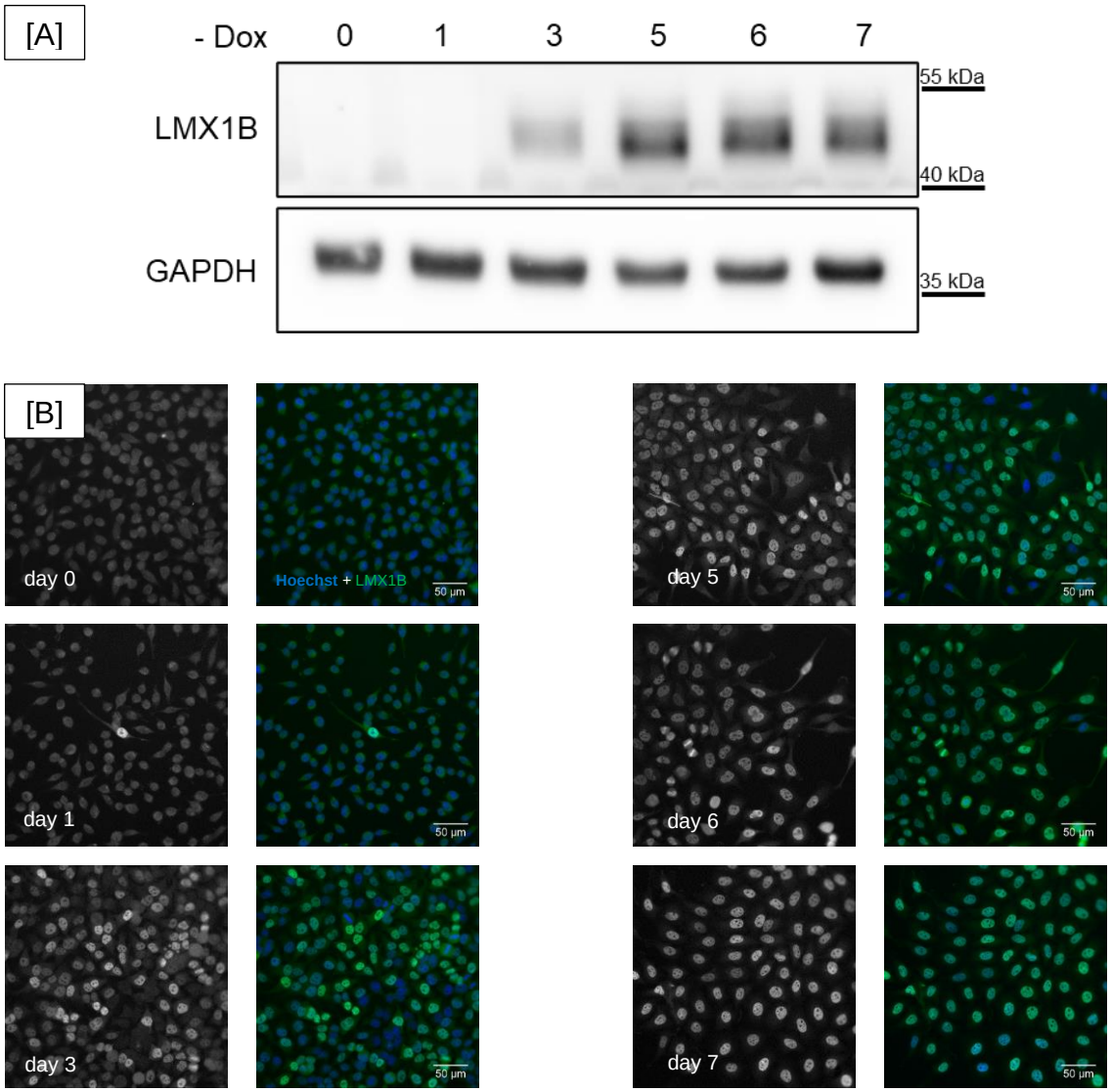

Figure 3.14: Induction series of LMX1B (H54L) expression of stable transfected HtTA-1/myc-LMX1B (H54L) cell line by the absence of doxycycline.

After 0, 1, 3, 5, 6 or 7 days of incubation, cells were harvested, lysed, and analyzed by western blot and immunofluorescence staining. **[A]** Western Blot against myc- LMX1B (H54L), 46 kDa, with 40 µg of whole cell protein lysates were loaded, respectively. Cell line HtTA- 1/myc- LMX1B (H54L) showed an induced LMX1B (H54L) expression from day 3 to 7. **[B]** Immunofluorescence staining of induction series visualized a positive LMX1B (H54L) signal (green) from day 1 to 7. Nuclei staining was performed using Hoechst (blue).

HtTA-1/myc-LMX1B (C95F)

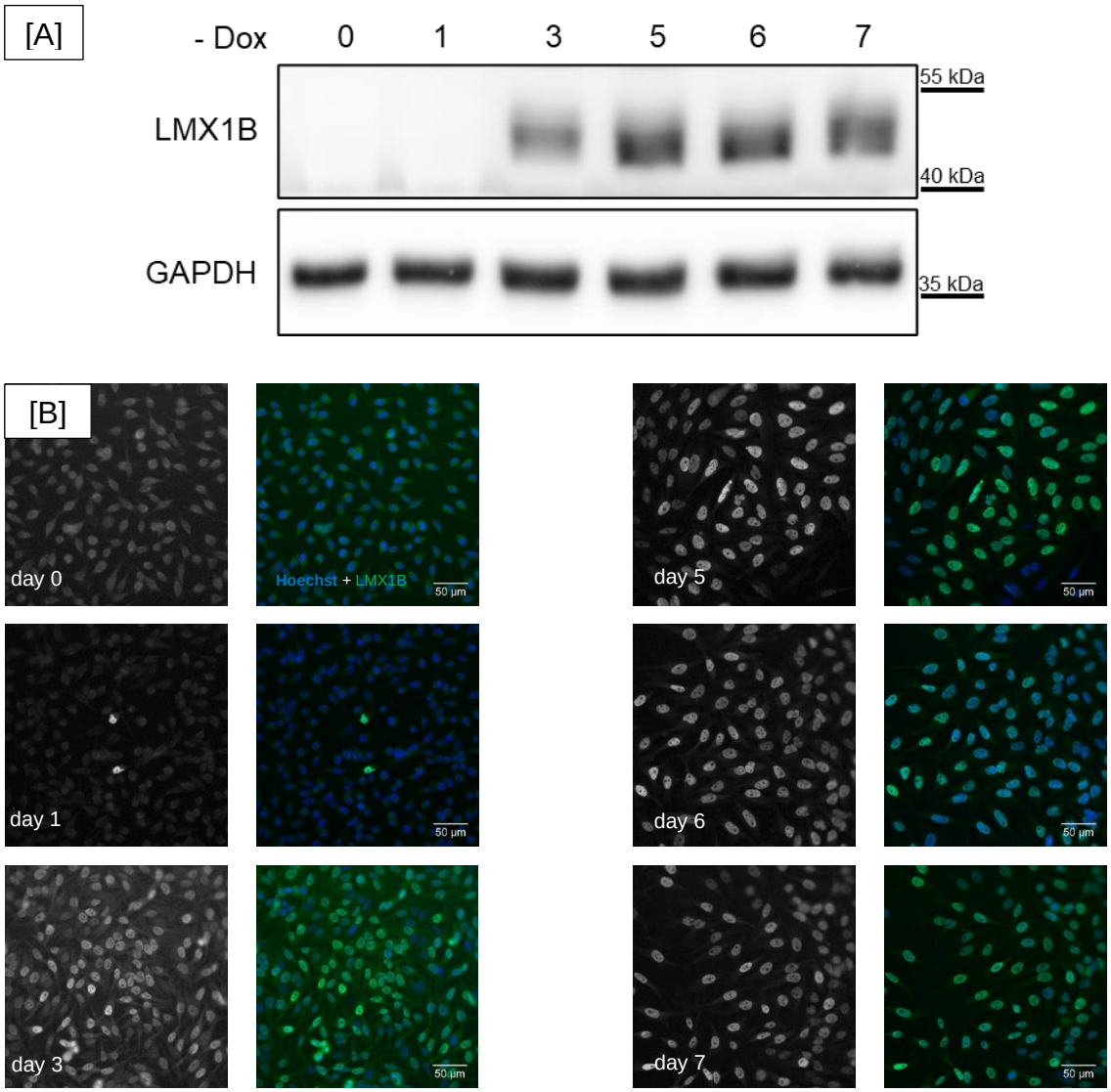

Figure 3.15: Induction series of LMX1B (C95F) expression of stable transfected HtTA-1/myc-LMX1B (C95F) cell line by the absence of doxycycline.

After 0, 1, 3, 5, 6 or 7 days of incubation, cells were harvested, lysed, and analyzed by western blot and immunofluorescence staining. **[A]** Western Blot against myc-LMX1B (C95F), 46 kDa, with 40 µg of whole cell protein lysates were loaded, respectively. Cell line HtTA- 1/myc- LMX1B (C95F) showed an induced LMX1B (C95F) expression from day 3 to 7. **[B]** Immunofluorescence staining of induction series visualized a positive LMX1B (C95F) signal (green) from day 1 to 7. Nuclei staining was performed using Hoechst (blue).

HtTA-1/myc-LMX1B (V242D)

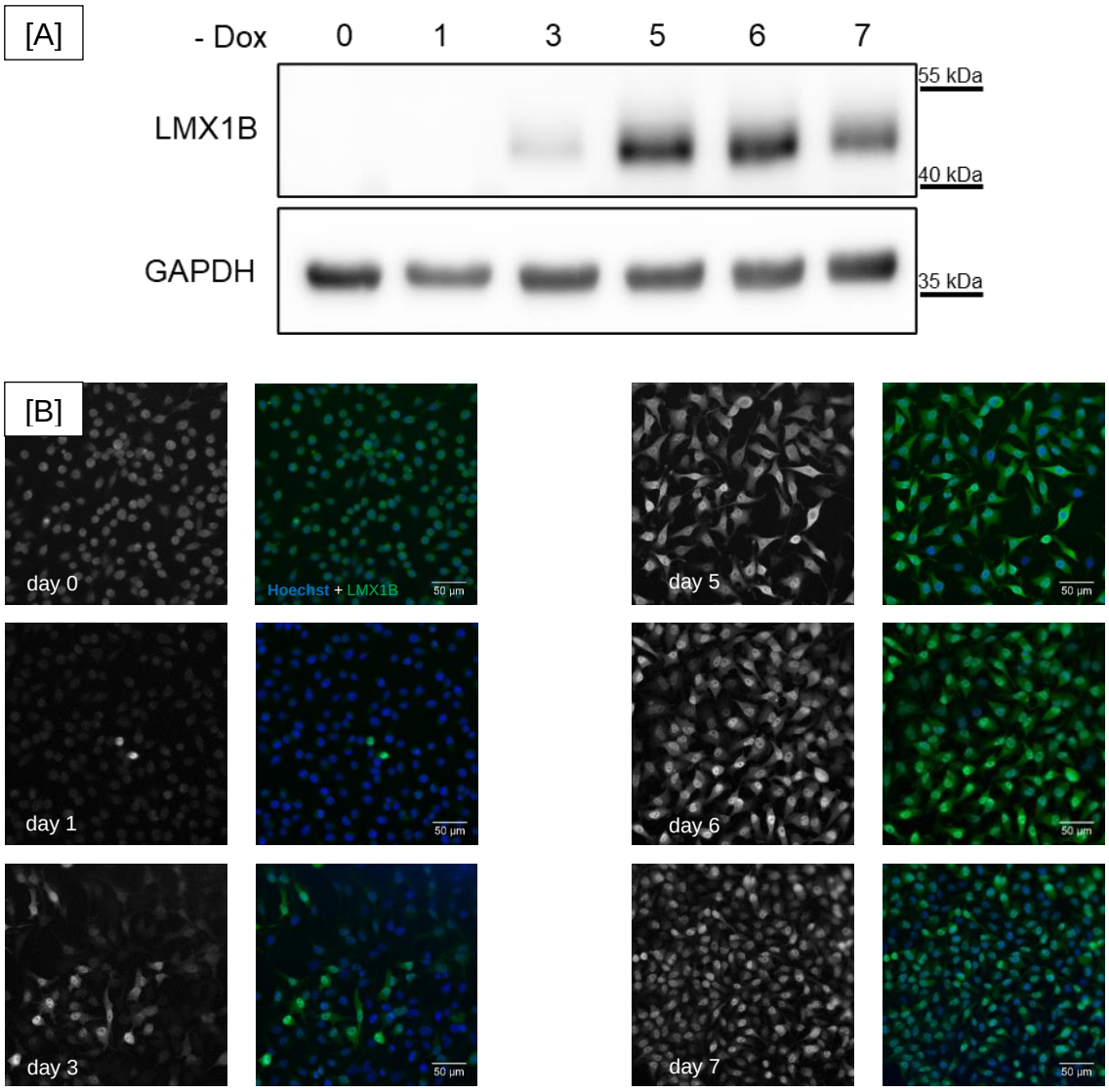

Figure 3.16: Induction series of LMX1B (V242D) expression of stable transfected HtTA-1/myc-LMX1B (V242D) cell line by the absence of doxycycline.

After 0, 1, 3, 5, 6 or 7 days of incubation, cells were harvested, lysed, and analyzed by western blot and immunofluorescence staining. **[A]** Western Blot against myc-LMX1B (V242D), 46 kDa, with 40 µg of whole cell protein lysates were loaded, respectively. Cell line HtTA-1/myc-LMX1B (V242D) showed an induced LMX1B (V242D) expression from day 3 to 7. **[B]** Immunofluorescence staining of induction series visualized a positive LMX1B (V242D) signal (green) from day 1 to 7. Nuclei staining was performed using Hoechst (blue).

3.2.3 Half-life of LMX1B mutant proteins

In *Lmx1b* knock-in mice, the mutant proteins Lmx1b (H54L) and Lmx1b (C95F) were not detectable. In light of the fact, that both knock-in transcripts were present, this brings up the question, why the protein could not be verified. Therefore, the half-lives of the wild-type and mutant LMX1B proteins were measured by cycloheximide chase assays. As shown in western blots of Figure 3.17 [A], knock-in mutations in the *LMX1B* gene significantly decreased the protein half-life. LMX1B (WT) protein has a half-life of around 4.5 hours, LMX1B (H54L) ~1.5 hours and LMX1B (C95F) around 45 minutes, Figure 3.17, [B]. This suggested that the mutant variants could be more susceptible to intracellular degradation than the LMX1B wild-type protein. In a previous study, the mutant LMX1B (V242D) showed a dominant-negative effect in mice (Cross *et al.* 2014). Thus, the protein turnover of this LMX1B mutant was additionally examined to clarify, whether a decreased stability of LMX1B mutants is a general phenomenon. As seen in Figure 3.18, [A] and [B], surprisingly, the mutation even increased the LMX1B protein half-life at around 8 hours. This phenomenon gave a hint that the mutant LMX1B (V242D) might be less prone to intracellular protein decay compared to LMX1B (WT) and LMX1B (H54L) as well as LMX1B (C95F) mutants.

[A]

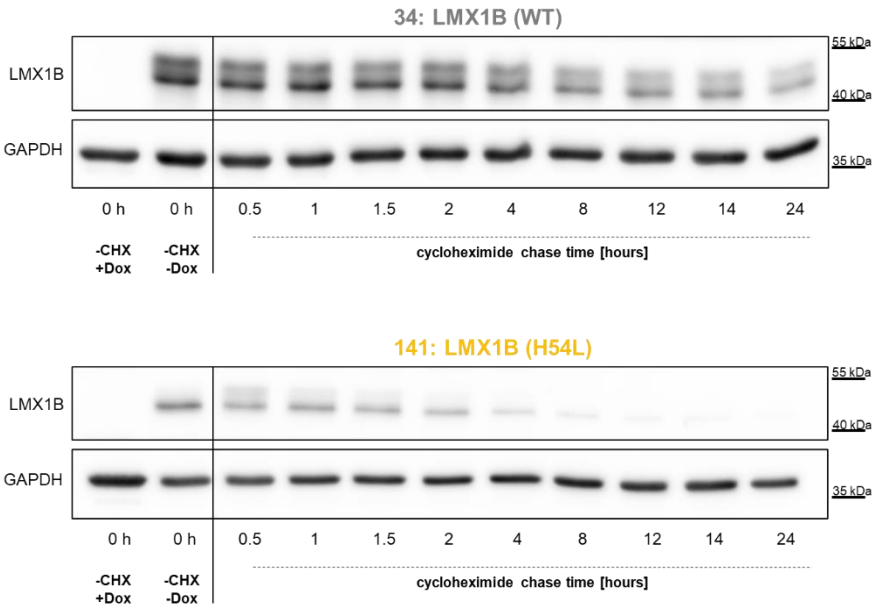

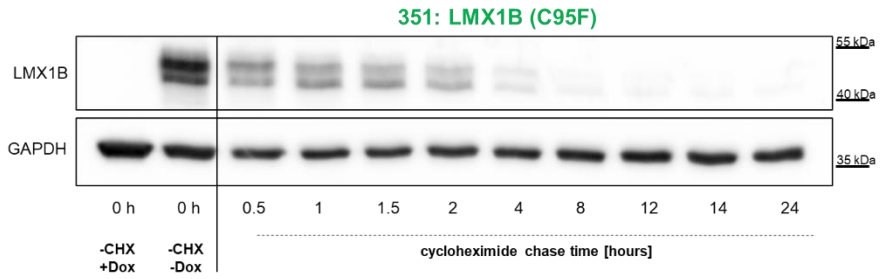

[B]

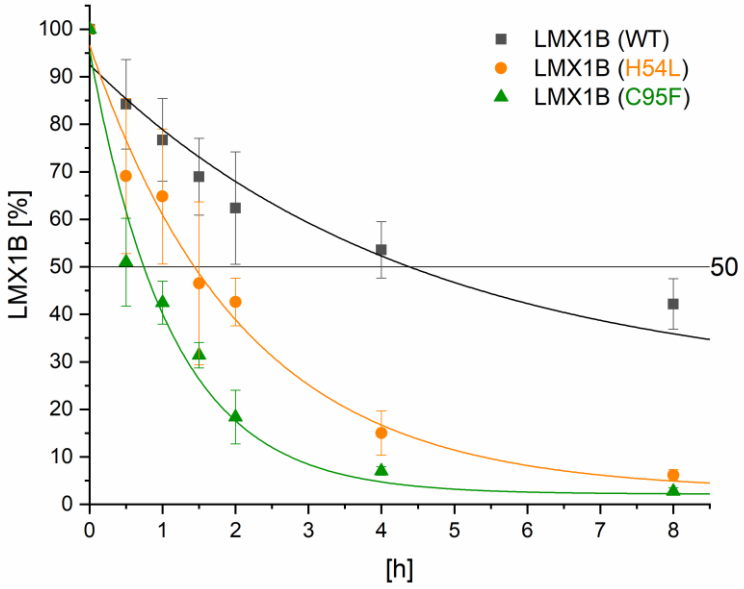

Figure 3.17: Measurement of LMX1B protein half-lives by cycloheximide chase assays.

LMX1B protein synthesis was induced for 6 days by doxycycline-free medium. On day 5, cells were split, and same number of cells was seeded in 10 different P6 dishes, one dish for each point of cycloheximide chase time. On day 6, cells were treated with cycloheximide (final concentration 100 ng/µL) for 0, 0.5, 1, 1.5, 2, 4, 8, 12, 14, and 24 hours. **[A]** Western blot against LMX1B (~46 kDa) of different cell clones. GAPDH was used as loading control. 40 µg of whole cell lysates were loaded. **[B]** Quantification of Western blots was carried out using the software Bio1D from Vilber Lourmat. Determined half-life of LMX1B (WT) (grey, wild-type LMX1B protein) ~4 hours, LMX1B (H54L) (orange, mutant LMX1B knock-in protein) ~1.5 hours, and LMX1B (C95F) (green, mutant LMX1B knock-in protein) ~45 minutes. Quantitative data are presented as mean values and ± standard deviation, n = 4 independent experiments.

[A]

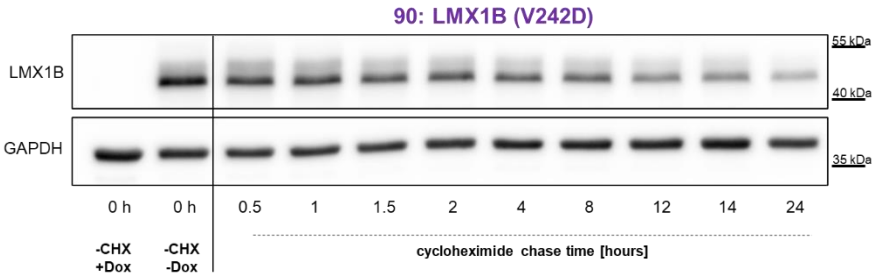

[B]

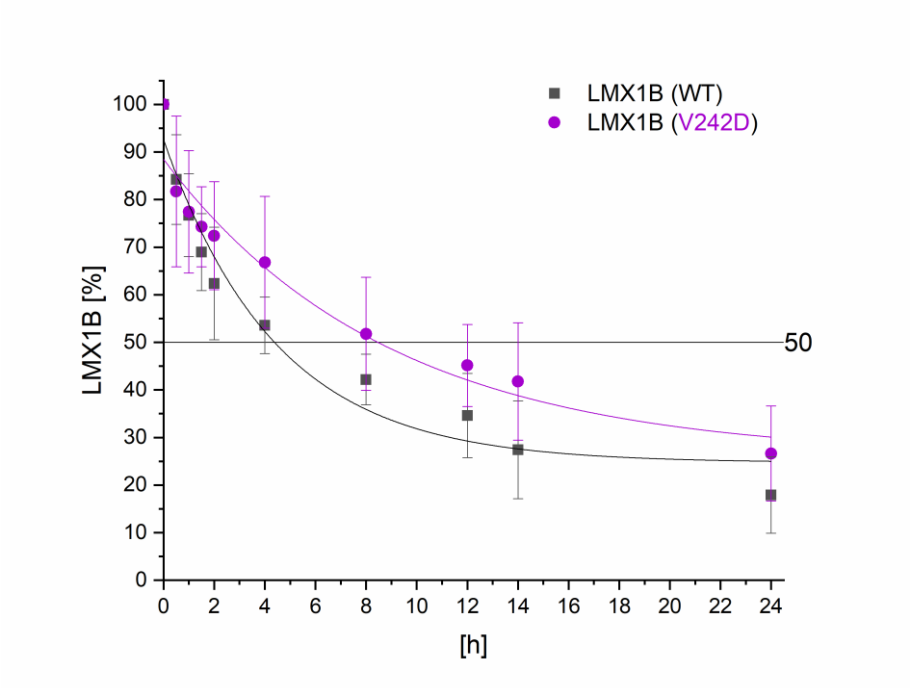

Figure 3.18: Analysis of LMX1B (V242D) protein half-life by cycloheximide chase assay compared to LMX1B (WT).

LMX1B protein expression was induced for 6 days by the absence of doxycycline in the medium. On day 5, cells were split and the same number of cells was seeded in 10 P6 dishes due to different harvest time points. On day 6, cells were treated with cycloheximide (final concentration 100 ng/µL) for 0, 0.5, 1, 1.5, 2, 4, 8, 12, 14, and 24 hours. **[A]** Western blot against LMX1B (~46 kDa) of cell clone 90 stable transfected with LMX1B (V242D). GAPDH was used as loading control. 40 µg of whole cell protein lysates were loaded, respectively. **[B]** Quantification results of western blots. Half-lives: LMX1B (WT) (grey, wild-type LMX1B protein) ~4 hours, same data as shown in Figure 3.17, LMX1B (V242D) (purple, LMX1B mutant protein) ~8 hours. Quantitative data are presented as mean values and ± standard deviation, n = 4 independent experiments.

3.2.4 Degradation pathway of LMX1B

To get insights into the mechanisms of degradation, cycloheximide chase assays have been carried out in the presence of the lysosome inhibitor Bafilomycin A_1 or the proteasome inhibitors, either MG-132 or bortezomib, also known as PS-341.

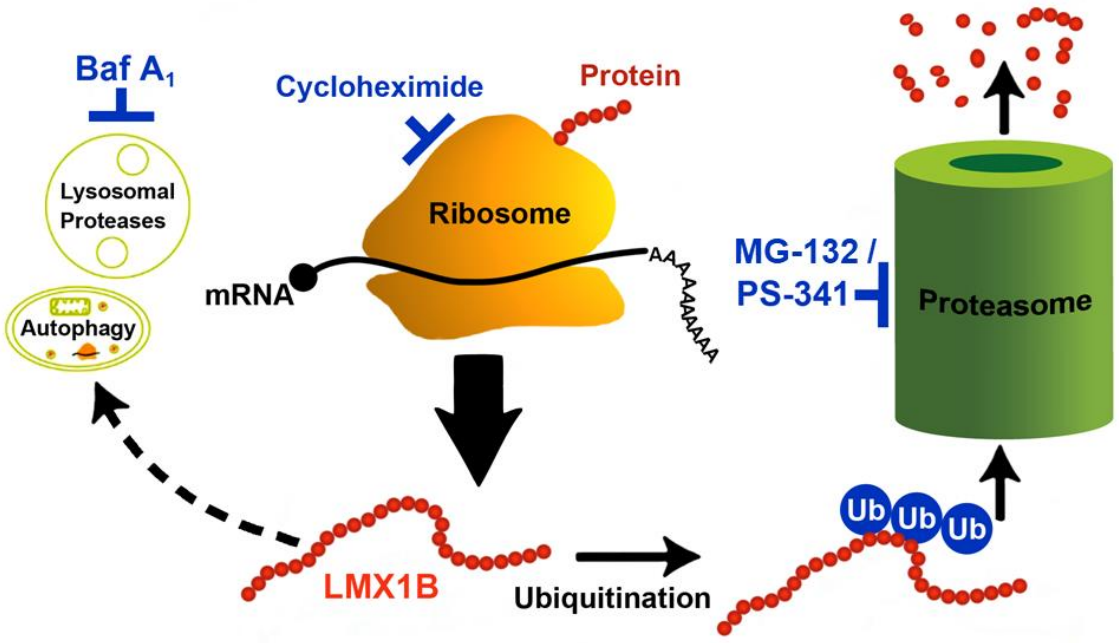

Figure 3.19: Model of possible degradation pathways of LMX1B.
The ribosome produces new protein chains. Cycloheximide treatment allows us to observe protein degradation as decreased abundance over time. Under normal conditions, unfolded protein is quickly degraded by one of the two possible pathways: either the lysosome or the proteasome. Inhibition of the lysosome using Bafilomycin A_1 (Baf-A_1) or the proteasome by bortezomib (PS-341) or MG-132 treatment, the respective pathway gets blocked. This induces an accumulation of the LMX1B protein. Model is adapted from (Larance *et al.* 2013).

Both proteasome inhibitors, MG-132 and PS-341, significantly slowed down the protein degradation and were able to almost restore protein levels of LMX1B (WT), LMX1B (H54L), and LMX1B (C95F) as well as LMX1B (V242D) (Figure 3.20 and Figure 3.21). However, the effect was stronger in the presence of PS-341 indicating to be a more efficient proteasomal blocker compared to MG-132. Inhibition of the lysosome by Bafilomycin A_1 (Baf-A_1) did not change the half-life of LMX1B wild-type or mutant proteins (Figure 3.22). These data mean that the LMX1B protein turnover inside the cell is mediated by the proteasome instead of the lysosomal pathway. In addition, LMX1B knock-in mutants were more susceptible to proteasomal degradation than LMX1B (WT), whereas LMX1B (V242D) showed even a higher stability.

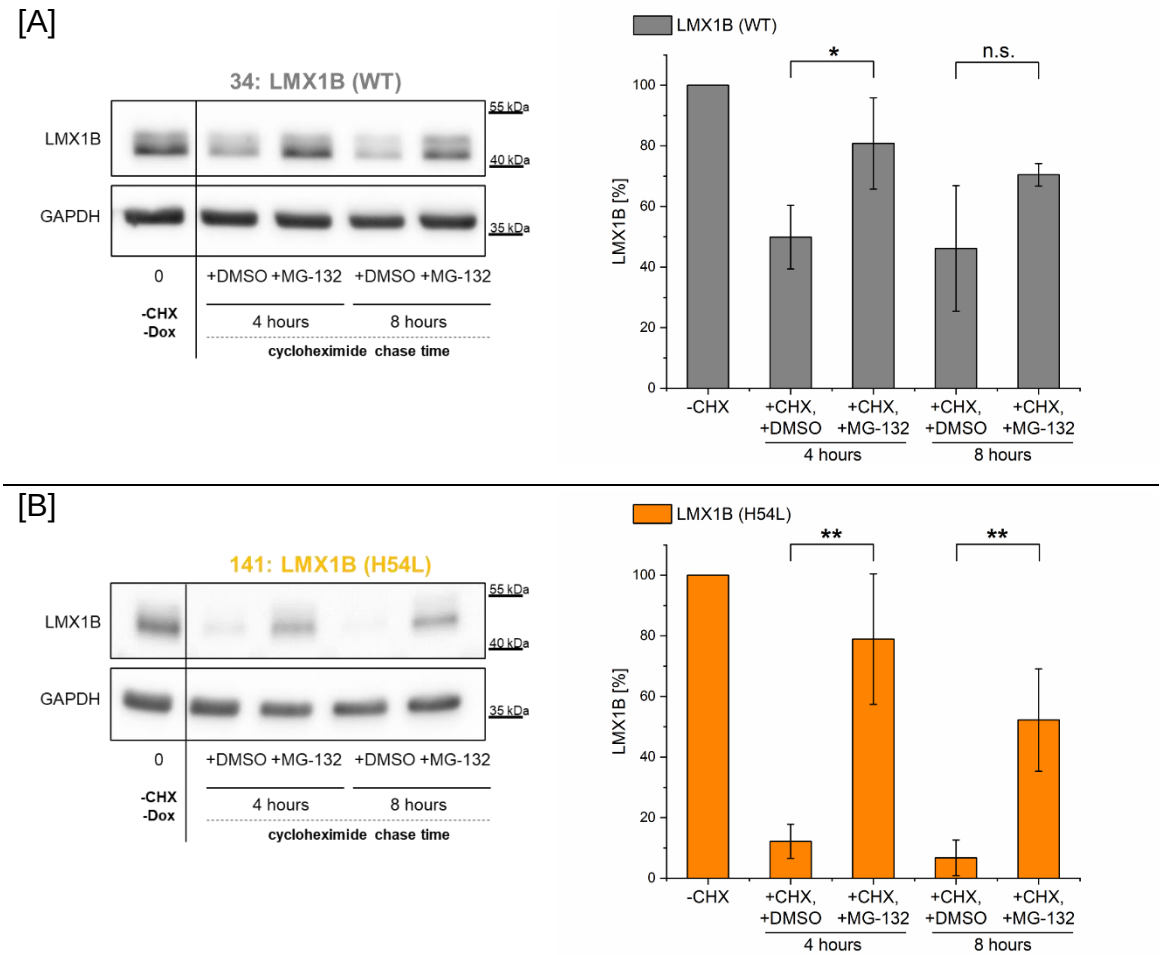

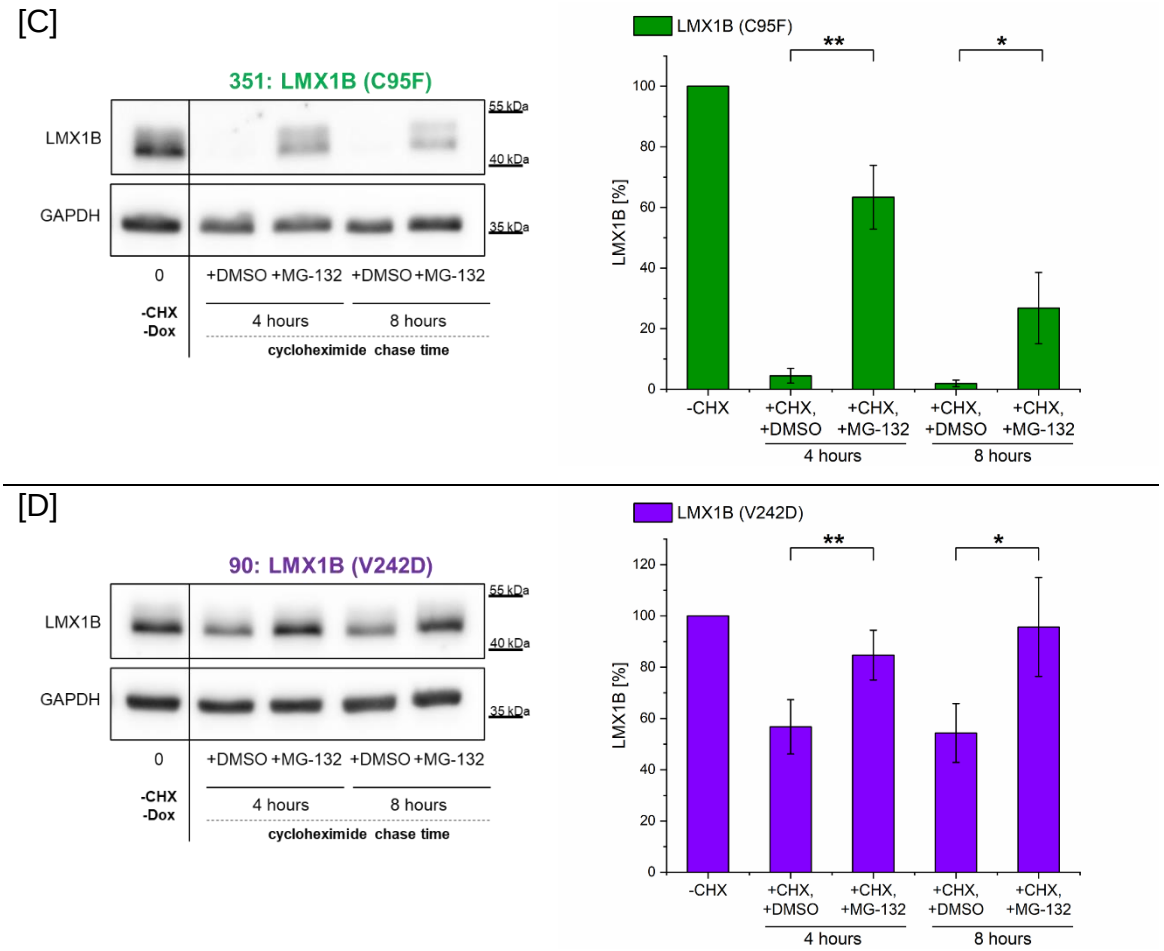

Figure 3.20: Effect of the proteasome inhibitor MG-132 on LMX1B protein degradation for 4 and 8 hours.

HtTA-1 cells were stably transfected either with the control LMX1B (WT), LMX1B (H54L), LMX1B (C95F) or LMX1B (V242D) expression plasmids, respectively. Expression of LMX1B was induced for 6 days. On day 5, the same number of cells was seeded in different P6 dishes according to harvest time points. On day 6, cells were treated with 100 ng/µL cycloheximide and DMSO (control) or 10 µM MG-132 for 0, 4, and 8 hours. 40 µg of whole cell protein lysates were loaded for Western blot against LMX1B (~46 kDa) and GAPDH (~36 kDa) as a loading control. Western blots were quantified using the software Bio1D. Quantitative analysis of data were presented as mean values ± standard deviation. Statistical significance was calculated by unpaired two-tailed Student´s t-test. N = 4, * $p < 0.01$; ** $p < 0.05$. **[A]** Data of LMX1B wild-type (grey, LMX1B (WT)); **[B]** LMX1B (H54L) mutant (orange); **[C]** LMX1B (C95F) mutant (green); **[D]** LMX1B (V242D) mutant (purple).

[A]

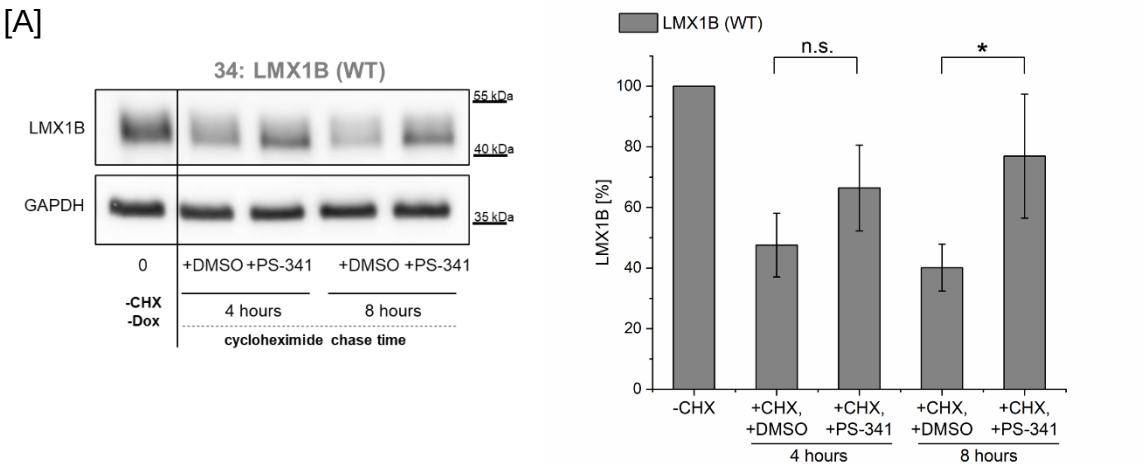
34: LMX1B (WT)
LMX1B
GAPDH
55 kDa
40 kDa
35 kDa
0
+DMSO +PS-341
+DMSO +PS-341
-CHX
-Dox
4 hours
8 hours
cycloheximide chase time
LMX1B (WT)
n.s.
*
LMX1B [%]
-CHX
+CHX, +DMSO
+CHX, +PS-341
+CHX, +DMSO
+CHX, +PS-341
4 hours
8 hours

[B]

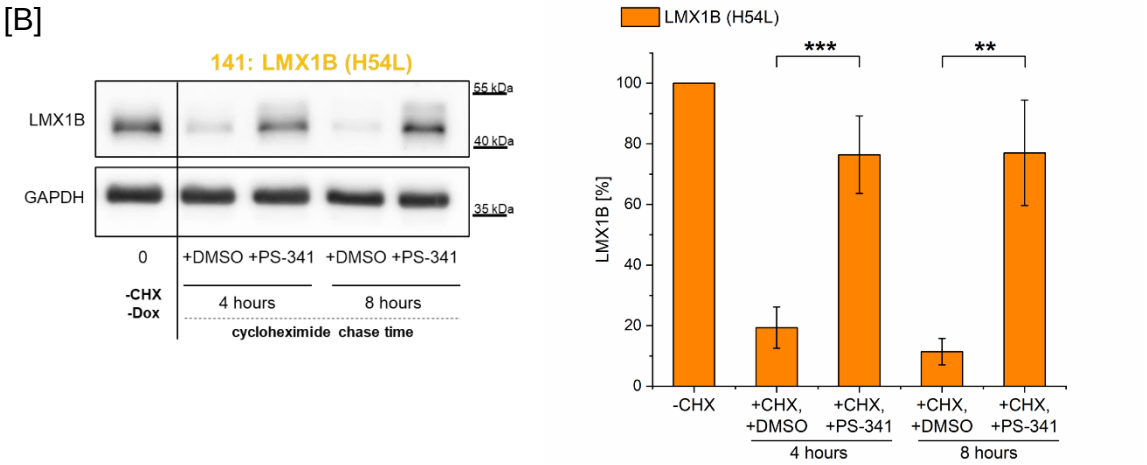
141: LMX1B (H54L)
LMX1B
GAPDH
55 kDa
40 kDa
35 kDa
0
+DMSO +PS-341
+DMSO +PS-341
-CHX
-Dox
4 hours
8 hours
cycloheximide chase time
LMX1B (H54L)
***
**
LMX1B [%]
-CHX
+CHX, +DMSO
+CHX, +PS-341
+CHX, +DMSO
+CHX, +PS-341
4 hours
8 hours

[C]

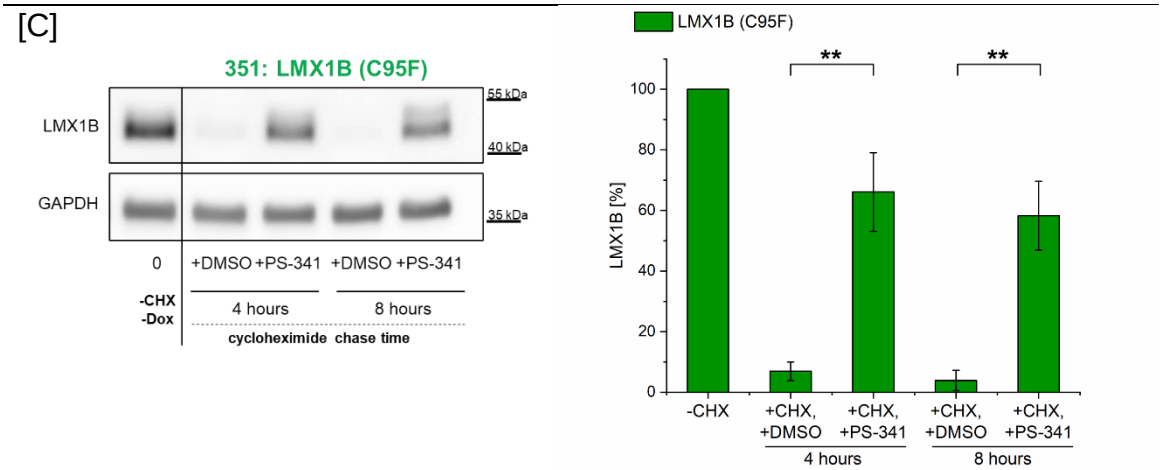
351: LMX1B (C95F)
LMX1B
GAPDH
55 kDa
40 kDa
35 kDa
0
+DMSO +PS-341
+DMSO +PS-341
-CHX
-Dox
4 hours
8 hours
cycloheximide chase time
LMX1B (C95F)
**
**
LMX1B [%]
-CHX
+CHX, +DMSO
+CHX, +PS-341
+CHX, +DMSO
+CHX, +PS-341
4 hours
8 hours

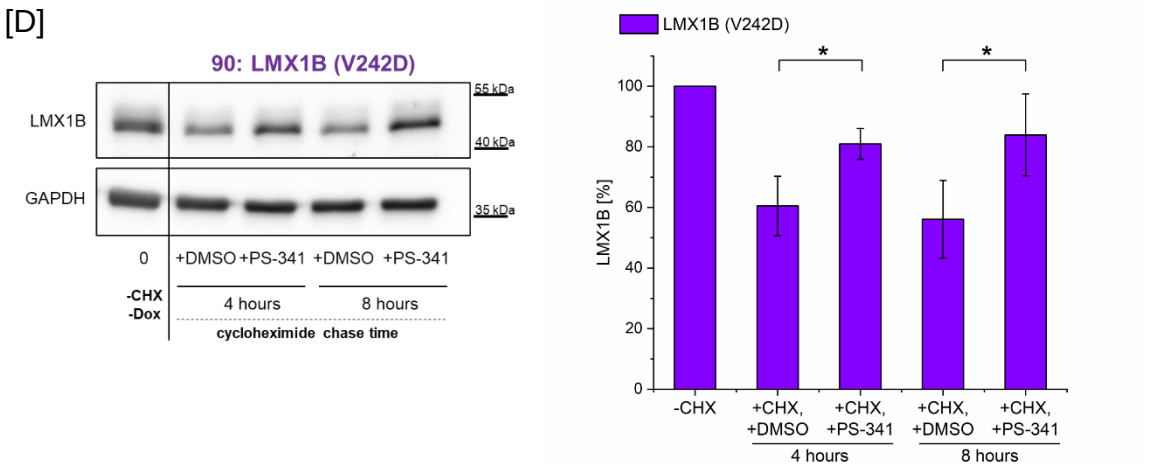

Figure 3.21: Effect of the proteasome inhibitor bortezomib (PS-341) on LMX1B protein degradation for 4 and 8 hours.

HtTA-1 cells were stably transfected either with the control LMX1B (WT), LMX1B (H54L), LMX1B (C95F) or LMX1B (V242D) expression plasmids, respectively. Expression of LMX1B was induced for 6 days. On day 5, the same number of cells was seeded in different P6 dishes according to harvest time points. On day 6, cells were treated with 100 ng/µL cycloheximide and DMSO (control) or 10 µM PS-341 for 0, 4, and 8 hours. 40 µg of whole cell protein lysates were loaded for Western blot against LMX1B (~46 kDa) and GAPDH (~36 kDa) as a loading control. Western blots were quantified using the software Bio1D. Quantitative analysis of data were presented as mean values ± SEM. Statistical significance was calculated by unpaired two-tailed Student´s t-test. N = 4, * $p < 0.01$; ** $p < 0.05$; *** $p < 0.001$. **[A]** Data of LMX1B wild-type (grey, LMX1B (WT)); **[B]** LMX1B (H54L) mutant (orange); **[C]** LMX1B (C95F) mutant (green); **[D]** LMX1B (V242D) mutant (purple).

[A]

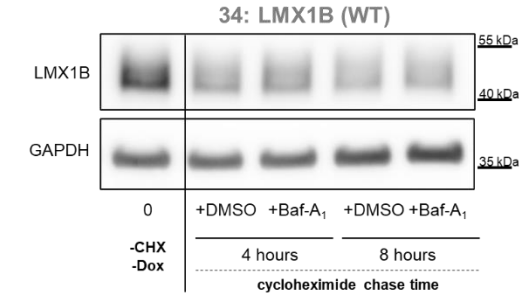
34: LMX1B (WT)
LMX1B
GAPDH
55 kDa
40 kDa
35 kDa
0
+DMSO +Baf-A1 +DMSO +Baf-A1
-CHX
-Dox
4 hours 8 hours
cycloheximide chase time

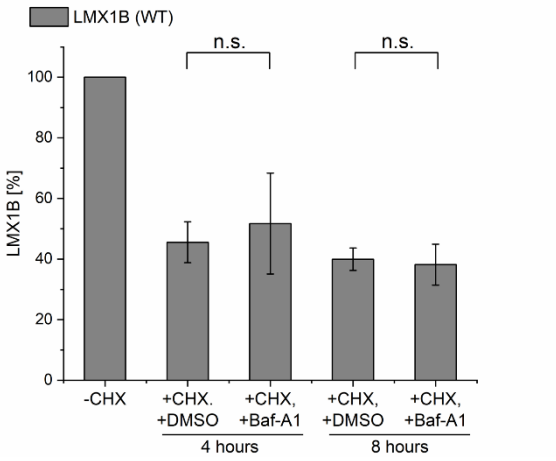
LMX1B (WT)
n.s.
n.s.
LMX1B [%]
100
80
60
40
20
0
-CHX
+CHX. +DMSO
+CHX, +Baf-A1
+CHX, +DMSO
+CHX, +Baf-A1
4 hours
8 hours

[B]

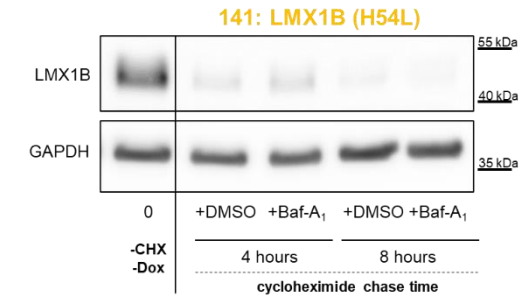
141: LMX1B (H54L)
LMX1B
GAPDH
55 kDa
40 kDa
35 kDa
0
+DMSO +Baf-A1 +DMSO +Baf-A1
-CHX
-Dox
4 hours 8 hours
cycloheximide chase time

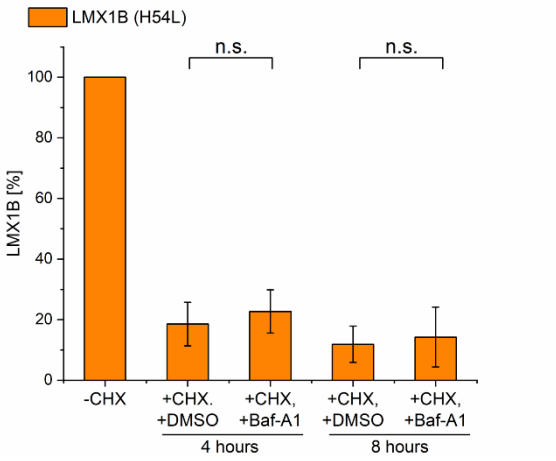
LMX1B (H54L)
n.s.
n.s.
LMX1B [%]
100
80
60
40
20
0
-CHX
+CHX. +DMSO
+CHX, +Baf-A1
+CHX, +DMSO
+CHX, +Baf-A1
4 hours
8 hours

[C]

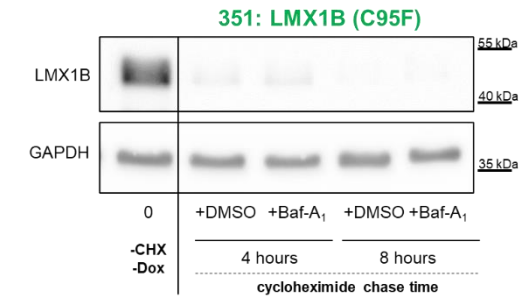
351: LMX1B (C95F)
LMX1B
GAPDH
55 kDa
40 kDa
35 kDa
0
+DMSO +Baf-A1 +DMSO +Baf-A1
-CHX
-Dox
4 hours 8 hours
cycloheximide chase time

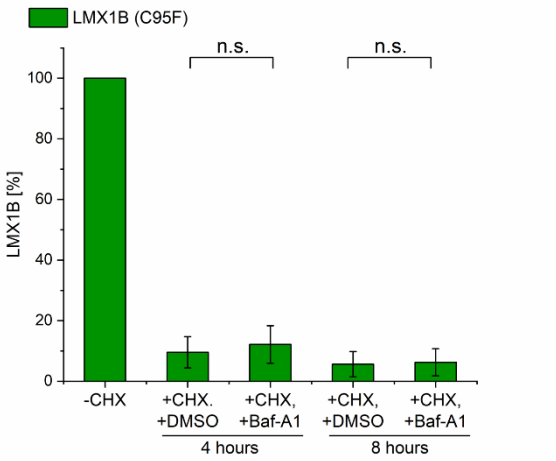
LMX1B (C95F)
n.s.
n.s.
LMX1B [%]
100
80
60
40
20
0
-CHX
+CHX. +DMSO
+CHX, +Baf-A1
+CHX, +DMSO
+CHX, +Baf-A1
4 hours
8 hours

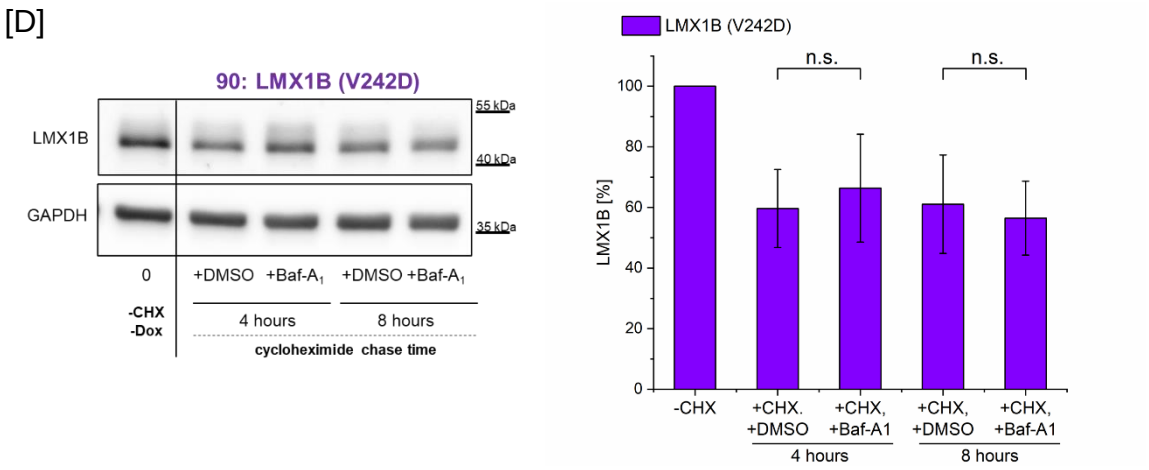

Figure 3.22: Effect of the lysosome inhibitor Bafilomycin-A_1 (Baf-A_1) on LMX1B protein degradation for 4 and 8 hours.

HtTA-1 cells were stably transfected either with the control LMX1B (WT), LMX1B (H54L), LMX1B (C95F) or LMX1B (V242D) expression plasmids, respectively. Expression of LMX1B was induced for 6 days. On day 5, the same number of cells was seeded in different P6 dishes according to harvest time points. On day 6, cells were treated with 100 ng/µL cycloheximide and DMSO (control) or 10 µM Baf-A_1 for 0, 4, and 8 hours. 40 µg of whole cell protein lysates were loaded for Western blot against LMX1B (~46 kDa) and GAPDH (~36 kDa) as a loading control. Western blots were quantified using the software Bio1D. Quantitative analysis of data were presented as mean values ± SEM. Statistical significance was calculated by unpaired two-tailed Student´s t-test. N = 3, * $p < 0.05$. **[A]** Data of LMX1B wild-type (grey, LMX1B (WT)); **[B]** LMX1B (H54L) mutant (orange); **[C]** LMX1B (C95F) mutant (green); **[D]** LMX1B (V242D) mutant (purple).

3.3 3D modeling of mutant LMX1B

To better understand the effects of the different mutant LMX1B proteins, detailed analyses of the 3D structure was performed in the following chapter.

To rationalize how amino acid substitutions could affect the LMX1B protein structure, a molecular modelling study based on the X-ray structure of the Isl1 LIM domains with Ldb1 LIM-interaction domain as a template with the stretch of aa 33-151, (PDB ID code 4JCJ) (Gadd *et al.* 2013) was performed in cooperation with Gregor Madej from research group Ziegler. For modeling, LMX1B sequence referred to NCBI NP_002307.2 was used shown in Figure 3.23, [A]. The replacement of the Histidine on position 54 with a Leucine (H54L) occurs in the first LIM (LIM 1) domain of LMX1B with the stretch 33-83. The substitution of the cysteine into a phenylalanine on position 95, located in the LIM 2 domain with the stretch 92-145. Both mutations H54L and C95F occurred in the zinc binding motifs (Figure 3.23, [B] and [C]). The amino acid changes lead to a disruption of the zinc binding domains and result in an instable protein structure. The surface potential shown in Figure 3.23, [D], revealed no alterations of the surface charge. Another mutation was analyzed locating in the homeodomain. The homeodomain of LMX1B (aa 199-257) was modeled in the same way using the X-ray structure of the homeodomains bound to DNA (PDB ID code 3A01) (Miyazono *et al.* 2010). The DNA double-strand was manually transferred from the template, the position and orientation were concluded from the structure alignment of the template and target molecules. On position 242 a valine was replaced by an aspartate. This mutation located in the DNA binding site of *LMX1B* facilitating the coordination of adenine and thymine at the major groove of DNA (Figure 3.24, [A] and [B]). The oxygen atom of the aspartate enables the DNA binding to the homeodomain of LMX1B (V242D). The surface potential was drastically altered in the LMX1B (V242D) (Figure 3.24, [D]) compared to LMX1B (WT) (Figure 3.24, [C]).

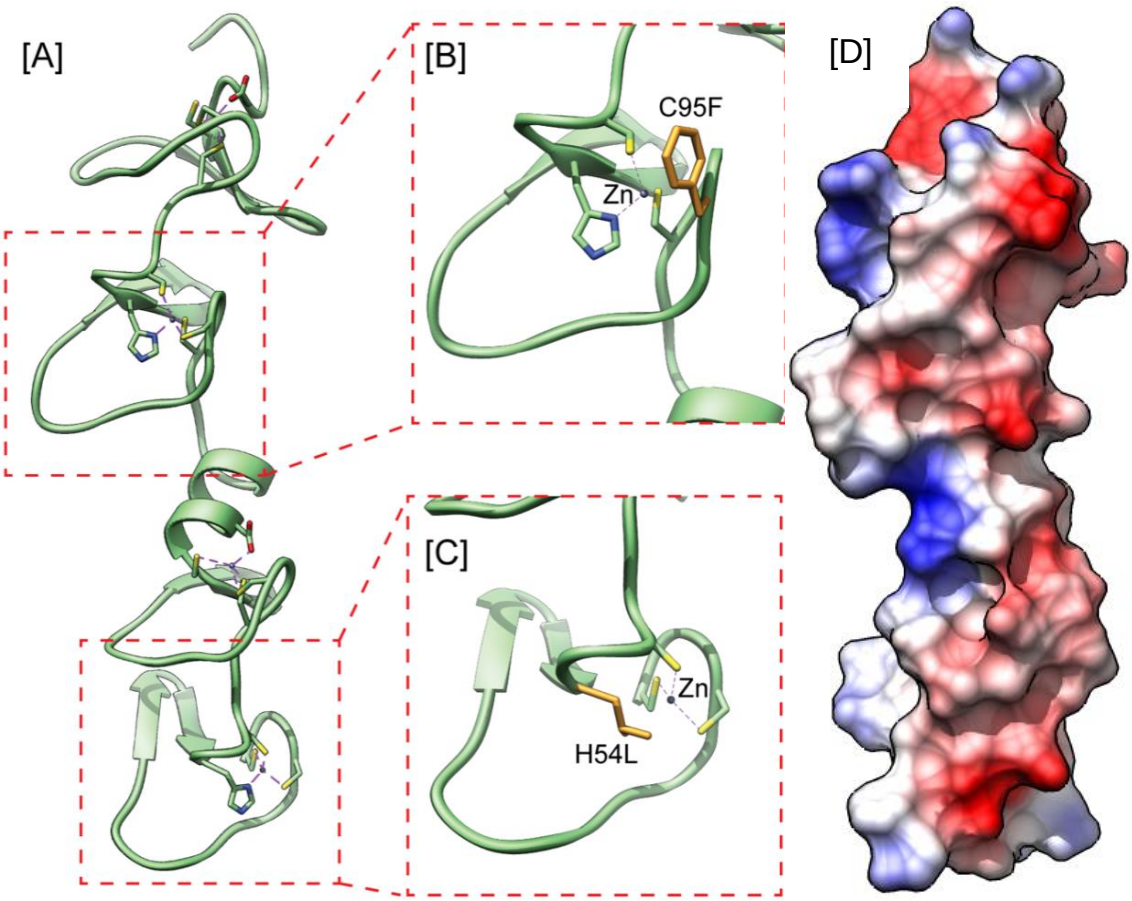

Figure 3.23: 3D structure of mutated sites in the LIM domains of LMX1B. **[A]** Ribbon model of the LIM domains from LMX1B wild-type protein with aa 33-151 according to PDB ID code 4JCJ. X-ray structure of the Isl1 LIM domains with Ldb1 LIM-interaction domain was used as a template. **[B]** Amino acid substitution of the cysteine on position 95 into a phenylalanine (orange) leads to a disrupted zinc binding site. The coordination of the zinc molecule is not sustainable resulting in a loss of LIM 2 domain structure. **[C]** On position 54 the amino acid histidine was changed by a leucine leading to a failed zinc coordination. **[D]** Surface potential of the LIM domains of LMX1B showed the distribution of positive (blue) and negative (red) charge.

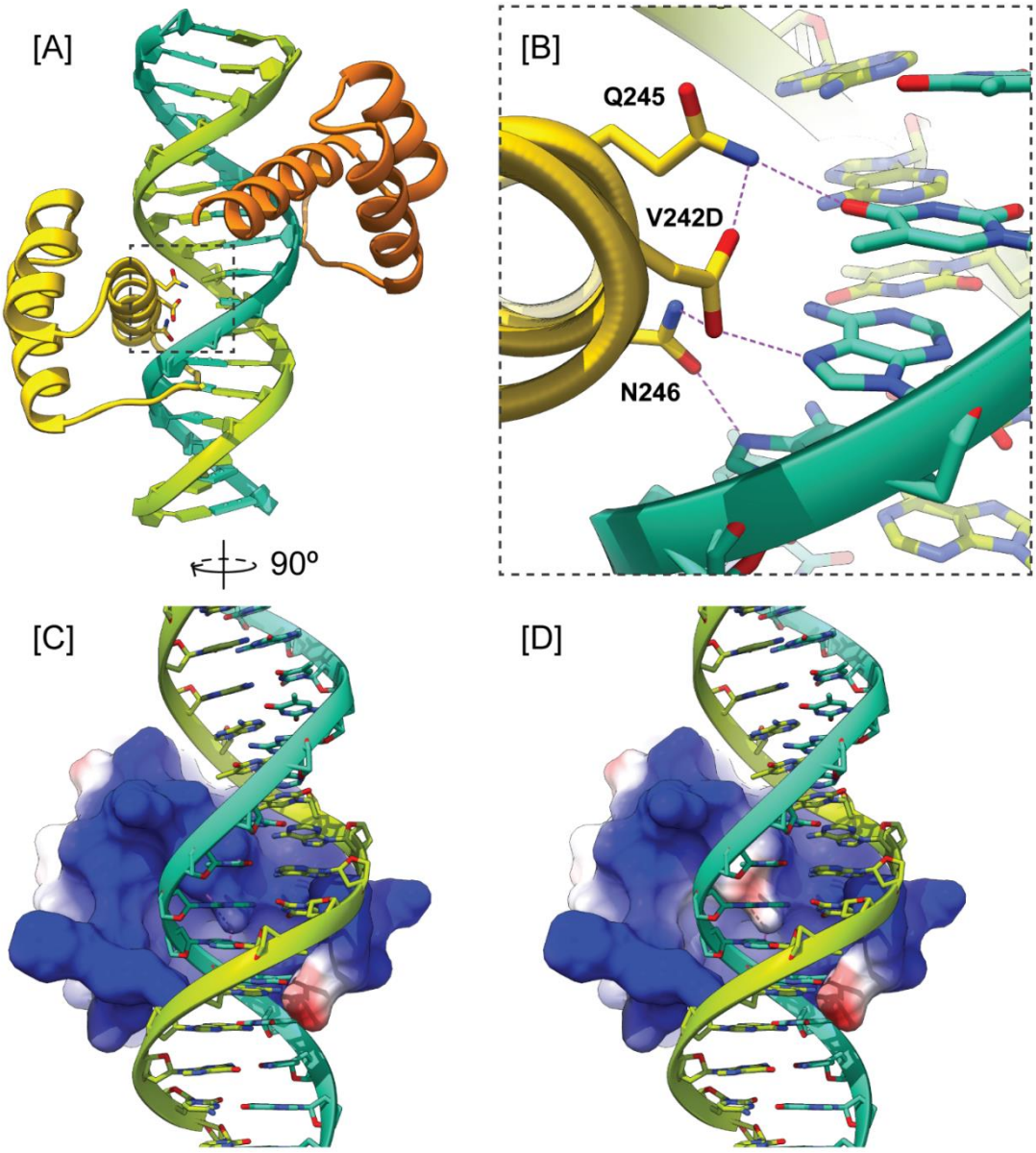

Figure 3.24: 3D structures from wild-type and mutated LMX1B homeodomain.

[A] Overview of interaction between the homeodomain of LMX1B (yellow) and the major groove of DNA (green and blue). The LMX1B homeodomain (aa 199-257) was modeled using the X-ray structure of the homeodomains bound to DNA (PDB ID code 3A01). **[B]** Mutation V242D resulted in an enhanced DNA bondage. The Aspartate coordinates a stronger binding of LMX1B and the DNA by interacting with nucleotides adenine and thymine, in addition to the residues Q245 and N246. **[C]** Analysis of the wild-type LMX1B homeodomain surface potential revealed a continuous charge distribution at the DNA binding site. View rotated through 90 °C to the left. **[D]** The mutation V242D resulted in a more negative surface potential at the DNA binding site.

3.4 Phenotypic characterization of multiple transgenic *Lmx1b* knock-in mice

Since *Lmx1b* knock-in mice are perinatally lethal, an examination of adult *Lmx1b* knock-in mice is impossible. Therefore, multiple transgenic mice were generated containing two floxed *Lmx1b* alleles together with an *NPHS2*-dependent reverse tetracycline-dependent transactivator (rtTA) and a *tetO*-dependent Cre expression cassette. In addition, these mice also harbor the mTmG-reporter gene. Because of the action of the human *NPHS2* promoter fragment, rtTA protein is exclusively produced in podocytes. These mice represented a unique tool to investigate whether Lmx1b is required during development as well as maintenance of the podocyte differentiation status. Inducible podocyte-specific *Lmx1b* knock-out mice with two *Lmx1b* alleles flanked with *loxP* sites showed no phenotype and were healthy without induction of recombination. After loss of Lmx1b during induction of Cre expression in podocytes, transgenic mice developed a strong proteinuria after seven days. To determine the consequences resulting from the point mutations coding for H54L in LIM 1 or C95F in LIM 2 in adult mice, respectively, inducible podocyte-specific *Lmx1b* knock-out mice were crossed with *Lmx1b* knock-in mice. Thereby, one *Lmx1b* allele was flanked by *loxP*-sites, whereas the other *Lmx1b* allele carried the mutation encoding H54L or C95F (*Lmx1b* $^{KI/lox}$). Since it is known, that inducible podocyte-specific *Lmx1b* knock-out mice develop a strong proteinuria resulting from the loss of *Lmx1b* in differentiated podocytes, it prompts the question, whether mice still exhibit a proteinuria, when only one copy of *Lmx1b* is recombined and one *Lmx1b* copy is still present but harboring either the mutation for Lmx1b (H54L) in LIM1 or Lmx1b (C95F) in LIM2. If the Lmx1b (H54L) and Lmx1b (C95F) have residual functions, the proteinuria should be weaker as in knock-out animals. The results showed that none of the mice died within the week of induction, but they developed a strong proteinuria after seven days of doxycycline administration. This effect resembled to the inducible podocyte-specific *Lmx1b* knock-out mice, in addition suggesting that the glomerular filtration barrier was affected after recombination of the *Lmx1b* gene in presence of the point mutations coding for Lmx1b (H54L) and Lmx1b (C95F) Figure 3.25.

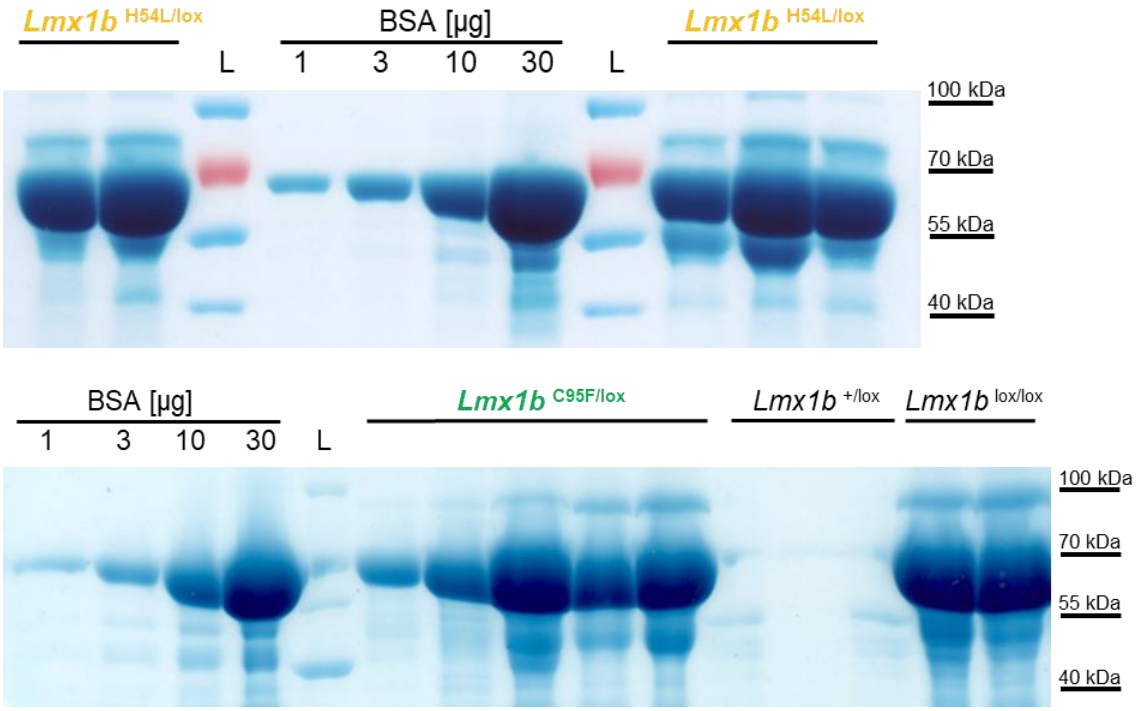

Figure 3.25: Proteinuria of podocyte-specific compound heterozygous *Lmx1b* knock-out and knock-in mice.
Experimental mice with genotypes: *NPHS2*::rtTA, *tetO*::Cre, *mTmG* he, *Lmx1b* $^{H54L/lox}$; *NPHS2*::rtTA, *tetO*::Cre, *mTmG* he, *Lmx1b* $^{C95F/lox}$. Control mice: *NPHS2*::rtTA, *tetO*::Cre, *mTmG* he, *Lmx1b* $^{lox/lox}$; *NPHS2*::rtTA, *tetO*::Cre, *mTmG* he, *Lmx1b* $^{+/lox}$. A 2 mg/ml doxycycline, 5% sucrose for 7 days in the drinking water. Urine sample was collected and 1 µl urine was loaded on a 10% SDS-gel, which was subsequently stained in an amido black solution. A strong proteinuria was detected in experimental mice after 7 days of induction, control animals (*Lmx1b* $^{+/lox}$, n=3) did not develop any proteinuria. Control mice with the complete podocyte-specific *Lmx1b* knock-out (*Lmx1b* $^{lox/lox}$, n=2) and *Lmx1b* knock-out/knock-in mice (*Lmx1b* $^{H54L/lox}$, n=5 and *Lmx1b* $^{C95F/lox}$, n=5) revealed a severe proteinuria after 7 days of induction. Variable amounts (1, 3, 10, 30 µg) of BSA served as a comparison.

3.5 Therapeutic effect of the proteasome inhibitor bortezomib on proteinuria of multiple transgenic mice

The mutated Lmx1b proteins were not detectable in homozygous *Lmx1b* knock-in mice on E18.5 (also see 3.1.5). As described in previous chapters 3.2.3 and 3.4, the point mutated *LMX1B* variants, encoding LMX1B (H54L) or LMX1B (C95F), showed an instability *in vitro* and the adult inducible podocyte-specific compound heterozygous *Lmx1b* mice developed a severe proteinuria. This might refer to a possible premature protein decay by the proteasome of the mutant Lmx1b variants. The following experiment was conducted to test the efficacy of the proteasome inhibitor bortezomib on proteinuria after Lmx1b inactivation in addition to the presence of point mutation encoding Lmx1b (H54L) or Lmx1b (C95F) *in vivo*. The addressed question was, if it is possible to stabilize the mutant Lmx1b (H54L) and Lmx1b (C95F) protein levels *in vivo* after application of the proteasome inhibitor bortezomib, thereby preventing a kidney damage Figure 3.26 [A] and [B]. Bortezomib is an approved chemotherapeutic substance which is used in cancer therapy of multiple myeloma to inhibit tumor growth.

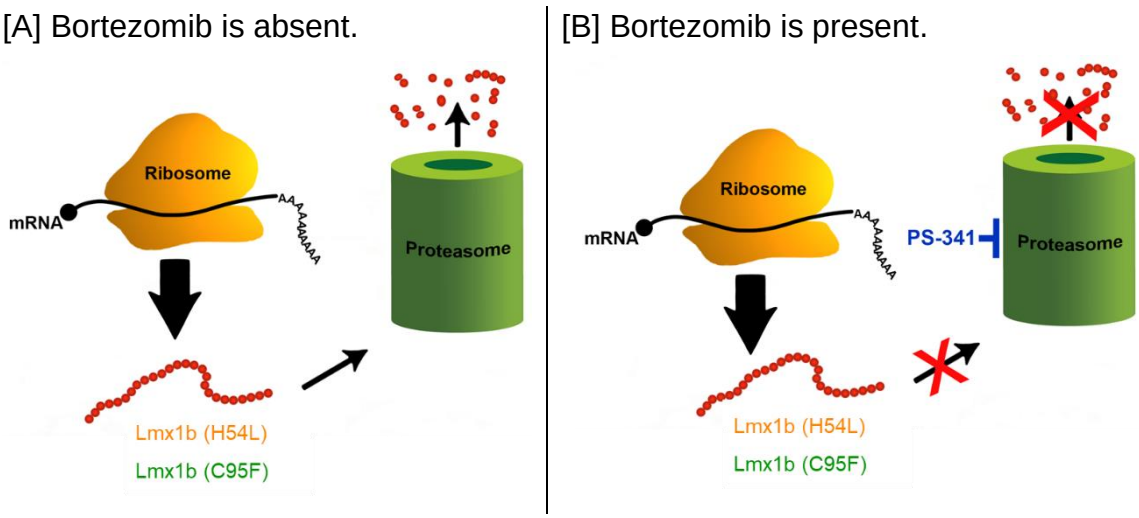

Figure 3.26: Prevention of Lmx1b (H54L) and Lmx1b (C95F) protein degradation by the proteasome *in vivo*.
Model adapted from (Larance *et al.* 2013) shows the mechanism of the bortezomib action. **[A]** The ribosome produces new protein chains, under normal conditions unfolded Lmx1b protein is quickly degraded by the proteasome. **[B]** Proteasome inhibition by bortezomib (PS-341) blocks the degradation of unfolded proteins and might be a therapeutical approach for treatment of nail-patella syndrome patients.

For this first experiment, the inducible podocyte-specific *Lmx1b* knock-out mice were crossed with *Lmx1b* (C95F) knock-in mice. In this case, one copy of the *Lmx1b* gene was flanked by *loxP*-sites (in intron 3 and intron 6), on the other chromosome, *Lmx1b* carried the point mutation coding for Lmx1b (C95F). During administration of 2 mg/ml doxycycline for 7 days, *Lmx1b* was podocyte-specifically recombined resulting in an inoperative Lmx1b version. In parallel, mice were treated with the proteasome inhibitor bortezomib with the therapeutic dose of 0.3 µg/g body weight. After assessment of the body weight, spontaneously delivered urine was collected on day 0, 2, 4, and 7, and subsequently, mice were injected with the dose-dependent volume of bortezomib diluted in 1x PBS pH 7.4. Preliminary data showed that mice with genotype *Lmx1b* $^{C95F/lox}$ developed a significant reduction in proteinuria on day seven compared to the control mice after treatment with bortezomib. One mouse of the same genotype served as a control and was equally treated with the solvent DMSO showing a severe proteinuria on day seven, Figure 3.27, [A] and [B]. The body weight was not affected due to the bortezomib injections, Figure 3.27, [C].

[A]

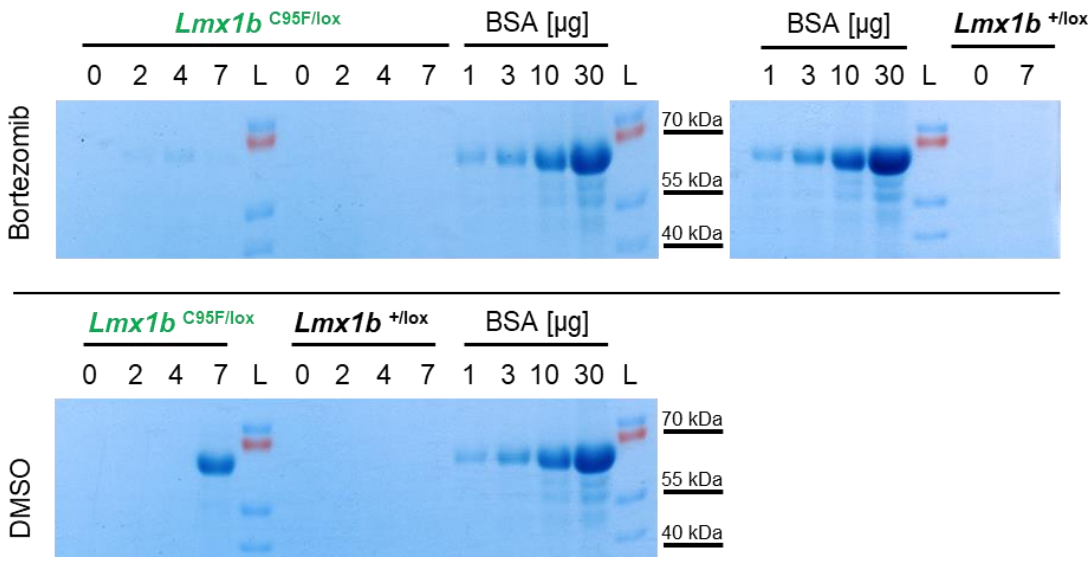

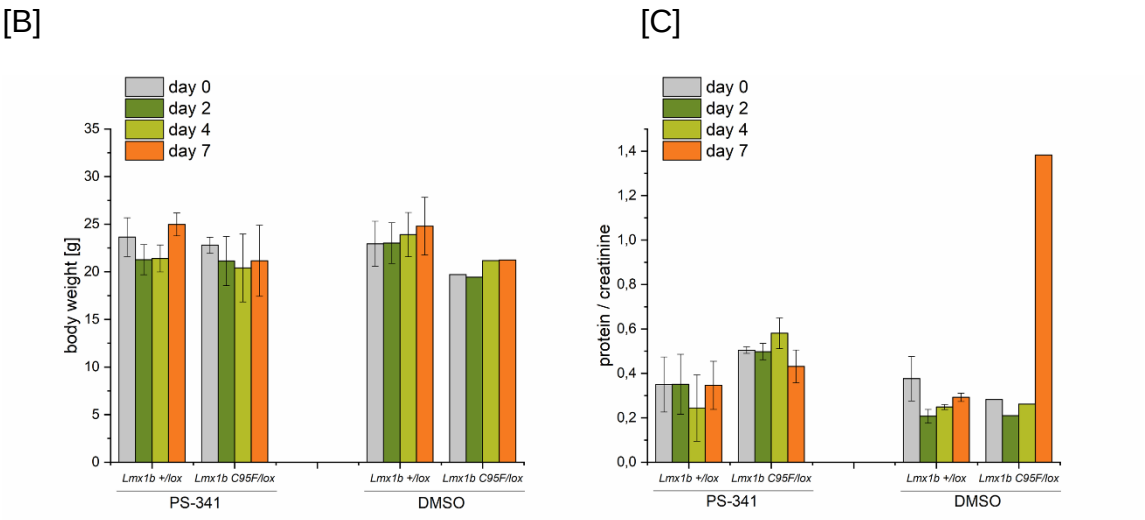

Figure 3.27: Effect of the proteasome inhibitor bortezomib on proteinuria of inducible podocyte-specific compound heterozygous *Lmx1b* mice.
Experimental mice with genotypes: *NPHS2*::rtTA, *tetO*::Cre, *mTmG* he, *Lmx1b* $^{C95F/lox}$. Control mice: *NPHS2*::rtTA, *tetO*::Cre, *mTmG* he, *Lmx1b* $^{lox/lox}$; *NPHS2*::rtTA, *tetO*::Cre, *mTmG* he, *Lmx1b* $^{+/lox}$. Recombination of *Lmx1b* flanked by *loxP*-sites was induced by 2 mg/ml doxycycline, 5% sucrose for 7 days in the drinking water. In parallel, mice were weighed and injected either with a bortezomib dose of 0.3 µg/g body weight diluted in 1x PBS pH 7.4 on day 0, 2, 4. Urine samples were collected on day 0, 2, 4, and 7. **[A]** 1 µl urine was loaded on a 10% SDS-gel, which was subsequently stained in an amido black solution. Two experimental mice (*Lmx1b* $^{C95F/lox}$) treated with bortezomib, showed a reduced proteinuria after 7 days of induction compared to mice of same genotype treated with DMSO. Control animals (*Lmx1b* $^{+/lox}$) did not develop any proteinuria after both bortezomib and DMSO administration, respectively. Variable amounts (1, 3, 10, 30 µg) of BSA served as a comparison. **[B]** Determination of body weight on day 0, 2, 4, and 7 of experimental and control mice did not reveal variations during doxycycline administration and bortezomib or DMSO injections. **[C]** Urine protein to creatinine ratio determined by Bradford protein assay and Jaffe reaction. Group PS-341: n=2, *Lmx1b* $^{C95F/lox}$, n=3, *Lmx1b* $^{+/lox}$; group DMSO: n=2, *Lmx1b* $^{C95F/lox}$, n=3, *Lmx1b* $^{+/lox}$.

4. Discussion

The disease nail-patella syndrome is described in humans as an autosomal dominant hereditary disorder with an incidence of 1:50 000 (Bongers *et al.* 2002; Witzgall 2017). The symptoms of nail-patella syndrome patients vary broadly with skeletal, ocular, and renal impairments. The renal symptoms are most important for the prognosis of the patients, comprising approximately 40% of nail-patella syndrome patients suffering from a nephropathy. This ranges from mild proteinuria over hematuria to end-stage renal disease (Sweeney *et al.* 2003). The cause for nail-patella syndrome arises from mutations in the gene encoding for the transcription factor LMX1B (Dreyer *et al.* 1998; McIntosh *et al.* 1998; Vollrath *et al.* 1998). Within the kidney, LMX1B is tissue-specific expressed in particular in developing and mature podocytes (Morello & Lee 2002). The precise molecular mechanisms that are involved during the development of renal injury in some patients, remain still unknown.

So far, for a clearer understanding of disease progression, the conventional *Lmx1b* knock-out mouse represented to be a convenient tool to investigate a range of structural and molecular alterations due to a Lmx1b defect (Chen *et al.* 1998a). Disaccording to the human patients showing an autosomal dominant mode of inheritance, *Lmx1b* knock-out mice exclusively develop a nail-patella syndrome resembling phenotype when mice show a homozygous *Lmx1b* knock-out whereas heterozygous *Lmx1b* knock-out mice appeared healthy. Homozygous *Lmx1b* knock-out mice died 24 h after birth while showing an impaired glomerular filtration barrier including a thickening of the glomerular basement membrane and a loss of podocyte foot processes with its slit diaphragms. Remarkably, the expression levels of *Nphs2*, *Col4α3*, and *Col4α4*, were reduced in those mice (Miner *et al.* 2002) whereas in human patients these genes appeared unaffected (Heidet *et al.* 2003).

Due to the human and murine discrepancies in the mode of inheritance of nail-patella syndrome, another mouse model was designed that should bypass these differences: The constitutive podocyte-specific *Lmx1b* knock-out mouse. Five days after birth, mice developed a proteinuria and died after 14 days due to renal failure. The ultrastructure of the glomerular filtration barrier showed severe impairments comprising loss of the slit diaphragms and podocyte foot processes as well as a

thickened glomerular basement membrane. Strikingly, mice revealed no alterations in the expression levels of *Nphs2*, *Col4α3*, and *Col4α4* according to human patients (Suleiman *et al.* 2007). By means of the constitutive podocyte-specific *Lmx1b* knock-out mice, no remarkable alterations in the podocytes were detected at the time of birth portending a possible involvement of Lmx1b during maintenance of podocyte structure.

This was the reason why the inducible podocyte-specific *Lmx1b* knock-out mouse was generated. The role of Lmx1b during maintenance of the podocyte structure was investigated by an induced Lmx1b knock-out in adult mice. Results showed an upregulation of mRNA levels of Abra, Arl4c and Sm22. Apart from that, in murine glomeruli a Sm22 upregulation was additionally detected on the protein level. In addition, in conditionally immortalized human podocytes a binding of LMX1B to the promoter regions of *ABRA* and *ARL4C* was verified. In summary, first results of a dysregulated actin cytoskeleton were published indicating that Lmx1b plays an important role for podocyte cell architecture (Burghardt *et al.* 2013; Setzer 2020).

To clarify precise molecular mechanisms associated with the pathogenic progression of nail-patella syndrome, a more suitable mouse model had to be generated. In the present study, the role of different mutations in the transcription factor *LMX1B* were further analyzed to establish a molecular linkage between *LMX1B* mutations and the pathogenic mechanism.

4.1 The phenotype of *Lmx1b* knock-in mice appears as a *Lmx1b* knock-out

In literature (Bongers *et al.* 2002), human nail-patella syndrome mutations are described to be mainly concentrated within the functional domains of LMX1B. About 44% of the mutations are located within the LIM 1 domain, 38% in the LIM 2 domain and about 18% were predominantly found in the homeodomain. Those mutations mainly include single base substitutions (missense, splice site, and nonsense or frameshift mutations or deletions/insertions). From the identification of putative loss-of-function mutations in *LMX1B* in nail-patella syndrome it was hypothesized that the disease originates by haploinsufficiency of *LMX1B*. A dominant-negative effect in humans, could not be excluded, since the mode of inheritance in humans and mice vary widely. To answer this question, a more appropriate mouse model had to be established to understand the precise molecular pathogenic mechanism of nail-patella syndrome. Thus, *Lmx1b* knock-in mice were generated carrying missense mutations in the different LIM domains of *Lmx1b* (Lucke *et al.*, unpublished) based on human nail-patella syndrome patients (Bongers *et al.* 2002). Since only one amino acid was substituted either in the first (H54L) or in the second (C95F) LIM domain of *Lmx1b* knock-in mice, in a first step, the LIM domain importance and functions of the mutant Lmx1b proteins were characterized within the present work. It was hypothesized that tissue-specific effects could be evoked after insertion of the respective point mutations. Due to this reason, the obvious phenotype of the *Lmx1b* knock-in mice was systematically characterized within this thesis. *Lmx1b* knock-in mice were analyzed on day E18.5 because homozygous *Lmx1b* knock-in mice die several hours after birth. Remarkably, heterozygous *Lmx1b* knock-in mice showed no obvious phenotype regarding the skeleton, the skull, exactly as heterozygous *Lmx1b* knock-out mice. Those mice were healthy and showed the phenotype of *Lmx1b* wild-type mice. In addition, the phenotype of homozygous *Lmx1b* knock-in mice reflected the phenotype of conventional *Lmx1b* knock-out mice. Patients with nail-patella syndrome and conventional *Lmx1b* knock-out mice exhibit similar dorsoventral patterning defects to bones in the limbs, including hypoplastic or absent patellae in addition to severe joint abnormalities. Most prominent was the appearance of the skull which represented various calvaria-specific defects. This was also the case for homozygous *Lmx1b* knock-in mice. µCT data and whole

mount skeletal staining reflected the image of the conventional *Lmx1b* knock-out mice. At first it was quite surprising that a single amino acid substitution can result in the same phenotype as the conventional *Lmx1b* knock-out mice. The molecular mechanisms based on the skeletal abnormalities in *Lmx1b* knock-out mice are still unknown. Mutations located in several genes are known to affect the suture development in mice or humans, such as *Fgf*, *msx-2*, and *twist* (Jabs *et al.* 1993; Opperman *et al.* 1995; el Ghouzzi *et al.* 1997; Howard *et al.* 1997; Wilkie 1997). It was assumed that *Lmx1b*, *msx-2* and *twist* constitute a genetic pathway to prevent premature osteoblast differentiation mediated by the *Fgf* receptor signaling in cranial suture development (Chen *et al.* 1998b). It has further been shown that Lmx1b plays a key role as an anti-osteogenic factor in patterning the head mesenchyme into areas with different osteogenic competence. This patterning event is crucial for proper separation of the osteogenic and non-osteogenic parts of the calvarial primordium (Cesario *et al.* 2018).

Another feature of nail-patella syndrome is proteinuria and renal insufficiency accompanied by a characteristic pathology of the glomerular basement membrane. A proper function of Lmx1b is essential for the kidney development, since homozygous *Lmx1b* knock-out mice die several hours after birth and exhibit severe nephropathies (Chen *et al.* 1998a). In addition, in those mice defects in podocyte differentiation could be observed meaning a retained cuboidal shape of the cell bodies and an absent formation of foot processes and slit diaphragms (Rohr *et al.* 2002). As a result, heterozygous *Lmx1b* knock-in mice showed no kidney phenotype equally to the heterozygous *Lmx1b* knock-out mice. The histology and ultrastructure of the glomeruli appeared healthy and in addition the number of filtration slits was not reduced. Analysis of the homozygous *Lmx1b* knock-in mice revealed an abnormal histological structure and ultrastructure of the kidneys. By means of H&E staining glomeruli appeared partially developed and the ultrastructure of the glomerular filtration barrier exhibited severe impairments. Podocytes appeared in a retained cuboidal shape and lacked foot processes including slit diaphragms. Corresponding to the homozygous *Lmx1b* knock-out, the number of filtration slits in homozygous *Lmx1b* knock-in mice were reduced compared to *Lmx1b* wild-type mice. Although no phenotype was discovered in the kidney of heterozygous *Lmx1b* knock-out mice, *Lmx1b* haploinsufficiency was described to profoundly affect the compensatory response to nephron loss in heterozygous *Lmx1b* knock-out mice

after unilateral nephrectomy (Endele *et al.* 2007). Consequently, specific pathologic situations might affect kidney functions in heterozygous *Lmx1b* knock-out mice. In summary, contrary to the expectations, the phenotype of the *Lmx1b* knock-in mice appeared as a functional *Lmx1b* knock-out. On the protein level, the mutant Lmx1b (H54L) as well as the Lmx1b (C95F) protein was not detectable in E18.5 podocytes by immunofluorescence.

At first the idea to explain this result was the response of the podocyte to recognize and degrade the aberrant Lmx1b mRNA rapidly before the accumulation of the deviant Lmx1b version could have adverse effects on the cell. But, the elimination of the mutated mRNA transcripts by the NMD pathway (Baker & Parker 2004) could be excluded since the Lmx1b (H54L) and Lmx1b (C95F) knock-in was confirmed on transcriptional level by means of qPCR and sequencing. The defect might occur during protein folding resulting in a misfolding event of the mutant Lmx1b versions leading to a rapid protein degradation. In the following, the protein stability of LMX1B (H54L), LMX1B (C95F) mutants was further examined in cell culture.

Contrary to these results, the group of (Cross *et al.* 2014) published a mouse model carrying the amino acid substitution V242D in the homeodomain of Lmx1b. This novel mouse mutant *Lmx1b Icst* was generated by N-ethyl-N-nitrosourea-induction. The author argues for a dominant-negative effect due to the glaucomatous eye defects, kidney failure and semi-lethality of heterozygous *Lmx1b Icst* mutant mice. This mouse model is a rare example that reflects the pathologic mode of action in humans. Nevertheless, there are discrepancies in the interpretation of the mode of action of mutant LMX1B in nail-patella syndrome.

4.2 The mutant proteins LMX1B (H54L) and LMX1B (C95F) show a reduced half-life compared to LMX1B (WT)

It is discussed that the disease nail-patella syndrome is caused in humans by haploinsufficiency of *LMX1B*. The molecular mechanisms behind the rare disorder are still poorly understood. Since mutations responsible for nail-patella syndrome are mainly located in the functional domains of *LMX1B*, mutation c.161A>C in LIM 1 and c.277-285 [AGCGGCTGC>TCCGGATTC] in LIM 2 were further analyzed to clarify the disease progression. Recent data of the *Lmx1b* knock-in mouse model suggest a possible protein degradation of mutant Lmx1b (H54L) and Lmx1b (C95F) proteins. Based on these results, the half-life of LMX1B (WT), LMX1B (H54L), and LMX1B (C95F) proteins was determined by a cycloheximide chase assay in cell culture. Considering that the half-life drops from ~4 hours for the LMX1B wild-type to ~1.5 hours for LMX1B (H54L) and ~45 minutes for LMX1B (C95F) mutant proteins, it is reasonable to suggest that the mutant LMX1B variants are expressed in cells but are degraded faster than the wild-type. These results provide the simple explanation, why it was not possible to verify the mutant Lmx1b proteins in Lmx1b knock-in mice by means of immunofluorescence. Lmx1b (H54L) as well as Lmx1b (C95F) are certainly expressed *in vivo*, but the podocytes potentially recognize mutant proteins as a failure resulting in a rapid elimination. Due to the amino acid substitutions, it might be quite possible that the mutant protein gets misfolded. On that account, it has already been reported that mis- or unfolded proteins are usually processed by cellular degradation pathways (Knecht *et al.* 2009). To find out whether this is true for the mutant proteins LMX1B (H54L) and LMX1B (C95F), the precise degradation pathway of LMX1B was investigated by further *in vitro* experiments.

4.3 The protein degradation of LMX1B is processed by the proteasome pathway

By use of the cycloheximide chase assay, the protein half-life of LMX1B (WT), LMX1B (H54L), and LMX1B (C95F) was determined. In a next step, the appropriate degradation pathway was ascertained by application of respective inhibitors. It could be shown that the degradation of the LMX1B wild-type and mutant proteins is processed by the proteasomal instead of the lysosomal pathway. Indeed, MG-132 does not completely block protein degradation, thus suggesting that other proteolytic pathways could contribute to the LMX1B turnover, as already proposed for other proteins (Fuertes *et al.* 2003). Remarkably, bortezomib, another proteasome inhibitor that is described to block more specific, preserved LMX1B wild-type and the mutant proteins more efficiently from degradation process. Quite instructive were the results after application of a lysosomal inhibitor. There was no effect concerning the protein degradation level for both LMX1B wild-type protein, as well as LMX1B (H54L) and LMX1B (C95F) mutants. Various proteasomal inhibitors have been generated for different purposes comprising research and therapeutic application. In experimental models, previous studies validated curative effects of proteasome inhibitors during renal injury by decreasing proliferation and inflammation due to the reduced activation of the pro-inflammatory NF-κB pathway (Meyer-Schwesinger 2019). However, an application of proteasome inhibitors needs to be carefully assessed for treatment of renal diseases caused by deficient LMX1B. Their use in the same context can evoke renal injury due to oxidative stress or preventing the removal of damaged protein thus further stressing renal cells. The proteasome inhibitor bortezomib is already in clinical use for treatment of multiple myeloma as a chemotherapeutic substance (Kubiczkova *et al.* 2014). Bortezomib reversibly blocks the chymotrypsin-like activity (β5 subunit) of the 20S core complex of the proteasome. Furthermore, rare detrimental effects in the kidney were reported for bortezomib referring to a beneficial influence during renal disease (Merin & Kelly 2014). An application of bortezomib might show curative effects or even prevent nail-patella syndrome patients from renal injury. Therefore, the therapeutic approach of bortezomib should be further tested *in vivo*.

In general, proteins to be degraded are previously marked by ubiquitin molecules. Despite the majority of protein turnover is mediated through the canonical ubiquitin-dependent pathway, there are various examples of proteasomal degradation that occur without prior ubiquitination (Singh Gautam *et al.* 2012). Since this could not be verified for LMX1B (data not shown), it is possible that LMX1B is ubiquitin-independently degraded by the proteasome as for example apomyoglobin (Singh Gautam *et al.* 2012). As one might expect, the molecular weight of LMX1B would have to rise after application of the proteasomal inhibitor due to poly-ubiquitin tagging. But this was not the case, also see 3.2.4. Examples of 20S-mediated ubiquitin-independent degradation comprise structurally abnormal and misfolded, proteins (Ben-Nissan & Sharon 2014) as it is assumed for LMX1B (H54L) and LMX1B (C95F).

4.4 The mutant protein LMX1B (V242D) shows an increased stability compared to LMX1B (WT) and is also degraded by the proteasomal pathway

The group of (Cross *et al.* 2014) reported a mouse model carrying an amino acid substitution V242D in the homeodomain of Lmx1b. The author argues for a dominant-negative effect due to the glaucomatous eye defects, kidney failure and semi-lethality of heterozygous *Lmx1b Icst* mutant mice. This mouse model is a rare example that resemble the defects found in human nail-patella syndrome patients with the same pattern of inheritance. The mode of action of mutant LMX1B in nail-patella syndrome is yet not understood. As discussed in the previous chapter, mutations occurring in the LIM domains lead to a reduced protein half-life. Since the phenotypes of the *Lmx1b* (H54L), *Lmx1b* (C95F) knock-in and the *Lmx1b Icst* mice appear quite diverse, in the following the half-life of the mutant LMX1B (V242D) protein was ascertained *in vitro*. Surprisingly, these data revealed an increased stability of the LMX1B (V242D) protein compared to LMX1B (WT). According to the degradation pathway of LMX1B in general, it could be shown that the LMX1B (V242D) is also abolished by the proteasome. The maintenance of intracellular proteostasis is based on the correct functioning of complex co-translational mechanisms to determine the fate of proteins, a process often referred

to as ‘protein quality control’ (Wang & Terpstra 2013). Both protein and mRNA half-lives are known to be strictly regulated. Usually, genes with crucial cell functions have both stable mRNAs and proteins while transcription factors tend to have unstable mRNAs and proteins. Furthermore, abundant and well-structured proteins are more stable than less-structured proteins (Schwanhäusser *et al.* 2011). Under the experimental conditions, the LMX1B (V242D) protein behaved as a more stable-protein with a half-life to be more than twice as high as the half-life of the wild-type protein. In this light, the phenotype of the *Lmx1b Icst* mutant mice matched the half-life results due to the pathogenic influence of the dominant-negative effect of LMX1B (V242D). Potentially, the amino acid substitution from a valine to an aspartate results in a highly structured protein whereby the functionality of the transcription factor LMX1B is reinforced. For this purpose, the tertiary protein structure was figured out to better understand the results of the reported *Lmx1b Icst* mutant mice phenotype in liaison with the protein half-life.

4.5 LMX1B (H54L) and LMX1B (C95F) mutants result in a protein instability, LMX1B (V242D) evokes a stronger DNA binding

LIM homeobox genes are one of the most important subfamilies of homeobox genes encoding LIM-homeodomain (LIM-HD) proteins. These proteins feature particularly two LIM domains in their amino termini and centrally located the homeodomain which is used to interact with specific DNA elements in target genes. Multiple studies have reported their fundamental roles during development in various organisms. The LIM domain is named by the initials and firstly described three homeodomain proteins Lin-11, Isl-1 and Mec-3 (Karlsson *et al.* 1990; Freyd *et al.* 1990). LIM motifs contain two tandemly-repeated, cysteine-rich, double-zinc binding domains that can be recognized by a number of co-factors mediating LIM-HD functions (Dawid *et al.* 1998; Jurata & Gill 1998). The transcription factor LMX1B belongs to the LIM-homeodomain protein family that harbors two LIM domains (LIM 1 and LIM 2), distinguished by characteristic patterns of conserved amino acids. The LIM 1 domain is located NH_2-terminal to the LIM 2 domain and both coordinate two zinc ions, respectively (Vollrath *et al.* 1998). The data from cell culture (3.2) demonstrated that LMX1B (H54L) and LMX1B (C95F) are faster degraded by the

proteasome compared to LMX1B (WT) and LMX1B (V242D). To figure out, whether the amino acid substitution results in an anomalous 3D protein structure, a homology modeling of the mutant LMX1B versions was carried out for expounding and reconstructing the tertiary protein structure. H54L within the LIM 1 domain as well as the C95F in the LIM 2 domain of LMX1B occurred in the zinc binding motifs (Bongers *et al.* 2002) resulting in a failed zinc ion coordination. Due to the loss of the zinc ion in LIM 1 or LIM 2, the NH_2-terminal loop of LMX1B protein cannot be formed, finally resulting in a misfolded protein followed by a rapid degradation via the proteasome. Previously published in literature, metal ions are known to stabilize tertiary conformations of proteins, participate in catalysis in certain metalloenzymes and induce changes in protein structure (Michelsen *et al.* 1993). For example, the zinc-finger structures of the transcription factor GAL4 including binuclear zinc sites or the zinc center in the steroid hormone receptor domain, are dependent on zinc to stabilize their tertiary folds (Kraulis *et al.* 1992; Marmorstein *et al.* 1992; Lee *et al.* 1989; Luisi *et al.* 1991). In a metaphorical sense, the zinc coordination may likewise play an essential role in stabilizing the tertiary structure of the LIM domains in LMX1B to generate a binding interface for protein-protein interactions. A loss of the zinc ion results in a complete LMX1B removal by the proteasome.

The homeodomain of LMX1B lies C-terminal followed by the transactivation domain (Bongers *et al.* 2002). The homeodomain was originally identified in transcription factors of the fly *Drosophila melanogaster* and is a 60 amino acid helix-turn-helix DNA-binding domain encoded by the so-called "*homeobox*" (Scott & Weiner 1984; Gehring *et al.* 1994). The homeodomain is very highly conserved and comprises three α helical regions folded into a tight globular structure that binds to 5'-TAAT-3' rich sequences, also known as FLAT elements (German *et al.* 1992; Gehring *et al.* 1994). The recognition helix within the homeodomain is positioned in the major groove of the DNA, roughly in parallel to the groove at the point where most of the specific intermolecular contacts take place. In addition to strengthen the binding, the amino-terminal arm of the homeodomain interacts with the DNA minor groove (Bürglin & Affolter 2016). Nonetheless, instead of the valine, the aspartate seems to induce a crucial effect in DNA binding. Due to the coordination of the adenine and thymine at the major groove of the DNA, the aspartate facilitates a reinforced binding of LMX1B (V242D) to the DNA. As a consequence, the dominant-negative effect published by the group (Cross *et al.* 2014) is plausible.

4.6 Bortezomib as a potential therapeutic target in nail-patella syndrome

The ubiquitin-proteasome system turned out to be of high importance during physiological processes along the entire nephron. Including the regulation of erythropoietin (Kaelin 2002), glucose transport (Pioli & Rigby 2001), salt and water homeostasis (Ronzaud & Staub 2014; Wu *et al.* 2018), the focus is upon the ubiquitin-proteasome activity as a crucial determinant of glomerular cell phenotypes and differentiation status (Rinschen *et al.* 2016b). Especially in podocytes and parietal cells of the glomerulus, this system has been described to play a major part (Schroeter *et al.* 2018). In parietal epithelial cells, podocyte-specific proteins, which are permanently synthesized, are removed by proteasomal decay (Guhr *et al.* 2013). In order to maintain the podocyte identity, the ubiquitin-proteasome system regulates the levels of podocyte-specific proteins such as actin-binding proteins α-actinin 4 and synaptopodin (Asanuma *et al.* 2006), the transcription factor WT1 (Gebeshuber *et al.* 2013), the stomatin family member podocin, the slit diaphragm protein nephrin (Rinschen *et al.* 2016a), the adapter protein NCK1 (Buvall *et al.* 2013), and the protein kinase Cλ (Okuda *et al.* 2001). Consequently, the podocyte gene transcription, actin dynamics, mechanosensation, endocytosis, and slit diaphragm architecture is influenced by the proteasome system (Figure 4.1, [A]).

Previous studies showed an involvement of the ubiquitin-proteasome system in the development of glomerular injury (Figure 4.1, [B]). Several renal diseases such as crescent glomerulonephritis, membranous nephropathy, and focal segmental glomerular sclerosis are caused by a disturbed ubiquitin-proteasome system. These findings emphasize the importance of a proper function in addition to a fine-tuned regulation of physiological processes by the ubiquitin-proteasome system in the kidney, which in turn influence the whole organism.

[A]

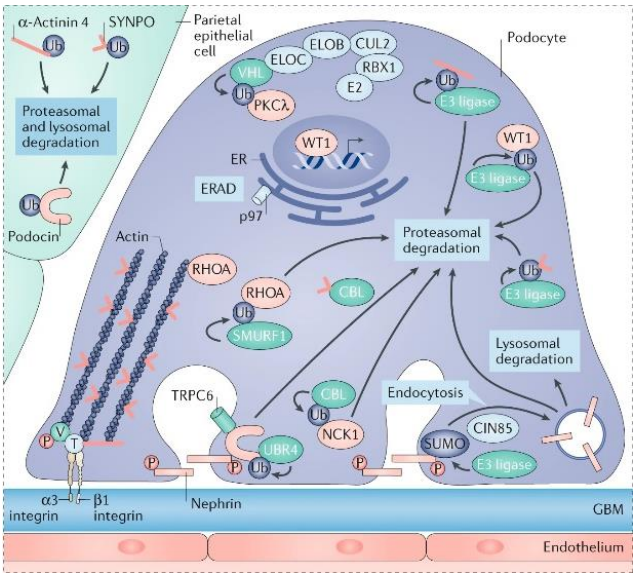

[B]

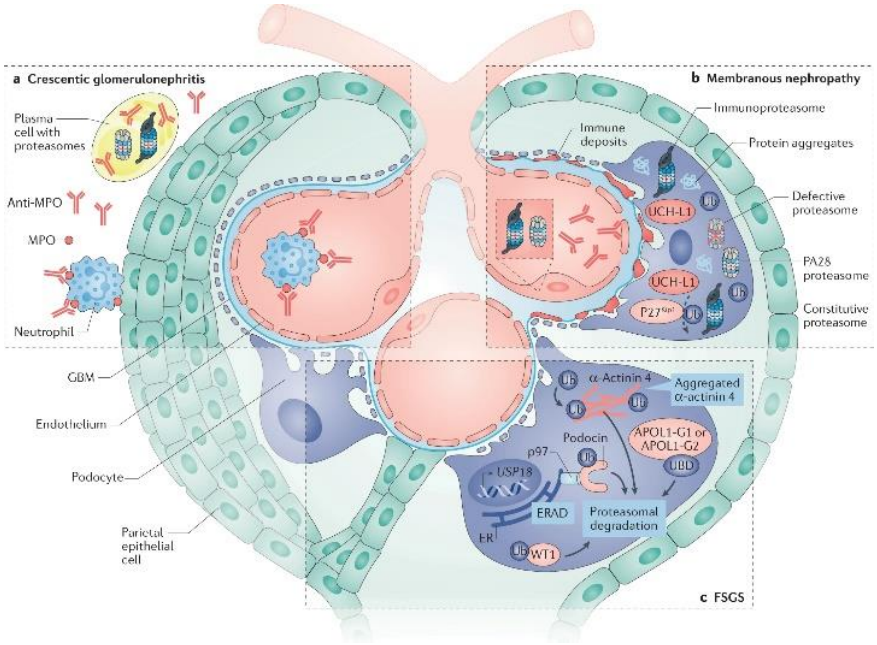

Figure 4.1: Model of the ubiquitin-proteasome system in the glomerulus.
[A] The ubiquitin-proteasome system in a healthy glomerulus. The ubiquitin-proteasome system maintains the glomerular cell-specific proteome. **[B]** The ubiquitin-proteasome system in glomerular pathology. Abbreviations: (SYNPO), synaptopodin; (WT1), transcription factor Wilms tumor 1; (NCK1), adapter protein NCK1; (PKCλ), protein kinase Cλ; (CUL2), cullin 2; (ELO), elongin; (ERAD), ER-associated degradation; (GBM) glomerular basement membrane; (P), phosphorylation; (SMURF), SMAD-ubiquitylation regulatory factor 1; (TRPC6), transient receptor potential channel 6 (Meyer-Schwesinger 2019).

Dysfunction of the ubiquitin-proteasome pathway is related to a variety of human disorders either due to reduced or increased ubiquitination of target proteins. Different steps of the UPS represent targets for recently developed drugs for the treatment of human neoplasms and other conditions (Moore *et al.* 2008). The proteasome inhibitor MG-132 acts at the chymotrypsin-like site of the proteasome similar to the clinically approved proteasome inhibitor bortezomib (PS-341) (Goldberg 2012). Proteasome inhibitors could theoretically restore the levels of mutant proteins as it has recently proposed for the protein menin (Canaff *et al.* 2012). Since mutant LIM proteins are degraded by the proteasome, presumably without a previous ubiquitination, the stabilization of the protein might show a therapeutic approach for treating nail-patella syndrome patients. However, the effects of these drugs include the regulation of multiple pathways implicated in tumorigenesis, and therefore this possible application should be explored in depth in preclinical studies (Hernández-Ramírez *et al.* 2016). The current project we are still working on, is the test of bortezomib as a drug in multiple transgenic mice in terms of the nail-patella syndrome mutants LMX1B (H54L) and LMX1B (C95F). Based on the profound results we received from the cell culture experiments, the protein levels of the LMX1B (H54L) and LMX1B (C95F) proteins could be restored after application of the proteasomal inhibitors MG-132 or PS-341. It would be interesting to know, whether it is possible to stabilize the mutant proteins, either Lmx1b (H54L) or Lmx1b (C95F) in adult mice after deletion of one *Lmx1b* copy by an induced Cre recombinase activity. Therefore, the *Lmx1b* recombination was induced for seven consecutive days by a doxycycline solution via the drinking water. Every other day, mice were weighed, intraperitoneally injected with bortezomib at a dose of 0.3 µg/g of body weight and at the same time, spot urine was collected for examination of proteinuria. Preliminary data revealed a potential preventive effect on proteinuria after treatment with the proteasome inhibitor bortezomib. Further experiments need to be performed for verification of the instructive first results.

.

5. Summary

Different mutations in *LMX1B* cause the hereditary disease nail-patella syndrome (Bongers *et al.* 2002). Many of the patients suffer from renal symptoms which finally defines their prognosis. But still the precise way of disease progression is broadly unexplored. For this purpose, an appropriate tool was needed to understand the disease development. The generation of the conventional *Lmx1b* knock-out mouse was the first model revealing many structural and molecular changes due to the Lmx1b deficiency. Consistent to human nail-patella syndrome patients, in homozygous *Lmx1b* knock-out mice, abnormalities of the eyes, limbs, and the renal structures could be investigated. Nevertheless, the research on the conventional *Lmx1b* knock-out mouse was rather limited since the mode of inheritance in mice does not correspond to humans. By implementation of the podocyte-specific *Lmx1b* knock-out mouse, a more detailed analysis of the structural changes in the kidney was achieved. In addition to the loss of podocyte foot processes those mice died after 14 days and were not suitable for further research on the function of Lmx1b in advanced age. In a further course, the inducible podocyte-specific *Lmx1b* knock-out mouse line with an *mTmG* reporter construct was generated. In this way, the knock- out of *Lmx1b* could be induced at a desired time point in mature podocytes of adult mice. Analysis of those mice revealed that Lmx1b is important for the maintenance of podocyte structures since a loss of Lmx1b results in a dysregulated actin cytoskeleton (Setzer 2020). So far, the puzzling phenomena concerns the fact that in humans nail-patella syndrome is inherited in an autosomal dominant fashion, but heterozygous *Lmx1b* knock-out mice do not develop a phenotype. In literature, it is described that the disease originates by haploinsufficiency of *LMX1B*. A dominant-negative effect in humans, could not be excluded, since the mode of inheritance in humans and mice vary widely. This still prompts the question what is the precise pathogenic mechanism of nail-patella syndrome? The main goal of this thesis was to clarify the molecular mechanism of disease progression of nail-patella syndrome.

Lmx1b knock-in mouse mutants, *Lmx1b* (H54L) and *Lmx1b* (C95F), which mimic the mutations found in the LIM domains of LMX1B of patients, were systematically analyzed, and give an insight whether we are dealing with haploinsufficiency or with other effects. Remarkably, heterozygous *Lmx1b* knock-in mice were healthy and showed no obvious phenotype regarding the kidney, skull, and skeleton. Surprisingly, only homozygous *Lmx1b* knock-in mice developed a nail-patella syndrome resembling phenotype. Indeed, the mutated mRNA of homozygous *Lmx1b* knock-in mice was proven by qPCR, but the mutant Lmx1b proteins were not detectable in podocytes by immunofluorescence. Consequently, a cell-specific LIM domain function could not be detected because the implemented *Lmx1b* knock- in mutations resulted in a loss-of-function effect.

Since the mRNA transcript in homozygous *Lmx1b* knock- in mice was verified, it was out of all reason why the protein could not be detected. Therefore, the half-life of LMX1B (H54L) and LMX1B (C95F) was examined to clarify the stability of mutant LMX1B proteins. Interestingly, the mutant LMX1B (H54L) and LMX1B (C95F) proteins showed a reduced half-life compared to wild-type LMX1B. Due to the amino acid change in the respective LIM domain of LMX1B, it is feasible that those versions are misfolded followed by a subsequent degradation in the cell. This phenomenon was confirmed in closer consideration of the LMX1B degradation pathway. By application of the proteasomal inhibitor bortezomib, PS- 341, the levels of the mutant LMX1B proteins could be efficiently stabilized. In contrast to this effect, a mouse model with a mutation in the homeobox of *Lmx1b* coding for LMX1B (V242D) was described to show a dominant-negative effect (Cross *et al.* 2014). In accordance with the examination of the stability of the mutant proteins LMX1B (H54L) and LMX1B (C95F), it was interesting to investigate the behavior of the mutant protein LMX1B (V242D). This mutant LMX1B protein showed an increased stability compared to the wild-type LMX1B protein but was also degraded by the proteasome. Taken together, these first results indicated that the pathogenic mechanism of nail-patella syndrome might depend on the nature of mutation in *LMX1B*.

To answer the question whether there are internal structural changes in mutant LMX1B protein versions, the 3D structure was additionally analyzed by homology modeling confirming the data of cell culture assays. The amino acid substitution H54L and C95F within the LIM domains resulted in an instable 3D structure due to the failed zinc ion coordination explaining the reduced half-life of mutant proteins LMX1B (H54L) and LMX1B (C95F), thus confirming the loss-of-function effect in *Lmx1b* knock-in mice. In addition, the 3D structure, and the surface potential of the mutant LMX1B (V242D) protein clearly stated an altered surface charge benefitting the binding to the major groove of the DNA. Thus, the enhanced half-life and the stronger DNA binding of the mutant LMX1B (V242D) protein fit into the concept of the dominant-negative effect of reported *Lmx1b Icst* mutant mice (Cross *et al.* 2014).

Finally, since it was shown that mutant proteins LMX1B (H54L) and LMX1B (C95F) can be stabilized in cell culture, it was interesting to know whether an application of the proteasome inhibitor bortezomib shows a curative effect on proteinuria in the inducible podocyte-specific compound heterozygous *Lmx1b* mice. Remarkably, first results showed an attenuation of excreted protein level of inducible podocyte-specific compound heterozygous *Lmx1b* $^{C95F/lox}$ mice after treatment with the proteasome inhibitor bortezomib.

Altogether, the present study gave some new memorable results on the topic *Lmx1b* mutations leading to nail-patella syndrome. Based on the profound results, it seems to be very likely that the pathogenic mechanism of nail-patella syndrome relies on the nature of mutation in *LMX1B*. Examined mutations occurring within the LIM domains predominantly result in a loss of function requiring an adjusted therapeutic treatment. Analysis of the mutation located in the homeobox of *Lmx1b* revealed a dominant-negative effect in mice and presumably requires a different therapy, for instance knock-down of the mutant LMX1B (V242D) mRNA. In future studies, the efficacy of the already practically used proteasome inhibitor bortezomib should be further tested and might pave the way for a potential therapeutic approach of nail-patella syndrome.

6. References

Abrahamson, D.R. (1985). Origin of the glomerular basement membrane visualized after in vivo labeling of laminin in newborn rat kidneys. *The Journal of cell biology*, 100, 1988–2000.

Adams, K.A., Maida, J.M., Golden, J.A. & Riddle, R.D. (2000). The transcription factor Lmx1b maintains Wnt1 expression within the isthmic organizer. *Development (Cambridge, England)*, 127, 1857–1867.

Andrews, P.M. & Bates, S.B. (1984). Filamentous actin bundles in the kidney. *The Anatomical record*, 210, 1–9.

Asanuma, K., Kim, K., Oh, J., Giardino, L., Chabanis, S. & Faul, C. *et al.* (2005). Synaptopodin regulates the actin-bundling activity of alpha-actinin in an isoform-specific manner. *The Journal of clinical investigation*, 115, 1188–1198.

Asanuma, K., Yanagida-Asanuma, E., Faul, C., Tomino, Y., Kim, K. & Mundel, P. (2006). Synaptopodin orchestrates actin organization and cell motility via regulation of RhoA signalling. *Nature cell biology*, 8, 485–491.

Avasthi, P.S., Evan, A.P. & Hay, D. (1980). Glomerular endothelial cells in uranyl nitrate-induced acute renal failure in rats. *The Journal of clinical investigation*, 65, 121–127.

Baker, K.E. & Parker, R. (2004). Nonsense-mediated mRNA decay: terminating erroneous gene expression. *Current opinion in cell biology*, 16, 293–299.

Ballermann, B.J. (2005). Glomerular endothelial cell differentiation. *Kidney international*, 67, 1668–1671.

Ben-Nissan, G. & Sharon, M. (2014). Regulating the 20S proteasome ubiquitin-independent degradation pathway. *Biomolecules*, 4, 862–884.

Bhattacharya, D., Mukhopadhyay, M., Bhattacharyya, M. & Karmakar, P. (2018). Is autophagy associated with diabetes mellitus and its complications? A review. *EXCLI journal*, 17, 709–720.

Bongers, E.M., Wijs, I.J. de, Marcelis, C., Hoefsloot, L.H. & Knoers, N.V. (2008). Identification of entire LMX1B gene deletions in nail patella syndrome: evidence for haploinsufficiency as the main pathogenic mechanism underlying dominant inheritance in man. *European journal of human genetics : EJHG*, 16, 1240–1244.

Bongers, E.M.H.F., Gubler, M.-C. & Knoers, N.V.A.M. (2002). Nail-patella syndrome. Overview on clinical and molecular findings. *Pediatric nephrology (Berlin, Germany)*, 17, 703–712.

Bongers, E.M.H.F., Huysmans, F.T., Levtchenko, E., Rooy, J.W. de, Blickman, J.G. & Admiraal, R.J.C. *et al.* (2005). Genotype-phenotype studies in nail-patella syndrome show that LMX1B mutation location is involved in the risk of developing nephropathy. *European journal of human genetics : EJHG*, 13, 935–946.

Boute, N., Gribouval, O., Roselli, S., Benessy, F., Lee, H. & Fuchshuber, A. *et al.* (2000). NPHS2, encoding the glomerular protein podocin, is mutated in autosomal recessive steroid-resistant nephrotic syndrome. *Nature genetics*, 24, 349–354.

Bradford, M.M. (1976). A rapid and sensitive method for the quantitation of microgram quantities of protein utilizing the principle of protein-dye binding. *Analytical Biochemistry*, 72, 248–254.

Burghardt, T., Hochapfel, F., Salecker, B., Meese, C., Gröne, H.-J. & Rachel, R. *et al.* (2015). Advanced electron microscopic techniques provide a deeper insight into the peculiar features of podocytes. *American journal of physiology. Renal physiology*, 309, F1082-9.

Burghardt, T., Kastner, J., Suleiman, H., Rivera-Milla, E., Stepanova, N. & Lottaz, C. *et al.* (2013). LMX1B is essential for the maintenance of differentiated podocytes in adult kidneys. *Journal of the American Society of Nephrology : JASN*, 24, 1830–1848.

Bürglin, T.R. & Affolter, M. (2016). Homeodomain proteins: an update. *Chromosoma*, 125, 497–521.

Bustin, S.A. (2000). Absolute quantification of mRNA using real-time reverse transcription polymerase chain reaction assays. *Journal of molecular endocrinology*, 25, 169–193.

Buvall, L., Rashmi, P., Lopez-Rivera, E., Andreeva, S., Weins, A. & Wallentin, H. *et al.* (2013). Proteasomal degradation of Nck1 but not Nck2 regulates RhoA activation and actin dynamics. *Nature communications*, 4, 2863.

Canaff, L., Vanbellinghen, J.-F., Kanazawa, I., Kwak, H., Garfield, N. & Vautour, L. *et al.* (2012). Menin missense mutants encoded by the MEN1 gene that are targeted to the proteasome: restoration of expression and activity by CHIP siRNA. *The Journal of clinical endocrinology and metabolism*, 97, E282-91.

Cesario, J.M., Landin Malt, A., Chung, J.U., Khairallah, M.P., Dasgupta, K. & Asam, K. *et al.* (2018). Anti-osteogenic function of a LIM-homeodomain transcription

factor LMX1B is essential to early patterning of the calvaria. *Developmental biology*, 443, 103–116.

Chen, H., Lun, Y., Ovchinnikov, D., Kokubo, H., Oberg, K.C. & Pepicelli, C.V. *et al.* (1998a). Limb and kidney defects in Lmx1b mutant mice suggest an involvement of LMX1B in human nail patella syndrome. *Nature genetics*, 19, 51–55.

Chen, H., Ovchinnikov, D., Pressman, C.L., Aulehla, A., Lun, Y. & Johnson, R.L. (1998b). Multiple calvarial defects in lmx1b mutant mice. *Developmental genetics*, 22, 314–320.

Chew, C. & Lennon, R. (2018). Basement Membrane Defects in Genetic Kidney Diseases. *Frontiers in pediatrics*, 6, 11.

Choi, H.J., Lee, B.H., Kang, J.H., Jeong, H.J., Moon, K.C. & Ha, I.S. *et al.* (2008). Variable phenotype of Pierson syndrome. *Pediatric nephrology (Berlin, Germany)*, 23, 995–1000.

Ciani, L., Patel, A., Allen, N.D. & ffrench-Constant, C. (2003). Mice lacking the giant protocadherin mFAT1 exhibit renal slit junction abnormalities and a partially penetrant cyclopia and anophthalmia phenotype. *Molecular and cellular biology*, 23, 3575–3582.

Conti, S., Perico, L., Grahammer, F. & Huber, T.B. (2017). The long journey through renal filtration: new pieces in the puzzle of slit diaphragm architecture. *Current opinion in nephrology and hypertension*, 26, 148–153.

Cross, S.H., Macalinao, D.G., McKie, L., Rose, L., Kearney, A.L. & Rainger, J. *et al.* (2014). A dominant-negative mutation of mouse Lmx1b causes glaucoma and is semi-lethal via LDB1-mediated dimerization corrected. *PLoS genetics*, 10, e1004359.

Dai, J.-X., Johnson, R.L. & Ding, Y.-Q. (2009). Manifold functions of the Nail-Patella Syndrome gene Lmx1b in vertebrate development. *Development, growth & differentiation*, 51, 241–250.

Dawid, I.B., Breen, J.J. & Toyama, R. (1998). LIM domains: multiple roles as adapters and functional modifiers in protein interactions. *Trends in genetics : TIG*, 14, 156–162.

Ding, Y.-Q., Marklund, U., Yuan, W., Yin, J., Wegman, L. & Ericson, J. *et al.* (2003). Lmx1b is essential for the development of serotonergic neurons. *Nature neuroscience*, 6, 933–938.

Dong, Y., Skoultchi, A.I. & Pollard, J.W. (1993). Efficient DNA transfection of quiescent mammalian cells using poly-L-ornithine. *Nucleic acids research*, 21, 771–772.

Donoviel, D.B., Freed, D.D., Vogel, H., Potter, D.G., Hawkins, E. & Barrish, J.P. *et al.* (2001). Proteinuria and perinatal lethality in mice lacking NEPH1, a novel protein with homology to NEPHRIN. *Molecular and cellular biology*, 21, 4829–4836.

Drenckhahn, D. & Franke, R.P. (1988). Ultrastructural organization of contractile and cytoskeletal proteins in glomerular podocytes of chicken, rat, and man. *Laboratory investigation; a journal of technical methods and pathology*, 59, 673–682.

Dreyer, S.D., Morello, R., German, M.S., Zabel, B., Winterpacht, A. & Lunstrum, G.P. *et al.* (2000). LMX1B transactivation and expression in nail-patella syndrome. *Human molecular genetics*, 9, 1067–1074.

Dreyer, S.D., Zhou, G., Baldini, A., Winterpacht, A., Zabel, B. & Cole, W. *et al.* (1998). Mutations in LMX1B cause abnormal skeletal patterning and renal dysplasia in nail patella syndrome. *Nature genetics*, 19, 47–50.

Dunston, J.A., Hamlington, J.D., Zaveri, J., Sweeney, E., Sibbring, J. & Tran, C. *et al.* (2004). The human LMX1B gene: transcription unit, promoter, and pathogenic mutations. *Genomics*, 84, 565–576.

Dunston, J.A., Reimschisel, T., Ding, Y.-Q., Sweeney, E., Johnson, R.L. & Chen, Z.-F. *et al.* (2005). A neurological phenotype in nail patella syndrome (NPS) patients illuminated by studies of murine Lmx1b expression. *European journal of human genetics : EJHG*, 13, 330–335.

Durbeej, M., Henry, M.D., Ferletta, M., Campbell, K.P. & Ekblom, P. (1998). Distribution of dystroglycan in normal adult mouse tissues. *The journal of histochemistry and cytochemistry : official journal of the Histochemistry Society*, 46, 449–457.

el Ghouzzi, V., Le Merrer, M., Perrin-Schmitt, F., Lajeunie, E., Benit, P. & Renier, D. *et al.* (1997). Mutations of the TWIST gene in the Saethre-Chotzen syndrome. *Nature genetics*, 15, 42–46.

El-Aouni, C., Herbach, N., Blattner, S.M., Henger, A., Rastaldi, M.P. & Jarad, G. *et al.* (2006). Podocyte-specific deletion of integrin-linked kinase results in severe

glomerular basement membrane alterations and progressive glomerulosclerosis. *Journal of the American Society of Nephrology : JASN*, 17, 1334–1344.

Emsley, P. & Cowtan, K. (2004). Coot: model-building tools for molecular graphics. *Acta crystallographica. Section D, Biological crystallography*, 60, 2126–2132.

Endele, S., Klein, S., Richter, S., Molter, T., Amann, K. & Klanke, B. *et al.* (2007). Renal phenotype in heterozygous Lmx1b knockout mice (Lmx1b+/-) after unilateral nephrectomy. *Transgenic research*, 16, 723–729.

Eremina, V., Jefferson, J.A., Kowalewska, J., Hochster, H., Haas, M. & Weisstuch, J. *et al.* (2008). VEGF inhibition and renal thrombotic microangiopathy. *The New England journal of medicine*, 358, 1129–1136.

Ervasti, J.M. & Campbell, K.P. (1993). A role for the dystrophin-glycoprotein complex as a transmembrane linker between laminin and actin. *The Journal of cell biology*, 122, 809–823.

Farquhar, M.G. (2006). The glomerular basement membrane: not gone, just forgotten. *The Journal of clinical investigation*, 116, 2090–2093.

Faul, C., Asanuma, K., Yanagida-Asanuma, E., Kim, K. & Mundel, P. (2007). Actin up: regulation of podocyte structure and function by components of the actin cytoskeleton. *Trends in cell biology*, 17, 428–437.

Freyd, G., Kim, S.K. & Horvitz, H.R. (1990). Novel cysteine-rich motif and homeodomain in the product of the Caenorhabditis elegans cell lineage gene lin-11. *Nature*, 344, 876–879.

Fridén, V., Oveland, E., Tenstad, O., Ebefors, K., Nyström, J. & Nilsson, U.A. *et al.* (2011). The glomerular endothelial cell coat is essential for glomerular filtration. *Kidney international*, 79, 1322–1330.

Fuertes, G., Villarroya, A. & Knecht, E. (2003). Role of proteasomes in the degradation of short-lived proteins in human fibroblasts under various growth conditions. *The international journal of biochemistry & cell biology*, 35, 651–664.

Fujikake, N., Shin, M. & Shimizu, S. (2018). Association Between Autophagy and Neurodegenerative Diseases. *Frontiers in neuroscience*, 12, 255.

Gadd, M.S., Jacques, D.A., Nisevic, I., Craig, V.J., Kwan, A.H. & Guss, J.M. *et al.* (2013). A structural basis for the regulation of the LIM-homeodomain protein islet 1 (Isl1) by intra- and intermolecular interactions. *The Journal of biological chemistry*, 288, 21924–21935.

Gebeshuber, C.A., Kornauth, C., Dong, L., Sierig, R., Seibler, J. & Reiss, M. *et al.* (2013). Focal segmental glomerulosclerosis is induced by microRNA-193a and its downregulation of WT1. *Nature medicine*, 19, 481–487.

Gehring, W.J., Qian, Y.Q., Billeter, M., Furukubo-Tokunaga, K., Schier, A.F. & Resendez-Perez, D. *et al.* (1994). Homeodomain-DNA recognition. *Cell*, 78, 211–223.

George, B., Verma, R., Soofi, A.A., Garg, P., Zhang, J. & Park, T.-J. *et al.* (2012). Crk1/2-dependent signaling is necessary for podocyte foot process spreading in mouse models of glomerular disease. *The Journal of clinical investigation*, 122, 674–692.

German, M.S., Wang, J., Chadwick, R.B. & Rutter, W.J. (1992). Synergistic activation of the insulin gene by a LIM-homeo domain protein and a basic helix-loop-helix protein: building a functional insulin minienhancer complex. *Genes & development*, 6, 2165–2176.

Gibson, U.E., Heid, C.A. & Williams, P.M. (1996). A novel method for real time quantitative RT-PCR. *Genome research*, 6, 995–1001.

Goldberg, A.L. (2012). Development of proteasome inhibitors as research tools and cancer drugs. *The Journal of cell biology*, 199, 583–588.

Gossen, M. & Bujard, H. (1992a). Tight control of gene expression in mammalian cells by tetracycline-responsive promoters. *Proceedings of the National Academy of Sciences of the United States of America*, 89, 5547–5551.

Gossen, M. & Bujard, H. (1992b). Tight control of gene expression in mammalian cells by tetracycline-responsive promoters. *Proceedings of the National Academy of Sciences of the United States of America*, 89, 5547–5551.

Grahammer, F. (2017). New structural insights into podocyte biology. *Cell and tissue research*, 369, 5–10.

Grahammer, F., Schell, C. & Huber, T.B. (2013). The podocyte slit diaphragm--from a thin grey line to a complex signalling hub. *Nature reviews. Nephrology*, 9, 587–598.

Grahammer, F., Wigge, C., Schell, C., Kretz, O., Patrakka, J. & Schneider, S. *et al.* (2016). A flexible, multilayered protein scaffold maintains the slit in between glomerular podocytes. *JCI insight*, 1.

Gross, O., Beirowski, B., Harvey, S.J., McFadden, C., Chen, D. & Tam, S. *et al.* (2004). DDR1-deficient mice show localized subepithelial GBM thickening with focal loss of slit diaphragms and proteinuria. *Kidney international*, 66, 102–111.

Gross, O., Licht, C., Anders, H.J., Hoppe, B., Beck, B. & Tönshoff, B. *et al.* (2012). Early angiotensin-converting enzyme inhibition in Alport syndrome delays renal failure and improves life expectancy. *Kidney international*, 81, 494–501.

Guhr, S.S.O., Sachs, M., Wegner, A., Becker, J.U., Meyer, T.N. & Kietzmann, L. *et al.* (2013). The expression of podocyte-specific proteins in parietal epithelial cells is regulated by protein degradation. *Kidney international*, 84, 532–544.

Guo, C., Qiu, H.-Y., Shi, M., Huang, Y., Johnson, R.L. & Rubinstein, M. *et al.* (2008). Lmx1b-controlled isthmic organizer is essential for development of midbrain dopaminergic neurons. *The Journal of neuroscience : the official journal of the Society for Neuroscience*, 28, 14097–14106.

Heid, C.A., Stevens, J., Livak, K.J. & Williams, P.M. (1996). Real time quantitative PCR. *Genome research*, 6, 986–994.

Heidet, L., Bongers, E.M.H.F., Sich, M., Zhang, S.-Y., Loirat, C. & Meyrier, A. *et al.* (2003). In vivo expression of putative LMX1B targets in nail-patella syndrome kidneys. *The American journal of pathology*, 163, 145–155.

Hernández-Ramírez, L.C., Martucci, F., Morgan, R.M.L., Trivellin, G., Tilley, D. & Ramos-Guajardo, N. *et al.* (2016). Rapid Proteasomal Degradation of Mutant Proteins Is the Primary Mechanism Leading to Tumorigenesis in Patients With Missense AIP Mutations. *The Journal of clinical endocrinology and metabolism*, 101, 3144–3154.

Hershko, A., Ciechanover, A. & Varshavsky, A. (2000). Basic Medical Research Award. The ubiquitin system. *Nature medicine*, 6, 1073–1081.

Hiratani, I., Yamamoto, N., Mochizuki, T., Ohmori, S.-y. & Taira, M. (2003). Selective degradation of excess Ldb1 by Rnf12/RLIM confers proper Ldb1 expression levels and Xlim-1/Ldb1 stoichiometry in Xenopus organizer functions. *Development (Cambridge, England)*, 130, 4161–4175.

Hoekstra, E.J., Mesman, S., Munnik, W.A. de & Smidt, M.P. (2013). LMX1B is part of a transcriptional complex with PSPC1 and PSF. *PloS one*, 8, e53122.

Howard, T.D., Paznekas, W.A., Green, E.D., Chiang, L.C., Ma, N. & Ortiz de Luna, R.I. *et al.* (1997). Mutations in TWIST, a basic helix-loop-helix transcription factor, in Saethre-Chotzen syndrome. *Nature genetics*, 15, 36–41.

Huber, T.B., Kottgen, M., Schilling, B., Walz, G. & Benzing, T. (2001). Interaction with podocin facilitates nephrin signaling. *The Journal of biological chemistry*, 276, 41543–41546.

Huber, T.B., Schmidts, M., Gerke, P., Schermer, B., Zahn, A. & Hartleben, B. *et al.* (2003). The carboxyl terminus of Neph family members binds to the PDZ domain protein zonula occludens-1. *The Journal of biological chemistry*, 278, 13417–13421.

Jabs, E.W., Müller, U., Li, X., Ma, L., Luo, W. & Haworth, I.S. *et al.* (1993). A mutation in the homeodomain of the human MSX2 gene in a family affected with autosomal dominant craniosynostosis. *Cell*, 75, 443–450.

Jarad, G., Cunningham, J., Shaw, A.S. & Miner, J.H. (2006). Proteinuria precedes podocyte abnormalities inLamb2-/- mice, implicating the glomerular basement membrane as an albumin barrier. *The Journal of clinical investigation*, 116, 2272–2279.

Jarad, G. & Miner, J.H. (2009). Update on the glomerular filtration barrier. *Current opinion in nephrology and hypertension*, 18, 226–232.

Jarad, G., Pippin, J.W., Shankland, S.J., Kreidberg, J.A. & Miner, J.H. (2011). Dystroglycan does not contribute significantly to kidney development or function, in health or after injury. *American journal of physiology. Renal physiology*, 300, F811-20.

Jeansson, M. & Haraldsson, B. (2003). Glomerular size and charge selectivity in the mouse after exposure to glucosaminoglycan-degrading enzymes. *Journal of the American Society of Nephrology : JASN*, 14, 1756–1765.

Jiang, S., Zhang, J., Huang, D., Zhang, Y., Liu, X. & Wang, Y. *et al.* (2014). A microdeletion of chromosome 9q33.3 encompasses the entire LMX1B gene in a Chinese family with nail patella syndrome. *International journal of molecular sciences*, 15, 20158–20168.

Johnson, J.D., Zhang, W., Rudnick, A., Rutter, W.J. & German, M.S. (1997). Transcriptional synergy between LIM-homeodomain proteins and basic helix-loop-helix proteins: the LIM2 domain determines specificity. *Molecular and cellular biology*, 17, 3488–3496.

Jurata, L.W. & Gill, G.N. (1997). Functional analysis of the nuclear LIM domain interactor NLI. *Molecular and cellular biology*, 17, 5688–5698.

Jurata, L.W. & Gill, G.N. (1998). Structure and function of LIM domains. *Current topics in microbiology and immunology*, 228, 75–113.

Kaelin, W.G. (2002). How oxygen makes its presence felt. *Genes & development*, 16, 1441–1445.

Kalluri, R., van den Heuvel, L.P., Smeets, H.J., Schroder, C.H., Lemmink, H.H. & Boutaud, A. *et al.* (1995). A COL4A3 gene mutation and post-transplant anti-alpha 3(IV) collagen alloantibodies in Alport syndrome. *Kidney international*, 47, 1199–1204.

Kaplan, J.M., Kim, S.H., North, K.N., Rennke, H., Correia, L.A. & Tong, H.Q. *et al.* (2000). Mutations in ACTN4, encoding alpha-actinin-4, cause familial focal segmental glomerulosclerosis. *Nature genetics*, 24, 251–256.

Karlsson, O., Thor, S., Norberg, T., Ohlsson, H. & Edlund, T. (1990). Insulin gene enhancer binding protein Isl-1 is a member of a novel class of proteins containing both a homeo- and a Cys-His domain. *Nature*, 344, 879–882.

Kestilä, M., Lenkkeri, U., Männikkö, M., Lamerdin, J., McCready, P. & Putaala, H. *et al.* (1998). Positionally cloned gene for a novel glomerular protein--nephrin--is mutated in congenital nephrotic syndrome. *Molecular cell*, 1, 575–582.

Khandia, R., Dadar, M., Munjal, A., Dhama, K., Karthik, K. & Tiwari, R. *et al.* (2019). A Comprehensive Review of Autophagy and Its Various Roles in Infectious, Non-Infectious, and Lifestyle Diseases: Current Knowledge and Prospects for Disease Prevention, Novel Drug Design, and Therapy. *Cells*, 8.

Knecht, E., Aguado, C., Cárcel, J., Esteban, I., Esteve, J.M. & Ghislat, G. *et al.* (2009). Intracellular protein degradation in mammalian cells: recent developments. *Cellular and molecular life sciences : CMLS*, 66, 2427–2443.

Kobayashi, N. (2002). Mechanism of the process formation; podocytes vs. neurons. *Microscopy research and technique*, 57, 217–223.

Komander, D., Clague, M.J. & Urbé, S. (2009). Breaking the chains: structure and function of the deubiquitinases. *Nature reviews. Molecular cell biology*, 10, 550–563.

Kraulis, P.J., Raine, A.R., Gadhavi, P.L. & Laue, E.D. (1992). Structure of the DNA-binding domain of zinc GAL4. *Nature*, 356, 448–450.

Kriz, W. (2006). Biologie des Podozyten. *Nephrologe*, 1, 144–152.

Kriz, W. (2019). The Inability of Podocytes to Proliferate: Cause, Consequences, and Origin. *Anatomical record (Hoboken, N.J. : 2007)*.

Kriz, W., Shirato, I., Nagata, M., LeHir, M. & Lemley, K.V. (2013). The podocyte's response to stress: the enigma of foot process effacement. *American journal of physiology. Renal physiology*, 304, F333-47.

Kubiczkova, L., Pour, L., Sedlarikova, L., Hajek, R. & Sevcikova, S. (2014). Proteasome inhibitors - molecular basis and current perspectives in multiple myeloma. *Journal of cellular and molecular medicine*, 18, 947–961.

Larance, M., Ahmad, Y., Kirkwood, K.J., Ly, T. & Lamond, A.I. (2013). Global subcellular characterization of protein degradation using quantitative proteomics. *Molecular & cellular proteomics : MCP*, 12, 638–650.

Lausecker, F., Tian, X., Inoue, K., Wang, Z., Pedigo, C.E. & Hassan, H. *et al.* (2018). Vinculin is required to maintain glomerular barrier integrity. *Kidney international*, 93, 643–655.

Lea, P.J., Silverman, M., Hegele, R. & Hollenberg, M.J. (1989). Tridimensional ultrastructure of glomerular capillary endothelium revealed by high-resolution scanning electron microscopy. *Microvascular research*, 38, 296–308.

Lee, M.S., Gippert, G.P., Soman, K.V., Case, D.A. & Wright, P.E. (1989). Three-dimensional solution structure of a single zinc finger DNA-binding domain. *Science (New York, N.Y.)*, 245, 635–637.

Lennon, R., Byron, A., Humphries, J.D., Randles, M.J., Carisey, A. & Murphy, S. *et al.* (2014a). Global analysis reveals the complexity of the human glomerular extracellular matrix. *Journal of the American Society of Nephrology : JASN*, 25, 939–951.

Lennon, R., Randles, M.J. & Humphries, M.J. (2014b). The importance of podocyte adhesion for a healthy glomerulus. *Frontiers in endocrinology*, 5, 160.

Lenoir, O., Tharaux, P.-L. & Huber, T.B. (2016). Autophagy in kidney disease and aging: lessons from rodent models. *Kidney international*, 90, 950–964.

Luisi, B.F., Xu, W.X., Otwinowski, Z., Freedman, L.P., Yamamoto, K.R. & Sigler, P.B. (1991). Crystallographic analysis of the interaction of the glucocorticoid receptor with DNA. *Nature*, 352, 497–505.

Marini, M., Bocciardi, R., Gimelli, S., Di Duca, M., Divizia, M.T. & Baban, A. *et al.* (2010). A spectrum of LMX1B mutations in Nail-Patella syndrome: new point mutations, deletion, and evidence of mosaicism in unaffected parents. *Genetics in medicine : official journal of the American College of Medical Genetics*, 12, 431–439.

Marini, M., Giacopelli, F., Seri, M. & Ravazzolo, R. (2005). Interaction of the LMX1B and PAX2 gene products suggests possible molecular basis of differential phenotypes in Nail-Patella syndrome. *European journal of human genetics : EJHG*, 13, 789–792.

Marmorstein, R., Carey, M., Ptashne, M. & Harrison, S.C. (1992). DNA recognition by GAL4: structure of a protein-DNA complex. *Nature*, 356, 408–414.

Matejas, V., Hinkes, B., Alkandari, F., Al-Gazali, L., Annexstad, E. & Aytac, M.B. *et al.* (2010). Mutations in the human laminin beta2 (LAMB2) gene and the associated phenotypic spectrum. *Human mutation*, 31, 992–1002.

McIntosh, I., Dreyer, S.D., Clough, M.V., Dunston, J.A., Eyaid, W. & Roig, C.M. *et al.* (1998). Mutation analysis of LMX1B gene in nail-patella syndrome patients. *American journal of human genetics*, 63, 1651–1658.

Merin, N.M. & Kelly, K.R. (2014). Clinical use of proteasome inhibitors in the treatment of multiple myeloma. *Pharmaceuticals (Basel, Switzerland)*, 8, 1–20.

Meyer, H.-J. & Rape, M. (2014). Enhanced protein degradation by branched ubiquitin chains. *Cell*, 157, 910–921.

Meyer-Schwesinger, C. (2019). The ubiquitin-proteasome system in kidney physiology and disease. *Nature reviews. Nephrology*, 15, 393–411.

Michelsen, J.W., Schmeichel, K.L., Beckerle, M.C. & Winge, D.R. (1993). The LIM motif defines a specific zinc-binding protein domain. *Proceedings of the National Academy of Sciences of the United States of America*, 90, 4404–4408.

Mierzejewska, K., Siwek, W., Czapinska, H., Kaus-Drobek, M., Radlinska, M. & Skowronek, K. *et al.* (2014). Structural basis of the methylation specificity of R.DpnI. *Nucleic acids research*, 42, 8745–8754.

Miner, J.H., Go, G., Cunningham, J., Patton, B.L. & Jarad, G. (2006). Transgenic isolation of skeletal muscle and kidney defects in laminin beta2 mutant mice: implications for Pierson syndrome. *Development (Cambridge, England)*, 133, 967–975.

Miner, J.H., Morello, R., Andrews, K.L., Li, C., Antignac, C. & Shaw, A.S. *et al.* (2002). Transcriptional induction of slit diaphragm genes by Lmx1b is required in podocyte differentiation. *The Journal of clinical investigation*, 109, 1065–1072.

Mitch, W.E. & Goldberg, A.L. (1996). Mechanisms of muscle wasting. The role of the ubiquitin-proteasome pathway. *The New England journal of medicine*, 335, 1897–1905.

Miyazono, K.-i., Zhi, Y., Takamura, Y., Nagata, K., Saigo, K. & Kojima, T. *et al.* (2010). Cooperative DNA-binding and sequence-recognition mechanism of aristaless and clawless. *The EMBO journal*, 29, 1613–1623.

Mizushima, N., Noda, T., Yoshimori, T., Tanaka, Y., Ishii, T. & George, M.D. *et al.* (1998). A protein conjugation system essential for autophagy. *Nature*, 395, 395–398.

Moeller, M.J., Sanden, S.K., Soofi, A., Wiggins, R.C. & Holzman, L.B. (2003). Podocyte-specific expression of cre recombinase in transgenic mice. *Genesis (New York, N.Y. : 2000)*, 35, 39–42.

Moeller, M.J. & Tenten, V. (2013). Renal albumin filtration: alternative models to the standard physical barriers. *Nature reviews. Nephrology*, 9, 266–277.

Moore, B.S., Eustáquio, A.S. & McGlinchey, R.P. (2008). Advances in and applications of proteasome inhibitors. *Current opinion in chemical biology*, 12, 434–440.

Morello, R. & Lee, B. (2002). Insight into podocyte differentiation from the study of human genetic disease: nail-patella syndrome and transcriptional regulation in podocytes. *Pediatric research*, 51, 551–558.

Morello, R., Zhou, G., Dreyer, S.D., Harvey, S.J., Ninomiya, Y. & Thorner, P.S. *et al.* (2001). Regulation of glomerular basement membrane collagen expression by LMX1B contributes to renal disease in nail patella syndrome. *Nature genetics*, 27, 205–208.

Mundel, P., Reiser, J., Zúñiga Mejía Borja, A., Pavenstädt, H., Davidson, G.R. & Kriz, W. *et al.* (1997). Rearrangements of the cytoskeleton and cell contacts induce process formation during differentiation of conditionally immortalized mouse podocyte cell lines. *Experimental cell research*, 236, 248–258.

Muzumdar, M.D., Tasic, B., Miyamichi, K., Li, L. & Luo, L. (2007). A global double-fluorescent Cre reporter mouse. *Genesis (New York, N.Y. : 2000)*, 45, 593–605.

Nishioka, N., Nagano, S., Nakayama, R., Kiyonari, H., Ijiri, T. & Taniguchi, K. *et al.* (2005). Ssdp1 regulates head morphogenesis of mouse embryos by activating the Lim1-Ldb1 complex. *Development (Cambridge, England)*, 132, 2535–2546.

Noakes, P.G., Miner, J.H., Gautam, M., Cunningham, J.M., Sanes, J.R. & Merlie, J.P. (1995). The renal glomerulus of mice lacking s-laminin/laminin beta 2: nephrosis despite molecular compensation by laminin beta 1. *Nature genetics*, 10, 400–406.

Ohsumi, Y. (2014). Historical landmarks of autophagy research. *Cell research*, 24, 9–23.

Okuda, H., Saitoh, K., Hirai, S., Iwai, K., Takaki, Y. & Baba, M. *et al.* (2001). The von Hippel-Lindau tumor suppressor protein mediates ubiquitination of activated atypical protein kinase C. *The Journal of biological chemistry*, 276, 43611–43617.

Opperman, L.A., Passarelli, R.W., Morgan, E.P., Reintjes, M. & Ogle, R.C. (1995). Cranial sutures require tissue interactions with dura mater to resist osseous obliteration in vitro. *Journal of bone and mineral research : the official journal of the American Society for Bone and Mineral Research*, 10, 1978–1987.

Ostendorff, H.P., Peirano, R.I., Peters, M.A., Schlüter, A., Bossenz, M. & Scheffner, M. *et al.* (2002). Ubiquitination-dependent cofactor exchange on LIM homeodomain transcription factors. *Nature*, 416, 99–103.

Pavenstädt, H., Kriz, W. & Kretzler, M. (2003). Cell biology of the glomerular podocyte. *Physiological reviews*, 83, 253–307.

Perico, L., Conti, S., Benigni, A. & Remuzzi, G. (2016). Podocyte-actin dynamics in health and disease. *Nature reviews. Nephrology*, 12, 692–710.

Pettersen, E.F., Goddard, T.D., Huang, C.C., Couch, G.S., Greenblatt, D.M. & Meng, E.C. *et al.* (2004). UCSF Chimera--a visualization system for exploratory research and analysis. *Journal of computational chemistry*, 25, 1605–1612.

Pioli, P.A. & Rigby, W.F. (2001). The von Hippel-Lindau protein interacts with heteronuclear ribonucleoprotein a2 and regulates its expression. *The Journal of biological chemistry*, 276, 40346–40352.

Pressman, C.L., Chen, H. & Johnson, R.L. (2000). LMX1B, a LIM homeodomain class transcription factor, is necessary for normal development of multiple tissues in the anterior segment of the murine eye. *Genesis (New York, N.Y. : 2000)*, 26, 15–25.

Pries, A.R., Secomb, T.W. & Gaehtgens, P. (2000). The endothelial surface layer. *Pflugers Archiv : European journal of physiology*, 440, 653–666.

Rascle, A., Neumann, T., Raschta, A.-S., Neumann, A., Heining, E. & Kastner, J. *et al.* (2009). The LIM-homeodomain transcription factor LMX1B regulates expression of NF-kappa B target genes. *Experimental cell research*, 315, 76–96.

Reiser, J., Polu, K.R., Möller, C.C., Kenlan, P., Altintas, M.M. & Wei, C. *et al.* (2005). TRPC6 is a glomerular slit diaphragm-associated channel required for normal renal function. *Nature genetics*, 37, 739–744.

Reitsma, S., Slaaf, D.W., Vink, H., van Zandvoort, M.A.M.J. & oude Egbrink, M.G.A. (2007). The endothelial glycocalyx: composition, functions, and visualization. *Pflugers Archiv : European journal of physiology*, 454, 345–359.

RENWICK, J.H. & LAWLER, S.D. (1955). Genetical linkage between the ABO and nail-patella loci. *Annals of human genetics*, 19, 312–331.

Rinschen, M.M., Bharill, P., Wu, X., Kohli, P., Reinert, M.J. & Kretz, O. *et al.* (2016a). The ubiquitin ligase Ubr4 controls stability of podocin/MEC-2 supercomplexes. *Human molecular genetics*, 25, 1328–1344.

Rinschen, M.M., Schroeter, C.B., Koehler, S., Ising, C., Schermer, B. & Kann, M. *et al.* (2016b). Quantitative deep mapping of the cultured podocyte proteome uncovers shifts in proteostatic mechanisms during differentiation. *American journal of physiology. Cell physiology*, 311, C404-17.

Rodewald, R. & Karnovsky, M.J. (1974). Porous substructure of the glomerular slit diaphragm in the rat and mouse. *The Journal of cell biology*, 60, 423–433.

Rohr, C., Prestel, J., Heidet, L., Hosser, H., Kriz, W. & Johnson, R.L. *et al.* (2002). The LIM-homeodomain transcription factor Lmx1b plays a crucial role in podocytes. *The Journal of clinical investigation*, 109, 1073–1082.

Ronzaud, C. & Staub, O. (2014). Ubiquitylation and control of renal Na+ balance and blood pressure. *Physiology (Bethesda, Md.)*, 29, 16–26.

Roselli, S., Heidet, L., Sich, M., Henger, A., Kretzler, M. & Gubler, M.-C. *et al.* (2004). Early glomerular filtration defect and severe renal disease in podocin-deficient mice. *Molecular and cellular biology*, 24, 550–560.

Sachs, N., Kreft, M., van den Bergh Weerman, M.A., Beynon, A.J., Peters, T.A. & Weening, J.J. *et al.* (2006). Kidney failure in mice lacking the tetraspanin CD151. *The Journal of cell biology*, 175, 33–39.

Sachs, N. & Sonnenberg, A. (2013). Cell-matrix adhesion of podocytes in physiology and disease. *Nature reviews. Nephrology*, 9, 200–210.

Sali, A. & Blundell, T.L. (1993). Comparative protein modelling by satisfaction of spatial restraints. *Journal of molecular biology*, 234, 779–815.

Satchell, S. (2013). The role of the glomerular endothelium in albumin handling. *Nature reviews. Nephrology*, 9, 717–725.

Satchell, S.C. & Braet, F. (2009). Glomerular endothelial cell fenestrations: an integral component of the glomerular filtration barrier. *American journal of physiology. Renal physiology*, 296, F947-56.

Sato, U., Kitanaka, S., Sekine, T., Takahashi, S., Ashida, A. & Igarashi, T. (2005). Functional characterization of LMX1B mutations associated with nail-patella syndrome. *Pediatric research*, 57, 783–788.

Schell, C. & Huber, T.B. (2017). The Evolving Complexity of the Podocyte Cytoskeleton. *Journal of the American Society of Nephrology : JASN*, 28, 3166–3174.

Schnabel, E., Anderson, J.M. & Farquhar, M.G. (1990). The tight junction protein ZO-1 is concentrated along slit diaphragms of the glomerular epithelium. *The Journal of cell biology*, 111, 1255–1263.

Schönig, K., Schwenk, F., Rajewsky, K. & Bujard, H. (2002). Stringent doxycycline dependent control of CRE recombinase in vivo. *Nucleic acids research*, 30, e134.

Schroeter, C.B., Koehler, S., Kann, M., Schermer, B., Benzing, T. & Brinkkoetter, P.T. *et al.* (2018). Protein half-life determines expression of proteostatic networks in podocyte differentiation. *FASEB journal : official publication of the Federation of American Societies for Experimental Biology*, 32, 4696–4713.

Schwanhäusser, B., Busse, D., Li, N., Dittmar, G., Schuchhardt, J. & Wolf, J. *et al.* (2011). Global quantification of mammalian gene expression control. *Nature*, 473, 337–342.

Schwarz, K., Simons, M., Reiser, J., Saleem, M.A., Faul, C. & Kriz, W. *et al.* (2001). Podocin, a raft-associated component of the glomerular slit diaphragm, interacts with CD2AP and nephrin. *The Journal of clinical investigation*, 108, 1621–1629.

Scott, M.P. & Weiner, A.J. (1984). Structural relationships among genes that control development: sequence homology between the Antennapedia, Ultrabithorax, and fushi tarazu loci of Drosophila. *Proceedings of the National Academy of Sciences of the United States of America*, 81, 4115–4119.

Sellin, L., Huber, T.B., Gerke, P., Quack, I., Pavenstädt, H. & Walz, G. (2003). NEPH1 defines a novel family of podocin interacting proteins. *FASEB journal : official publication of the Federation of American Societies for Experimental Biology*, 17, 115–117.

Seri, M., Melchionda, S., Dreyer, S., Marini, M., Carella, M. & Cusano, R. *et al.* (1999). Identification of LMX1B gene point mutations in italian patients affected with Nail-Patella syndrome. *International journal of molecular medicine*, 4, 285–290.

Setzer, M. (2020). *Regulation of the actin cytoskeleton in podocytes by the transcription factor LMX1B.* Universitätsbibliothek Regensburg, Regensburg.

Shankland, S.J. (2006). The podocyte's response to injury: role in proteinuria and glomerulosclerosis. *Kidney international*, 69, 2131–2147.

Shankland, S.J., Pippin, J.W. & Duffield, J.S. (2014). Progenitor cells and podocyte regeneration. *Seminars in nephrology*, 34, 418–428.

Shen, M.-Y. & Sali, A. (2006). Statistical potential for assessment and prediction of protein structures. *Protein science : a publication of the Protein Society*, 15, 2507–2524.

Shigehara, T., Zaragoza, C., Kitiyakara, C., Takahashi, H., Lu, H. & Moeller, M. *et al.* (2003). Inducible podocyte-specific gene expression in transgenic mice. *Journal of the American Society of Nephrology : JASN*, 14, 1998–2003.

Shih, N.Y., Li, J., Karpitskii, V., Nguyen, A., Dustin, M.L. & Kanagawa, O. *et al.* (1999). Congenital nephrotic syndrome in mice lacking CD2-associated protein. *Science (New York, N.Y.)*, 286, 312–315.

Shirato, I. (2002). Podocyte process effacement in vivo. *Microscopy research and technique*, 57, 241–246.

Shirato, I., Hosser, H., Kimura, K., Sakai, T., Tomino, Y. & Kriz, W. (1996). The development of focal segmental glomerulosclerosis in masugi nephritis is based on progressive podocyte damage. *Virchows Archiv : an international journal of pathology*, 429, 255–273.

Singh Gautam, A.K., Balakrishnan, S. & Venkatraman, P. (2012). Direct ubiquitin independent recognition and degradation of a folded protein by the eukaryotic proteasomes-origin of intrinsic degradation signals. *PloS one*, 7, e34864.

Smoyer, W.E., Mundel, P., Gupta, A. & Welsh, M.J. (1997). Podocyte alpha-actinin induction precedes foot process effacement in experimental nephrotic syndrome. *The American journal of physiology*, 273, F150-7.

St John, P.L. & Abrahamson, D.R. (2001). Glomerular endothelial cells and podocytes jointly synthesize laminin-1 and -11 chains. *Kidney international*, 60, 1037–1046.

Sugimoto, H., Hamano, Y., Charytan, D., Cosgrove, D., Kieran, M. & Sudhakar, A. *et al.* (2003). Neutralization of circulating vascular endothelial growth factor (VEGF) by anti-VEGF antibodies and soluble VEGF receptor 1 (sFlt-1) induces proteinuria. *The Journal of biological chemistry*, 278, 12605–12608.

Suleiman, H., Heudobler, D., Raschta, A.-S., Zhao, Y., Zhao, Q. & Hertting, I. *et al.* (2007). The podocyte-specific inactivation of Lmx1b, Ldb1 and E2a yields new insight into a transcriptional network in podocytes. *Developmental biology*, 304, 701–712.

Suleiman, H., Zhang, L., Roth, R., Heuser, J.E., Miner, J.H. & Shaw, A.S. *et al.* (2013). Nanoscale protein architecture of the kidney glomerular basement membrane. *eLife*, 2, e01149.

Sweeney, E., Fryer, A., Mountford, R., Green, A. & McIntosh, I. (2003). Nail patella syndrome: a review of the phenotype aided by developmental biology. *Journal of medical genetics*, 40, 153–162.

Timpl, R. (1989). Structure and biological activity of basement membrane proteins. *European journal of biochemistry*, 180, 487–502.

Tryggvason, K., Patrakka, J. & Wartiovaara, J. (2006). Hereditary proteinuria syndromes and mechanisms of proteinuria. *The New England journal of medicine*, 354, 1387–1401.

Tryggvason, K. & Wartiovaara, J. (2001). Molecular basis of glomerular permselectivity. *Current opinion in nephrology and hypertension*, 10, 543–549.

Urlinger, S., Baron, U., Thellmann, M., Hasan, M.T., Bujard, H. & Hillen, W. (2000). Exploring the sequence space for tetracycline-dependent transcriptional activators: novel mutations yield expanded range and sensitivity. *Proceedings of the National Academy of Sciences of the United States of America*, 97, 7963–7968.

Voges, D., Zwickl, P. & Baumeister, W. (1999). The 26S proteasome: a molecular machine designed for controlled proteolysis. *Annual review of biochemistry*, 68, 1015–1068.

Vollrath, D., Jaramillo-Babb, V.L., Clough, M.V., McIntosh, I., Scott, K.M. & Lichter, P.R. *et al.* (1998). Loss-of-function mutations in the LIM-homeodomain gene, LMX1B, in nail-patella syndrome. *Human molecular genetics*, 7, 1091–1098.

Wang, X. & Terpstra, E.J.M. (2013). Ubiquitin receptors and protein quality control. *Journal of molecular and cellular cardiology*, 55, 73–84.

Wartiovaara, J., Ofverstedt, L.-G., Khoshnoodi, J., Zhang, J., Mäkelä, E. & Sandin, S. *et al.* (2004). Nephrin strands contribute to a porous slit diaphragm scaffold as revealed by electron tomography. *The Journal of clinical investigation*, 114, 1475–1483.

Weinbaum, S., Tarbell, J.M. & Damiano, E.R. (2007). The structure and function of the endothelial glycocalyx layer. *Annual review of biomedical engineering*, 9, 121–167.

Wiggins, R.C. (2007). The spectrum of podocytopathies: a unifying view of glomerular diseases. *Kidney international*, 71, 1205–1214.

Wilkie, A.O. (1997). Craniosynostosis: genes and mechanisms. *Human molecular genetics*, 6, 1647–1656.

Winn, M.P., Conlon, P.J., Lynn, K.L., Farrington, M.K., Creazzo, T. & Hawkins, A.F. *et al.* (2005). A mutation in the TRPC6 cation channel causes familial focal segmental glomerulosclerosis. *Science (New York, N.Y.)*, 308, 1801–1804.

Witzgall, R. (2017). Nail-patella syndrome. *Pflugers Archiv : European journal of physiology*, 469, 927–936.

Wu, Q., Moeller, H.B., Stevens, D.A., Sanchez-Hodge, R., Childers, G. & Kortenoeven, M.L.A. *et al.* (2018). CHIP Regulates Aquaporin-2 Quality Control and Body Water Homeostasis. *Journal of the American Society of Nephrology : JASN*, 29, 936–948.

Yu, H., Singh Gautam, A.K., Wilmington, S.R., Wylie, D., Martinez-Fonts, K. & Kago, G. *et al.* (2016). Conserved Sequence Preferences Contribute to Substrate Recognition by the Proteasome. *The Journal of biological chemistry*, 291, 14526–14539.

Yun, C.W., Lee, S.H., Fujikake, N., Shin, M. & Shimizu, S. (2018). The Roles of Autophagy in Cancer // Association Between Autophagy and Neurodegenerative Diseases. *International journal of molecular sciences*, 19 // 12, 255.

Zaidel-Bar, R., Cohen, M., Addadi, L. & Geiger, B. (2004). Hierarchical assembly of cell-matrix adhesion complexes. *Biochemical Society transactions*, 32, 416–420.

Zenker, M., Aigner, T., Wendler, O., Tralau, T., Müntefering, H. & Fenski, R. *et al.* (2004). Human laminin beta2 deficiency causes congenital nephrosis with mesangial sclerosis and distinct eye abnormalities. *Human molecular genetics*, 13, 2625–2632.

Zhang, M., Pickart, C.M. & Coffino, P. (2003). Determinants of proteasome recognition of ornithine decarboxylase, a ubiquitin-independent substrate. *The EMBO journal*, 22, 1488–1496.

7. List of abbreviations

In general, abbreviations of proteins and genes of human origin were written in capital letters, in contrast to murine genes and proteins, which start with a capital letter. Furthermore, genes were written in italics.

A

A	Absorbance
aa	Amino acid
AA	Afferent ateriole
Abra	Actin-binding Rho-activating
ACTN	α-actinin
Amp	Ampicillin
ADP	Adenosine-5’-diphosphate
APS	Ammonium persulfate
ATP	Adenosine-5’-triphosphate

B

β	Mass concentration
Baf-A_1	Bafilomycin A_1
bp	Base pairs
bidest	Double distilled
BS	Bowman space
BSA	Bovine serum albumin

C

c	Concentration
°C	Degrees Celsius
C95F	Substitution of a cysteine into a phenylalanine on position 95
$CaCl_2$	Calcium chloride
CD2AP	CD2 associated protein
cDNA	Complementary DNA
CHX	Cycloheximide
CO_2	Carbon dioxide
COL4	Collagen type IV
Cre	Cyclization recombination
COOH-terminus	Carboxy-terminus
CT-value	Threshold of the real-time PCR

D

d	day
dd	Double distilled
DMEM	Dulbecco´s modified eagle medium
DMSO	Dimethylsulfoxide
DNA	Deoxyribonucleic acid
dNTP	Deoxynucleotide triphosphate
Dox	Doxycycline
DpnI	Enzyme from *Diplococcus pneumoniae* G41

E

ε	Extinction coefficient
E18.5	Mouse embryonic day 18.5
E	Fenestrated endothelium
EA	Efferent ateriole
E. coli	*Escherichia coli*
EDTA	Ethylenediaminetetraaceticacid
EGM	Extraglomerular mesangium
et al.	latin: et alia, and others
EtOH	Ethanol

F

FCS	Fetal calf serum
FLAT	FAR linked AT-rich
Floxed / loxed	Flanked by *loxP*
FP	Foot processes of the podocytes
FSGS	Focal segmental glomerulosclerosis

G

g	Gravitational acceleration
G418	Geneticin 418
GA	Glutaraldehyde
GAPDH	Glyceraldehyde 3-phosphate dehydrogenase
GBM	Glomerular basement membrane
GFB	Glomerular filtration barrier
GFP	Green fluorescent protein

H

h	Human (*homo sapiens*)
h	hour
H_2O	Water
H54L	Substitution of a histidine into a leucine on position 54
HCl	Hydrogen chloride
hCMV	Human cytomegalovirus
HD	Homeodomain
HeLa	Human cervical cancer cell line
HEPES	4-(2-hydroxyethyl)-1-piperazineethansulfonic acid
hPCL	Human podocyte cell line
HRP	Horseradish peroxidase
HtTA-1	HeLa cells stably transfected with a tetracycline-controlled transactivator (tTA) consisting of the tet repressor fused with the activating domain of virion 16 of herpes virus simplex virus

I

IF (Cryo)	Immunofluorescence
IL	Interleukin

K

KCl	Potassium chloride
kDa	kilodalton
Kg	Kilogram
KH_2PO_4	Potassium dihydrogen phosphate
KO	knock-out

L

l	Length
LB	Lysogeny broth
LC-1	Luciferase-Cre-1
LDB	LIM-domain binding protein
LMX1A	LIM homeobox transcription factor 1 alpa
LMX1B	LIM homeobox transcription factor 1 beta
loxP	Locus of X-over P1

M

m	Murine (*mus musculus*)
M	Molar
mA	milliamperes
MC	Mesangial cells
MD	Macula densa
mG	Membrane-targeted EGFP
MG-132	Proteasome inhibitor
$MgCl_2$	Magnesium chloride
min	minutes
mL	milliliter
mM	millimolar
mT	Membrane-targeted tdTomato
µCT	Micro computertomography
µg	Microgram
µL	Microliter
µm	Micrometer

N

N	Number
ng	Nanogram
n.s.	Not significant
Na_2HPO_4	Disodium hydrogen phosphate
$Na_3C_3H_5(COO)_3$	Trisodium citrate
NaAc	Sodium acetate
NaCl	Sodium chloride
$NaHCO_3$	Sodium hydrogen carbonate
NaOH	Sodium hydroxide
NPHS2	Nephrosis 2, idiopathic, steroid-resistant (Podocin)
NPS	Nail-patella syndrome
NH_2-terminus	Amino terminus

O

o/n	Over night
OD	Optical density
Oligo	Oligonucleotide
OMIM	Online Mendelian Inheritance in Man
ORF	Open reading frame

P

p-	Plasmid-, Phospho-
p.a.	pro analysi
pA	Polyadenylation sequence
PAGE	Polyacrylamide gel electrophoresis
PBS	Phosphate buffered saline
PCR	Polymerase chain reaction
PFA	Paraformaldehyde
PI	Propidium iodide
PS-341	Proteasome inhibitor bortezomib
PVDF	Polyvinylidene fluoride

Q

qPCR	Quantitative polymerase chain reaction

R

RNA	Ribonucleic acid
m-	messenger
mi-	micro
si-	small interfering
RNAse	Ribonuclease
rpm	Rounds per minute
RT	Reverse transcriptase
RT	Room temperature
rtTA	Reverse tetracycline-controlled transcriptional transactivator

S

s	Second
S9	Ribosomal protein S9
SD	Slit diaphragm
SDS	Sodium dodecyl sulfate
SEM	Scanning electron microscopy
SV40	Simian virus 40
SYNPO	Synaptopodin

T

t	time
TAE	Tris, acetic acid, EDTA
Taq	*Thermus aquaticus*
TBS	Tris buffered saline
TBS-T	Tris buffered saline, supplemented with 0.1 % Tween 20
tdtomato	Tandem dimer tomato protein
TE	Tris-EDTA
TEM	Transmission electron microscopy
TEMED	Tetramethylethylenediamine
TetO	Tet operon
TG	Transgene
TRPC6	Transient receptor potential cation channel subfamily C member 3
tTA	Tetracycline controlled transactivator

U

U-	Ubiquitin molecule
U	Unit
UTR	Untranslated region

V

V	Volume
V	Volt
V242D	Substitution of a valine into an aspartate on position 242
VEGF-A	Vascular endothelial growth factor A

W

WB	Western blot
WT	Wild-type
WT1	Wilms Tumor 1

Z

ZO-1	Zonula occludens-1

8. Acknowledgements

The present thesis has been conducted between October 2016 and October 2020 at the Department of Molecular and Cellular Anatomy at the University of Regensburg. This doctoral thesis would not have come to a successful completion without the support, suggestions, and patience of many people, to whom I would like to express my sincere gratitude in the following.

Foremost, I would like to thank Prof. Dr. Ralph Witzgall for being my thesis supervisor, for giving me the opportunity to work on the exciting LMX1B project, and for his input, patience, and confidence. In the last four years, I appreciated a lot the freedom to plan and perform my experiments, however, received support and feedback in any situation when I needed help.

In addition, I am very grateful to my mentoring team: Prof. Dr. Achim Göpferich and Prof. Dr. Eugen Kerkhoff provided precious scientific advice during the mentor meetings and the evaluation of my research.

I would like to thank Dr. Melanie Zaparty and Dr. Melanie Grosch for their professional advice and support. I appreciated to discuss with them about science and they provided lots of good suggestions and ideas. Special thanks to both of them for the final proofreading, constructive criticism and scientific discussion concerning my thesis.

I want to express my gratitude to Larissa Osten who gave me technical and maternal support during my thesis. In addition, I am thankful for all the help of Marion Kubitza in technical questions and everyday laboratory work. Apart from that, I want to thank Marina Wuttke, Suzan Kücükoktay and Adelina Altfreder, who assisted me a lot at the laboratory work, especially in genotyping of the transgene mice. Many thanks also go to Kerstin Hermann, Karin Schadendorf, and Helga Othmen for help and support concerning electron microscopy.

Special thanks go to Dr. Birgit Striegl from the Department of Mechanical Engineering at the Ostbayerische Technische Hochschule of Regensburg, for her great service and assistance concerning the µCT measurements.

Further I want to thank Dr. Gregor Madej from the research group Ziegler for his great support concerning the 3D homology modeling.

I want to thank my current and former fellow PhD colleagues: Dr. Susanne Baumgarten, Dr. Markus Setzer, Sandra Meisinger, Katrin Brunner, Jasmin Karreis, and Dr. Korbinian Bürger for creating a great atmosphere and moral support. In addition, I want to thank Florian Heiß and Philipp Becker for the entertaining lunch sessions and coffee breaks. Special thanks go to Dr. Markus Setzer for introducing me in the LMX1B project and answering all of my questions.

Great thanks to the Bachelor students, Gabriela Zuleger and Fabian Kugler, who contributed to this thesis by excellent experimental assistance.

I would like to acknowledge Anita Hecht and Anthonie Maurer for their constant help with image editing and photoshopping. Many thanks go to Uwe de Vries for his support with electronics, software, microscopy equipment and instruments.

A big thank you goes to Petra and Ludwig Utz. They took on the role of my university parents, always encouraging me and giving lots of mental support. Every time when I met them on the floor, I had to smile from ear to ear – always happy to see them. In addition, many thanks to Lena Seitz for her help and support in the reprocessing unit.

Further thanks go to all the current and former members of Prof. Witzgall´s group for the pleasant atmosphere I experienced the last four years: Prof. Dr. Silke Härteis, Prof. Dr. Reinhard Rachel, Dr. Kerstin Schmidt, Eva Chira, Justin Skotnitzki, Edeltraud Lautenschlager, Olga Maier, Christine Meese, Lucia Denk, Anita Zügner, Yulia Zaytseva, and Antje Zenker.

My special thanks also go to my dear friends for listening, offering me advice, and always supporting me, especially Julia Lenz, Lena Hacker, Marion Insprucker, Bilge Gümüs, Ella Beck, Jennifer Minge, Margarethe Bohmeier, and Amelie Bollwein. In addition, I would like to acknowledge Helma and Haschl for the unremitting support and care in so many ways.

In the end, I would like to say thank you to my wonderful family. They have been my backbone during my doctoral journey and gave me incredible mental support and motivation. Without them, my studies in biology would have been impossible and I would not have managed the long journey, which I will finish with this thesis. Thank you, Verena, Mama & Papa for your great support and patience in the last ten years.

Last but, not least, I would like to thank my partner in crime and best friend, Marco. For his great patience, support, encouragement, and advice during my entire studies. Especially, in the last four years of my doctoral thesis, he has taken care of whatever needed to be organized, just that I could focus on my dissertation. I am so grateful to have you in my life.

Eidesstattliche Erklärung

Ich erkläre hiermit an Eides statt, dass ich die vorliegende Arbeit ohne unzulässige Hilfe Dritter und ohne Benutzung anderer als der angegebenen Hilfsmittel angefertigt habe; die aus anderen Quellen direkt oder indirekt übernommenen Daten und Konzepte sind unter Angabe des Literaturzitats gekennzeichnet.

Bei Auswahl und Auswertung folgenden Materials haben mir die in der Arbeit genannten Personen in der jeweils beschriebenen Weise unentgeltlich geholfen.

Weitere Personen waren an der inhaltlich-materiellen Herstellung der vorliegenden Arbeit nicht beteiligt. Insbesondere habe ich hierfür nicht die unentgeltliche Hilfe eines Promotionsberaters oder anderer Personen in Anspruch genommen. Niemand hat von mir weder unmittelbar noch mittelbar geldwerte Leistungen für Arbeiten erhalten, die im Zusammenhang mit dem Inhalt der vorgelegten Dissertation stehen.

Die Arbeit wurde bisher weder im In- noch im Ausland in gleicher oder ähnlicher Form einer anderen Prüfungsbehörde vorgelegt.

_____

Lisa Lucke